Three-port DC-DC Converters to Interface Renewable Energy Sources with Bi-directional Load and Energy Storage Ports

A DISSERTATION
SUBMITTED TO THE FACULTY OF THE GRADUATE SCHOOL
OF THE UNIVERSITY OF MINNESOTA
BY

Hariharan Krishnaswami

IN PARTIAL FULFILLMENT OF THE REQUIREMENTS
FOR THE DEGREE OF
DOCTOR OF PHILOSOPHY

August, 2009

Acknowledgements

It is a pleasure to thank the many people who have made this thesis possible.

I owe my deepest gratitude to my supervisor, Professor Mohan, who has guided, mentored and supported me throughout my graduate studies. This thesis would not have been possible without his valuable inputs, good teaching and sound advice. He has always been and will be an inspiration to me.

I would like to thank Professor Robbins for providing me an opportunity to teach and gain valuable teaching experience. I would like to thank Professor Wollenberg for his excellent teaching and continuous encouragement. I am grateful to Professor Imbertson for his guidance during my job as a teaching assistant. I would also like to thank Professor Rajamani for having agreed to be part of the oral exam committee. I owe my gratitude to all the Professors who have taught me in graduate school.

I gratefully acknowledge the support given by Institute of Renewable Energy and Environment, University of Minnesota for this dissertation.

I would like to thank my parents who have given me unfailing support and love throughout and to whom I have dedicated this thesis. I would also like to thank my family members and relatives who have inspired and continuously motivated me.

My stay in graduate school has been made memorable by my friends, Ranjan, Apurva, Kaushik and Shivaraj with whom I had countless technical and personal discussions. I would also like to thank all my lab colleagues for creating a learning and fun environment.

Dedication

To my parents

ABSTRACT

Power electronic converters are needed to interface multiple renewable energy sources with the load along with energy storage in stand-alone or grid-connected residential, commercial and automobile applications. Recently, multi-port converters have attracted attention for such applications since they use single-stage high frequency ac-link based power conversion as compared to several power conversion stages in conventional dc-link based systems. In this thesis, two high frequency ac-link topologies are proposed, series resonant and current-fed three-port dc-dc converters. A renewable energy source such as fuel-cell or PV array can be connected to one of the ports, batteries or other types of energy storage devices to the second port and the load to the third port.

The series resonant three-port converter has two series-resonant tanks, a three-winding transformer and three active full-bridges with phase-shift control between them. The converter has capabilities of bi-directional power flow in the battery and the load port. Use of series-resonance aids in high switching frequency operation with realizable component values when compared to existing three-port converter with only inductors. Steady-state analysis of the converter is presented to determine the power flow equations, tank currents and soft-switching operation boundary. Dynamic analysis is performed to design a closed-loop controller to regulate the load-side port voltage and source-side port current. Design procedure for the three-port converter is explained and experimental results of a laboratory prototype are presented.

For applications where the load-port is not regenerative, a diode bridge is more economical than an active bridge at the load-side port. For this configuration, to control the output voltage and to share the power between the two sources, two control variables are proposed. One of them is the phase shift between the outputs of the active bridges and the other between two legs in one of the bridges. The latter uses phase-shift modulation to reduce the value of the fundamental of the bridge output. Steady-state analysis is presented to determine the output voltage, input port power and soft-switching operation boundary as a function of the phase shifts. It is observed from the analysis that the power can be made bi-directional in either of the source ports

by varying the phase shifts. Design procedure, simulation and experimental results of a prototype converter are presented.

The current-fed bi-directional three-port converter consists of three active full bridges with phase-shift control between them. Their inputs are connected to dc voltage ports through series inductors and hence termed as current-fed. The outputs are connected to three separate transformers whose secondary are configured in delta, with high frequency capacitors in parallel to each transformer secondary. The converter can be used in applications where dc currents at the ports and high step-up voltage ratios are desired. Steady-state analysis to determine power flow equations and dynamic analysis are presented. The output voltage is independent of the load as observed from analysis. Simulation results are presented to verify the analysis.

Contents

List of Tables

List of Figures

Chapter 1

Introduction

Renewable energy sources such as Fuel-Cells, Photo-Voltaic (PV) arrays are increasingly being used in automobiles, residential and commercial buildings. For stand-alone systems energy storage devices are required for backup power and fast dynamic response. A power electronic converter interfaces the sources with the load along with energy storage. Existing converters for such applications use a common dc-link. High frequency ac-link based systems have recently been explored due to its advantages of reduced part count, reduced size and centralized control. Such a high frequency ac-link based converter is termed as a multi-port converter in literature, to whose ports are connected the energy sources, energy storage devices and the load. In this chapter an introduction to multi-port converter is given. This is followed by the context, scope, contributions and organization of this thesis.

1.1 Multi-port dc-dc converter

1.1.1 Characteristics of multi-port converter

Multi-port converter has several ports to which sources or loads can be connected as shown in Fig. 1.1. The converter regulates the power flow between the sources and the loads. All of the ports have bi-directional power flow capability. The characteristics of a multi-port converter are,

- Bi-directional power flow in all of the ports

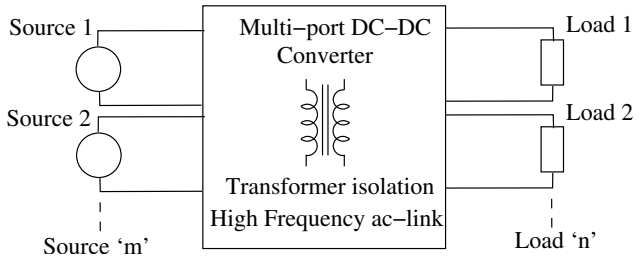

Figure 1.1: Block diagram of multi-port dc-dc converter showing 'm' sources and 'n' loads

- Control of power flow between the ports as application demands
- Port voltages can vary between few tenths of a volt to hundreds of volts
- Galvanic isolation between all ports
- All ports are interfaced through high frequency ac-link

1.1.2 Applications of multi-port dc-dc converter

Rooftop solar panels are being widely used to power residential and commercial buildings. For example, the Department of Energy (DOE) has the Solar America Cities initiative to increase the deployment of solar energy in major cities [1]. Energy storage will be used to store excess power and also as a backup unit to supply vital equipments. Due to cost reasons energy storage is applicable more in off-grid applications. A three-port converter with one of the ports connected to the solar panel or the front-end converter of the solar panel, another port connected to the battery and the third port to the load can be used for such an application. It is also possible for the utility to use energy storage in these buildings to meet peak power demands [2]. Hence, a fourth port connected to the utility through a bi-directional rectifier can be added to the converter.

Fuel-cell automobiles are considered to be an option for future clean energy automobiles [3]. The primary source will be fuel-cells with the power during acceleration and deceleration supplied from batteries. Fuel-cells have slow dynamic response and hence energy storage is essential in such an application. Batteries can be charged from fuel-cells and during regenerative braking operation. Three-port converter fits well into

this fuel-cell vehicle application. An uninterruptible power supply (UPS) can also be considered as a three-port converter [4]

The three-port converter discussed in this thesis has dc ports. If a motor or residential load needs ac, an inverter can be connected at the output of the load port. Some applications where multi-port converter can be used are listed below.

1. Fuel-cell hybrid automobiles – Port1: Fuel-cell, Port2: Batteries and/or ultracapacitors and Port3: Automobile load - Electric drive

2. Fuel-cell power conditioning systems – Port1: Fuel-cell, Port2: Batteries and Port3: AC loads with three-phase inverter

3. Off-grid residential buildings – Port1: Solar panels or Fuel-cells, Port2: Batteries and Port3: Residential loads

4. Grid-connected residential buildings – Port1: Solar panels or Fuel-cells, Port2: Batteries, Port3: Utility and Port4: Residential loads

1.1.3 High frequency ac-link based multi-port converter

Existing converter for the applications mentioned in the previous section use a common high voltage dc link as shown in Fig. 1.2. There are two stages of conversion, a dc-dc converter between the source and the dc bus and a bi-directional dc-dc converter between the battery and the dc bus. The load is connected to the dc bus through an inverter. Each of the dc-dc converters have a separate control stage along with a centralized control for determining power sharing ratio.

The dc link in Fig. 1.2 can be replaced with high frequency ac link and the number of stages can be reduced from two to one. Such a three-port converter is shown in Fig 1.3. The advantages of such an approach are [5],

- Single power conversion stage reduces component count on semiconductor switches, drive circuits and magnetics

- Reduced size due to reduced component count when compared to dc link based three-port converter

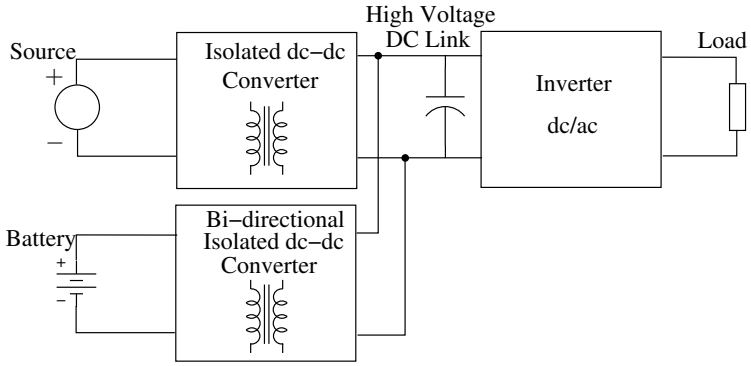

Figure 1.2: Block diagram of three-port dc-dc converter with dc link

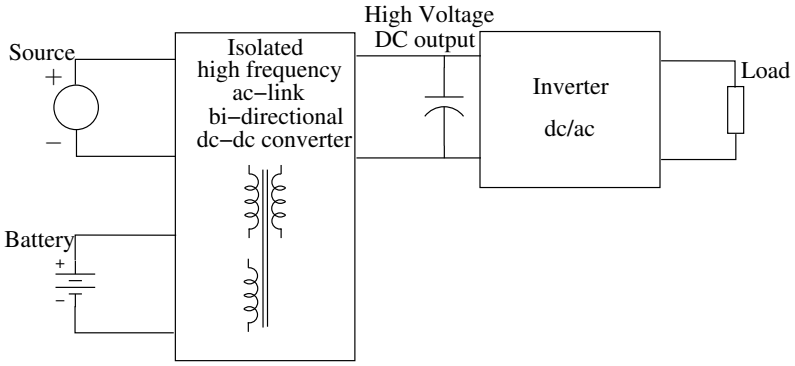

Figure 1.3: Block diagram of three-port dc-dc converter with high frequency ac-link

- High frequency three-winding transformer provides the isolation between the three ports
- Due to single-stage power conversion, the converter has a centralized control for regulating the output voltage and determining the power sharing ratio
- The converter naturally yields to bi-directional power flow in all ports

One method of building a single-stage power converter circuit interfacing multiple energy sources and the load is to emulate a multiple bus power system. The power flow is determined by the bus voltage magnitude, phase angle and the impedance of the transmission line between the buses. The active power plow between two buses with

voltages $V_1\angle 0$ and $V_2\angle -\theta$ is given by (1.1).

$$P = \frac{V_1 V_2}{X} \sin\theta \tag{1.1}$$

where P = Active power flow from bus1 to bus2

V_i = Voltage magnitude at bus 'i'

θ = Phase angle difference in radians between bus1 and bus2 voltages

X = Transmission line reactance ωL

The bus voltages are generated from dc sources using power electronic converters which can vary the magnitude, phase angle and the frequency of the bus voltages. Hence power flow can be controlled by the phase angles or voltage magnitudes or the frequency which changes the impedance or a combination of all these three methods. The impedance can be an inductor, capacitor or a resonant circuit using different connections of inductors and capacitors.

Two-port converter circuits using this principle of power flow such as the dual active bridge converter [6] and series resonant converter [7] have been existing in literature. These circuits are used in high-power dc-dc converters and high output voltage dc-dc converters. Also these converters are predominantly used for uni-directional power flow from source to load. Hence the load side active switches are replaced by a diode bridge. For telecommunication and aerospace applications high frequency ac-link based systems were explored [8,9]. They have multiple power converters powered from the same source or different sources, used mainly for paralleling operation and ac distribution.

With increased use of renewable energy sources in recent years, three-port or multi-port configurations with bi-directional ports have gained attraction. The principle of power flow explained using (1.1) can be extended for these applications. Several topologies and control methods have been proposed in literature. All of these topologies use inductors as the main power transfer and storage element. The following section explains the existing three-port converters. Another method of building a single stage power converter circuit is to use time-sharing principle i.e., at any time instant only one of the sources will be connected to the load. This method is also explained in the following section.

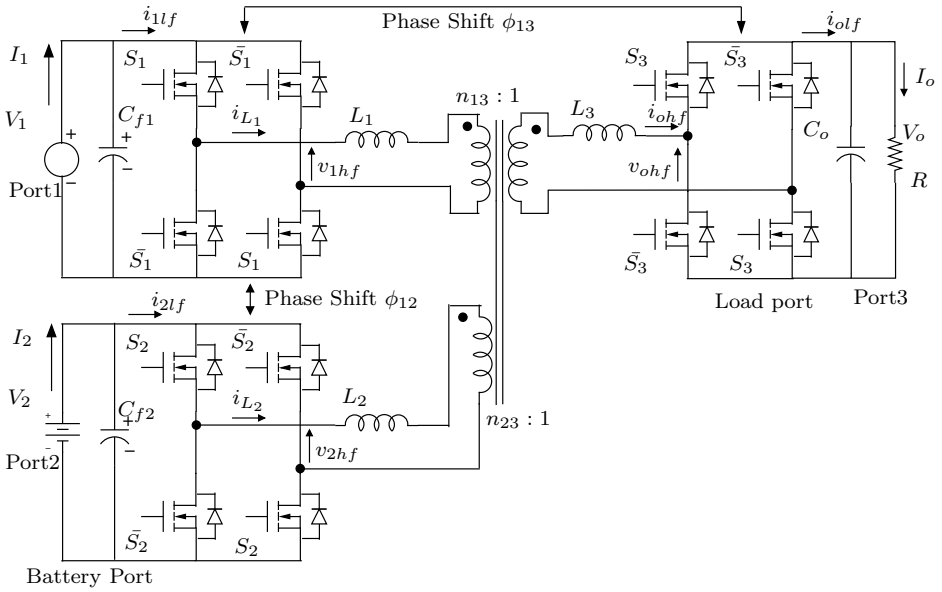

Figure 1.4: Triple active bridge three-port bi-directional converter

1.2 Existing three-port converter circuits

1.2.1 Triple active bridge three-port bi-directional converter

A three-port bi-directional converter using the principle explained in Section 1.1.3 for hybrid fuel-cell systems was proposed in [10]. The circuit diagram is shown in Fig. 1.4 where the full-bridges operate in square wave mode phase-shifted from each other. The phase-shift angle is assumed to be positive when lagging. The transformer can be represented as an extended cantilever model [11] as shown in Fig. 1.5 so that expressions for power flow can be derived. One of the power flow equations is given in (1.2). Note that the bus voltages are square waves. The converter proposed in [10] is a three-port extension of the dual active bridge converter [6]. One of the drawbacks of this converter is that the switching frequency and the inductor value cannot be determined independently for the same power level in (1.2). The inductor L_i includes the leakage inductance of the transformer. To achieve realizable inductor values greater than or equal to the leakage inductances of the transformer, the switching frequency should be reduced.

$$P_{13} = \frac{V_1 V_3}{\omega_s L_1'} \phi_{13} \left(1 - \frac{|\phi_{13}|}{\pi}\right) \tag{1.2}$$

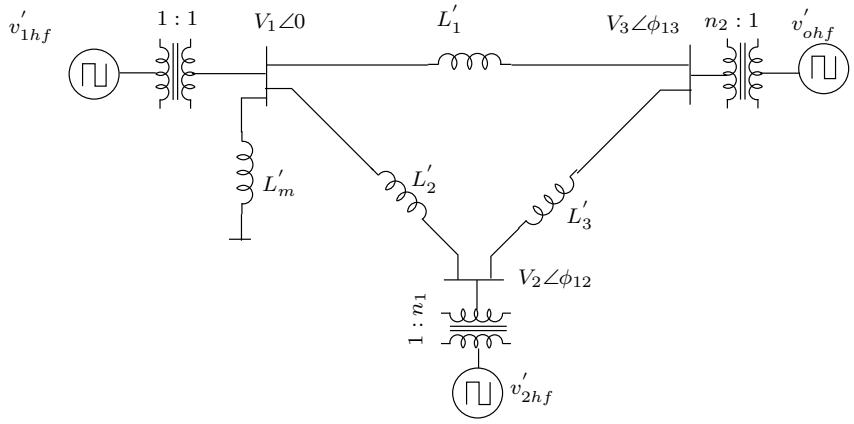

Figure 1.5: Three-winding transformer model equivalent representation for calculation of power flow

The converter in Fig. 1.4 can perform soft-switching or Zero Voltage Switching (ZVS) if the circuit parameters are adequately designed. To extend the ZVS range for load and input voltage variations, freewheeling intervals can be introduced in one or all of the bridges as explained in [12]. Apart from phase-shifting the voltage outputs of the bridges, duty cycle modulation is introduced in such a way that the average voltage is zero. This is equivalent to varying the magnitude of the fundamental of v_{ihf}.

The sources which are connected to the ports like batteries, supercapacitors have wide voltage ranges. To mitigate the effect of such variations on the range of phase-shifts and soft-switching operation, a boost half-bridge stage at the input of such ports is proposed in [13]. For high power applications, a three-phase version of the converter is proposed in [14]. This increases the current handling capacity of the converter. To control the output voltage and port power, a control methodology using two control loops is also given in [12, 13].

1.2.2 Triple half-bridge bi-directional converter

A three-port converter using two boost half-bridges at the input ports is proposed in [15] to interface batteries and supercapacitors with fuel cell output. The voltages are very low at the battery and capacitor end and hence a boost half-bridge is used to boost the voltage and also to create a square wave at the input of the transformer. Such a circuit is shown in Fig. 1.6. The control of power flow uses the same principle explained in

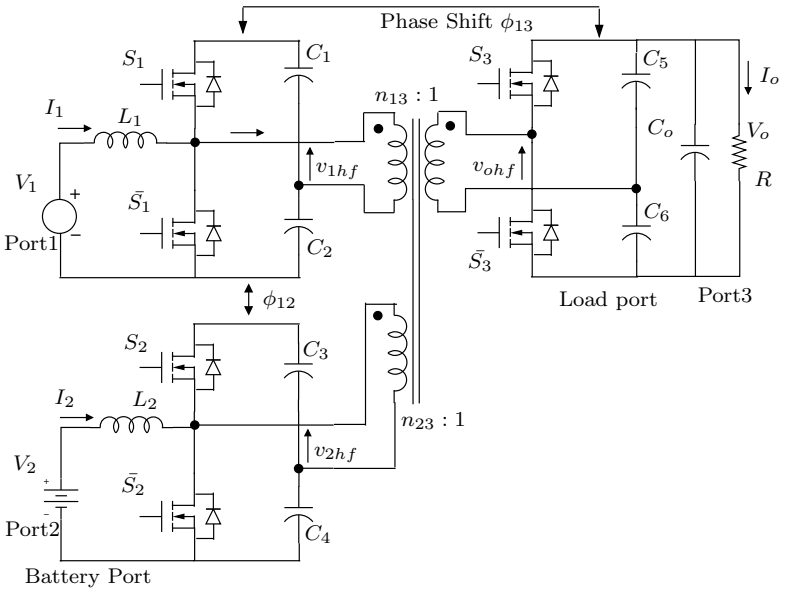

Figure 1.6: Triple half-bridge bi-directional converter

Section 1.2.1. This topology is especially advantageous in interfacing very low input voltage ports. Soft-switching operation is possible by appropriately selecting the circuit parameters.

1.2.3 Multiple-input buck-boost converter

A multiple-input buck-boost converter is proposed in [16] which uses the voltage sources on a time-shared basis. At any instant of time only one source is connected to the buck-boost inductor. The general circuit is shown in Fig. 1.7. A similar circuit can be implemented using flyback converter [17]. Bi-directional power flow can be enabled in all ports if needed, but there will not be any isolation between the ports. Matching wide voltage ranges will be difficult in this circuit without a transformer.

There are several other circuits for three-port converter proposed in the literature such as the tri-modal half-bridge converter having an active clamp forward converter [18], series-parallel resonant UPS with uni-directional load port with separate modes of operation for line operation and backup operation [19], a three-phase three-port UPS using a single high frequency transformer [4] and other topologies [20, 21, 22, 23, 24].

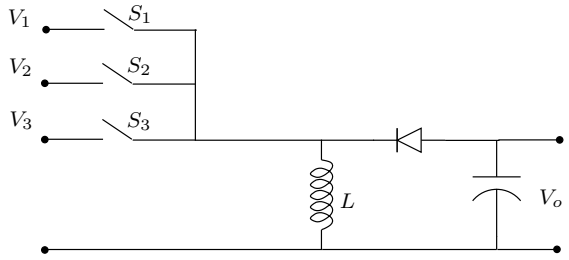

Figure 1.7: Multiple-input buck-boost converter

1.3 Scope of this thesis

The triple active bridge three-port bi-directional converter can meet all the requirements of a multi-port converter explained in Section 1.1.3. But, one of the drawbacks of this converter is that at medium to high power, the values of the inductances become difficult to control. To get values of inductors more than the leakage inductance of the transformer the switching frequency needs to be reduced. To overcome this problem and to enable high switching frequency operation, a series resonant three-port converter is proposed in this thesis. Besides, the converter has other features such as reduced peak currents and near sinusoidal currents and voltages which simplifies the analysis. This converter is analyzed in detail in this thesis under both steady-state and dynamic operation. In applications where uni-directional load ports are used, replacing active bridge with diode bridge proves more advantageous in terms of switching losses and reduction in drive circuitry. A series resonant three-port converter for such an application is also explored in this thesis.

In all the voltage-fed converters described in this thesis and literature, large input filter capacitors are required to filter the switching current at the ports. Current-fed circuits are more advantageous in battery charging applications where charging currents are dc. A current-fed three-port converter is proposed in this thesis which can maintain dc currents at the ports. Detailed analysis in steady-state and dynamic operation is presented.

The objective of this thesis is to suggest different circuit topologies for three-port converter which have unique advantages over existing topologies. This thesis also analyzes all the proposed topologies in detail and establishes design procedures. Simulation

and experimental results are presented to augment the analysis.

1.4 Contributions of this thesis

The contributions of this thesis are:

1. A novel series resonant three-port dc-dc converter with two series resonant tanks, three-winding transformer and three active bridges phase-shifted from each other for power flow control.

2. Detailed steady-state analysis of the converter to determine output voltage, port power, tank currents, tank voltages and soft-switching operation boundary.

3. Dynamic analysis of the converter using generalized averaging theory and controller design to control the output voltage and port powers.

4. Phase-shift control techniques for the series resonant three-port converter with unidirectional load port configuration and detailed steady-state analysis to determine the converter variables.

5. Design procedure, simulation and experimental results for both configurations of series resonant three-port converter

6. A novel current-fed three-port dc-dc converter for achieving dc currents at the ports

7. Steady-state and dynamic analysis of the current-fed three-port converter

1.5 Organization of this thesis

Chapter 1 introduces the three-port converter and its applications. The existing literature on three-port converter is explained. In Chapter 2 the series resonant three-port converter is introduced and steady-state analysis is presented. The three-winding transformer model and its effect on steady-state performance is also examined. To understand the dynamic response of the converter, a dynamic model is derived and closed-loop control design is explained in Chapter 3. The design of the series resonant

three-port converter is explained in Chapter 4 and simulation and experimental results are presented to verify the analysis. For uni-directional output configuration, phase-shift control techniques are proposed in Chapter 5 and detailed analysis is presented along with simulation and experimental results. For applications where dc current is desired at the ports, a current-fed topology is proposed and analyzed in Chapter 6. The design of such a converter is also presented along with simulation and experimental results. The last chapter concludes this thesis.

1.6 Conclusion

In this chapter the context of the thesis is established. The multi-port converter is introduced and its applications explained. Existing topologies of the three-port converter are described. The scope and contributions of this thesis are given.

Chapter 2

Three-port Series Resonant Converter - Steady-state Analysis

Series resonant dc-dc converters are used in several applications such as high-voltage and high-density power supplies. These converters have zero switching losses due to soft-switching and hence reduced size and higher power density when compared to conventional dc-dc converters. They are mostly uni-directional with only two ports, source and load. With proliferation of distributed renewable energy sources, there has been recently lot of interest in integrating the source, energy storage and the load into a single stage power conversion. Resonant converters are the choice for such applications due to the aforementioned advantages. In this chapter, a three-port series resonant dc-dc converter using a single-stage power conversion is proposed and analyzed.

2.1 Principle of operation

2.1.1 Two-port series resonant converter

The two-port series resonant converter which is well known in literature is shown in Fig 2.1. The transformer turns ratio is taken to be unity. The phase shift θ is between the square-wave outputs of the active bridges at either end of the resonant tank. The switching frequency F_s is constant. The resonant tank voltages and currents can be assumed to be sinusoidal due to the filtering action of the resonant circuit. Hence only

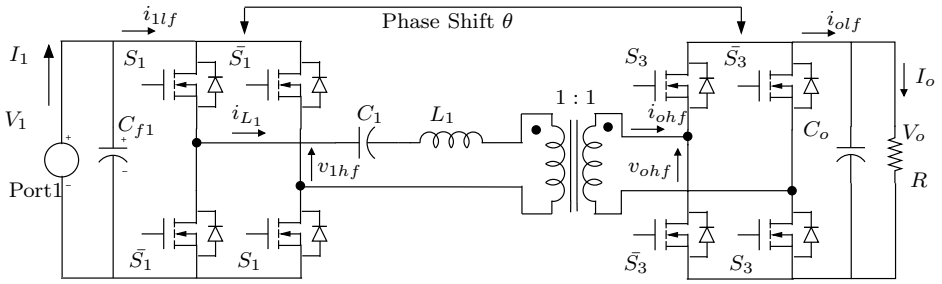

Figure 2.1: Two-port series resonant converter with two active bridges

the fundamental of the applied square wave can be used in the calculation of tank current. The output voltage V_o of the converter is given in (2.1).

$$V_o = \frac{V_1}{Q_1(F_1 - \frac{1}{F_1})} \sin\theta \tag{2.1}$$

$$\text{where } Q_1 = \frac{Z_1}{\frac{8}{\pi^2}R} \; ; \; Z_1 = \sqrt{\frac{L_1}{C_1}} \; ; \; F_1 = \frac{\omega_s}{\omega_1} \; ; \; \omega_s = 2\pi F_s \; ; \; \omega_1 = \frac{1}{\sqrt{L_1 C_1}} \; ;$$

$$V_o = \frac{V_1}{\sqrt{1 + Q_1^2\left(F_1 - \frac{1}{F_1}\right)^2}} \qquad \text{Load-side diode bridge} \tag{2.2}$$

There are several methods suggested in literature in varying the output voltage,

1. Phase shift angle θ [25].

2. Switching frequency F_s which changes the impedance provided by the resonant tank [7].

3. Voltage magnitudes by pulse width modulation of the active bridges at constant switching frequency F_s [26].

For very high output voltage applications, the active bridge at load side is replaced by a diode bridge. This results in the conventional series resonant converter whose output voltage is given by (2.2). It is observed that for the same switching frequency and quality ratio, the output voltage is higher with active bridge at the load side. In this Chapter the proposed converter uses phase shift angle between active bridges to control output voltage under constant switching frequency and constant voltage magnitudes.

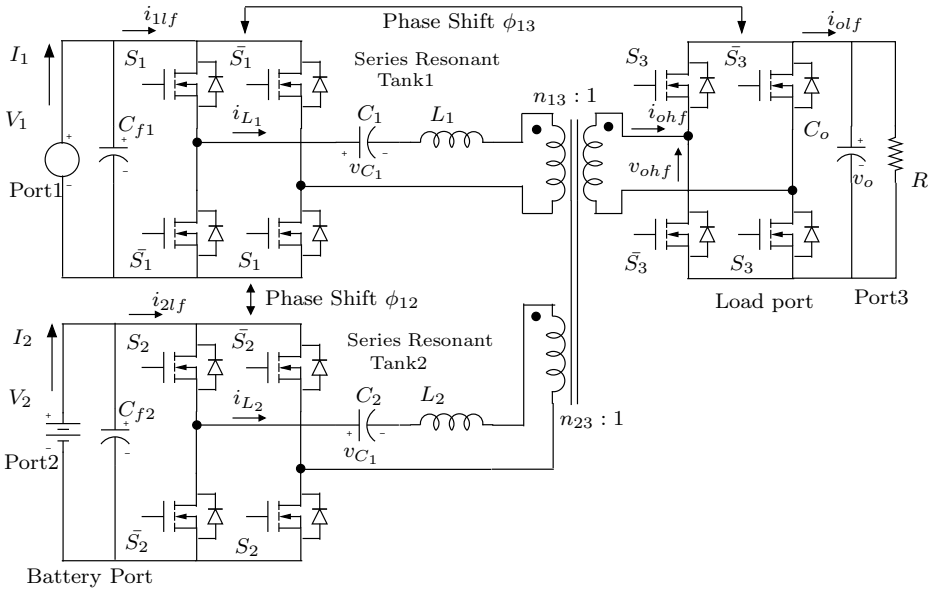

Figure 2.2: Proposed three-port series resonant converter circuit

2.1.2 Three-port series resonant converter

The proposed three-port series resonant converter circuit is shown in Fig 2.2. It has two series resonant tanks formed by L_1, C_1 and L_2, C_2 respectively. The input filter capacitors for port1 and port2 are C_{f1} and C_{f2} respectively. A constant voltage dc source such as fuel-cell can be connected to port1. Batteries are connected to port2. The switches are realized using Mosfets enabling bi-directional current flow in all ports. The switches operate at 50% duty cycle since square wave outputs are required at the output of the bridges.

Two phase-shift control variables ϕ_{13} and ϕ_{12} are considered as shown in Fig. 2.2. They control the phase-shift between the square wave outputs of the active bridges. The converter is operated at constant switching frequency F_s above resonant frequency of both resonant tanks. Steady-state operation is analyzed assuming sinusoidal tank currents and voltages due to filtering action of resonant circuits, under high quality factor. The three-winding transformer is mostly a step-up transformer whose winding1 and winding2 leakage inductances come in series with the tank inductances. Winding3 leakage inductance is neglected in the analysis presented in the following sections. The effect of this leakage inductance is discussed in detail in Section 2.5.

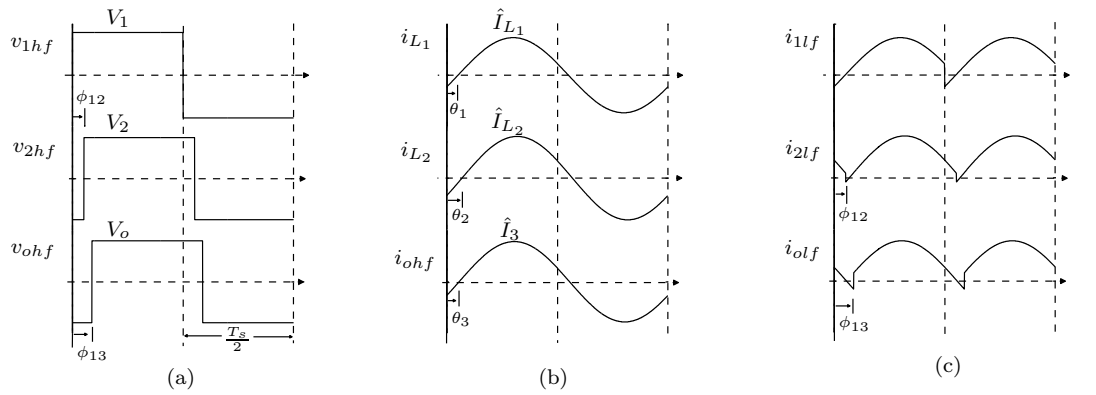

Figure 2.3: (a) PWM waveforms with definitions of phase-shift variables ϕ_{13} and ϕ_{12} (b) Tank currents and transformer winding3 current (c) Port currents before filter

2.1.3 Analysis of port voltages and currents

The square wave outputs and the corresponding phase shifts are shown in Fig. 2.3. The phase-shifts ϕ_{13} and ϕ_{12} are considered positive if v_{ohf} lags v_{1hf} and v_{2hf} lags v_{1hf} respectively. The waveforms of the tank currents and port currents before the filter are shown in Fig. 2.3b and 2.3c respectively. Phasor analysis is used to calculate the following quantities: $\hat{I}_{L_1}\angle\theta_1$, $\hat{I}_{L_2}\angle\theta_2$, $\hat{I}_{L_3}\angle\theta_3$, I_1, I_2, I_o and V_o.

The average value of the unfiltered output current i_{olf} in Fig. 2.3c is given by (2.3). Phasor analysis is used to calculate $\hat{I}_3$ (2.4), which is the peak of the transformer winding3 current. After substitution, the resultant expression for output current is (2.5).

$$I_o = \frac{2}{\pi}\hat{I}_3 \cos\left(\phi_{13} - \theta_3\right) \tag{2.3}$$

$$\text{where} \quad \hat{I}_3\angle\theta_3 = n_{13}\hat{I}_{L_1}\angle\theta_1 + n_{23}\hat{I}_{L_2}\angle\theta_2 \tag{2.4}$$

$$\hat{I}_{L_1}\angle\theta_1 = \frac{\frac{4}{\pi}V_1\angle 0 - \frac{4}{\pi}n_{13}V_o\angle\phi_{13}}{j\omega_s L_1 + \frac{1}{j\omega_s C_1}}$$

$$\hat{I}_{L_2}\angle\theta_2 = \frac{\frac{4}{\pi}V_2\angle\phi_{12} - \frac{4}{\pi}n_{23}V_o\angle\phi_{13}}{j\omega_s L_2 + \frac{1}{j\omega_s C_2}}$$

$$\text{Simplifying} \quad I_o = \frac{8}{\pi^2}\frac{n_{13}V_1}{Z_1(F_1 - \frac{1}{F_1})}\sin\phi_{13} + \frac{8}{\pi^2}\frac{n_{23}V_2}{Z_2(F_2 - \frac{1}{F_2})}\sin\left(\phi_{13} - \phi_{12}\right) \tag{2.5}$$

$$\text{where} \quad Z_i = \sqrt{\frac{L_i}{C_i}}\ ; \quad F_i = \frac{\omega_s}{\omega_i}\ ; \quad \omega_s = 2\pi f_s\ ; \quad \omega_i = \frac{1}{\sqrt{L_i C_i}}; \quad i = 1, 2 \tag{2.6}$$

If the load resistance is R, the output voltage is $V_o = I_o R$ as given by,

$$V_o = \frac{\frac{V_1}{n_{13}}}{Q_1(F_1 - \frac{1}{F_1})} \sin\phi_{13} + \frac{\frac{V_2}{n_{23}}}{Q_2(F_2 - \frac{1}{F_2})} \sin(\phi_{13} - \phi_{12}) \tag{2.7}$$

$$\text{where} \quad Q_i = \frac{Z_i}{\frac{8}{\pi^2} R n_{i3}^2} \quad \text{for} \quad i = 1, 2 \tag{2.8}$$

The average value of port1 current i_{1lf} from Fig. 2.3c can be expressed as in (2.9). Substituting the peak resonant tank1 current $\hat{I}_{L_1}$ from phasor analysis, the port1 dc current is then given by (2.10). Similar derivation is done for port2 and the results are given in (2.11) and (2.12).

$$I_1 = \frac{2}{\pi} \hat{I}_{L_1} \cos(\theta_1) \tag{2.9}$$

$$= \frac{8}{\pi^2} \frac{n_{13} V_o}{Z_1(F_1 - \frac{1}{F_1})} \sin\phi_{13} \tag{2.10}$$

$$I_2 = \frac{2}{\pi} \hat{I}_{L_2} \cos(\theta_2 - \phi_{12}) \tag{2.11}$$

$$= \frac{8}{\pi^2} \frac{n_{23} V_o}{Z_2(F_2 - \frac{1}{F_2})} \sin(\phi_{13} - \phi_{12}) \tag{2.12}$$

The analysis results are normalized to explain the characteristics of the converter, to compare with existing circuit topologies and to establish a design procedure. Consider a voltage base V_b and a power base P_b. For design calculations, the base voltage is used as the required output voltage and the base power as the maximum output power. The variable m_1 (2.13), termed as voltage conversion ratio, is defined as the normalized value of port1 input voltage referred to port1 side using turns ratio n_{13}. Similar definition applies for m_2 (2.13). The per unit output voltage is then given by (2.14).

$$m_1 = \frac{V_1}{n_{13} V_b}; \qquad m_2 = \frac{V_2}{n_{23} V_b}; \tag{2.13}$$

$$V_{o,pu} = \frac{V_o}{V_b} = \frac{m_1}{Q_1(F_1 - \frac{1}{F_1})} \sin\phi_{13} + \frac{m_2}{Q_2(F_2 - \frac{1}{F_2})} \sin(\phi_{13} - \phi_{12}) \tag{2.14}$$

A plot of per unit output voltage using (2.14) is shown in Fig. 2.4a and 2.4b. In the plot, the values of m_1 and m_2 are chosen as 1.0. The reason for this is to maximize

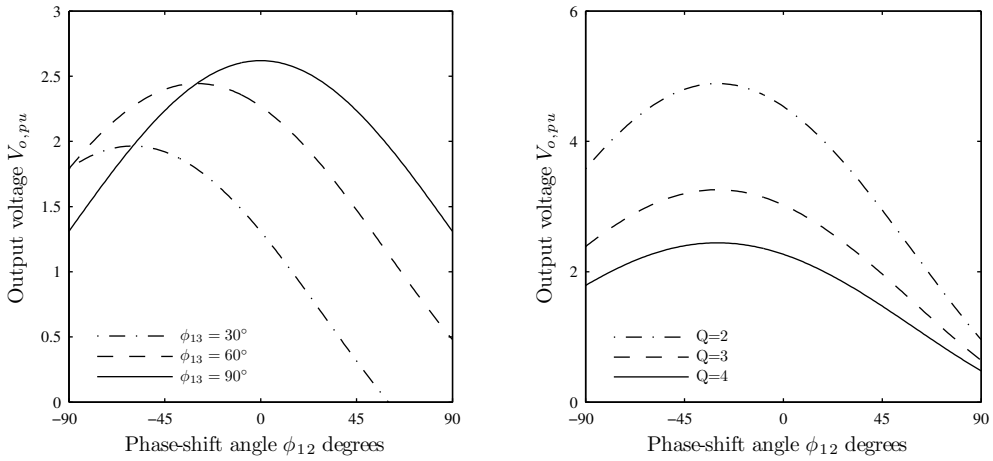

Figure 2.4: Output voltage in per unit Vs phase-shift angle ϕ_{12} for different values of (a) ϕ_{13} (b) Quality factor Q

the region of soft-switching operation as explained in Section 2.3. The values of quality factor at maximum load for both resonant tanks are chosen as 4.0. The reason for this is to minimize as much as possible the peak currents and voltages and at the same time achieve sufficiently high voltage conversion ratios. The ratio of switching frequency to resonant frequency is chosen as 1.1 to provide sufficiently high voltage gain.

From Fig. 2.4a it can be concluded that the output voltage magnitude can be varied by the phase-shift angles. From the plot in Fig. 2.4b it is clear that the output voltage is load dependent. But due to the presence of two resonant tanks the drop in voltage due to variation in quality factor is less when compared to two-port converters. It is also possible to regulate the output voltage to 1.0 *pu* by adjusting the two phase-shift angles.

2.2 Steady-state power flow equations

The port power can be calculated from the average value of the port currents. The expressions are then converted into per unit. The final port1 and port2 power in per

unit after simplifications are given by (2.15) and (2.16) respectively.

$$P_{1,pu} = \frac{P_1}{P_b} = \frac{m_1 I_{o,pu}}{Q_1\left(F_1 - \frac{1}{F_1}\right)} \sin\phi_{13} \tag{2.15}$$

$$P_{2,pu} = \frac{P_2}{P_b} = \frac{m_2 I_{o,pu}}{Q_2\left(F_2 - \frac{1}{F_2}\right)} \sin\left(\phi_{13} - \phi_{12}\right) \tag{2.16}$$

$$P_{o,pu} = P_{1,pu} + P_{2,pu} \tag{2.17}$$

$$\text{where} \quad R_b = \frac{V_b^2}{P_b}; \quad I_b = \frac{V_b}{R_b}; \quad R_{pu} = \frac{R}{R_b}; \quad I_{o,pu} = \frac{I_o}{I_b}$$

Plots of port1 and port2 power in per unit as a function of phase-shift ϕ_{13} are shown in Fig. 2.5a and 2.5b for three different quality factors. Since there are two phase-shift variables, phase-shift ϕ_{13} is varied and the phase-shift ϕ_{12} is chosen such that the output voltage in per unit $V_{o,pu}$ is kept constant at 1 pu. The output power $P_{o,pu}$ at maximum load $Q = 4.0$ is 1.0 pu. It is observed from Fig. 2.5a that the port1 power does not vary with load as long as output voltage is maintained constant. The phase-shift ϕ_{13} is kept positive for uni-directional power flow in port1. Port2 power $P_{2,pu}$ can go negative as seen from the plot and hence used as the battery port. In the plots, the values of m_1 and m_2 are chosen as 1.0 and F_1 and F_2 as 1.1.

2.3 Soft-switching operation boundary

The conditions for soft-switching operation in the active bridges can be derived from Fig. 2.3. If port1 and port2 tank currents lag their applied square wave voltages, then all switches in port1 and port2 bridges operate at Zero Voltage Switching (ZVS). This translates to $\theta_1 > 0$ for port1 and $\theta_2 - \phi_{12} > 0$ for port2. Note that angles are considered positive if lagging, in the analysis. Using phasor analysis, the soft-switching operation boundary conditions are given by (2.19) and (2.21) for port1 and port2 respectively.

$$\theta_1 > 0 \quad \text{For Port1} \tag{2.18}$$

$$V_{o,pu}\cos\phi_{13} - m_1 < 0 \quad \text{For Port1} \tag{2.19}$$

$$\theta_2 - \phi_{12} > 0 \quad \text{For Port2} \tag{2.20}$$

$$V_{o,pu}\cos\left(\phi_{13} - \phi_{12}\right) - m_2 < 0 \quad \text{For Port2} \tag{2.21}$$

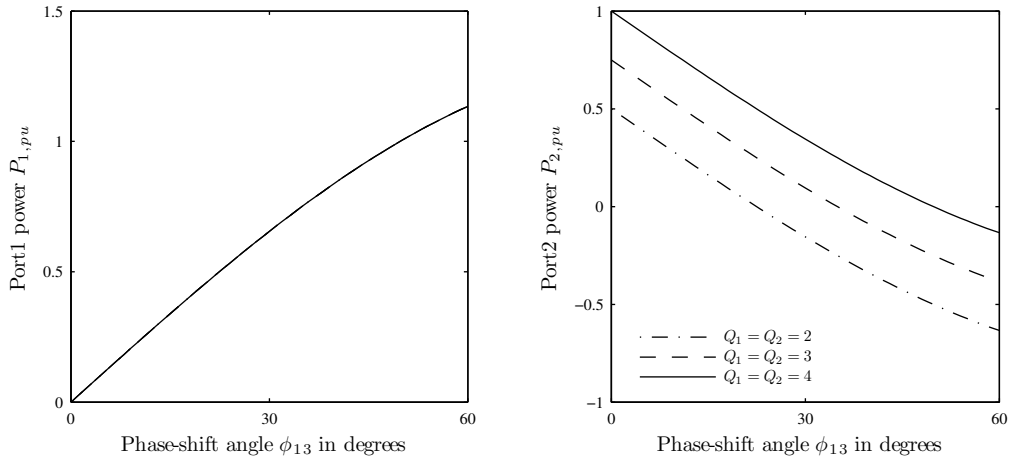

Figure 2.5: Port power in per unit Vs phase shift angle ϕ_{13} for different values of quality factor (a) Port1 (Note: The plot remains same for different values of quality factor) (b) Port2

For bridge in port3, based on the definitions of current indicated in Fig. 2.2, the condition changes to leading current for ZVS. This translates to $\theta_3 - \phi_{13} < 0$ for port3. The soft-switching operation boundary condition is given by (2.23).

$$\theta_3 - \phi_{13} < 0 \tag{2.22}$$

$$Q_1 \left(F_1 - \frac{1}{F_1}\right)(m_2 \cos(\phi_{13} - \phi_{12}) - V_{o,pu}) + Q_2 \left(F_2 - \frac{1}{F_2}\right)(m_1 \cos\phi_{13} - V_{o,pu}) < 0 \tag{2.23}$$

If $V_{o,pu}$ is regulated at 1 pu and m_1 and m_2 are chosen to be equal to or greater than 1, all switches in port1 and port2 operate at ZVS. For port3, with the same conditions, the quantities $m_1 \cos(\phi_{13} - \phi_{12})$ and $m_1 \cos\phi_{13}$ are always less than or equal to $V_{o,pu}$ and hence ZVS is possible in all switches in port3. A plot of soft-switching operation boundary using (2.23) is given in Fig. 2.6 for three values of m_1 and m_2 under varying ϕ_{13} with output voltage maintained constant at 1 pu. ZVS in port3 is particularly important since output voltage is normally higher than either of the port voltages.

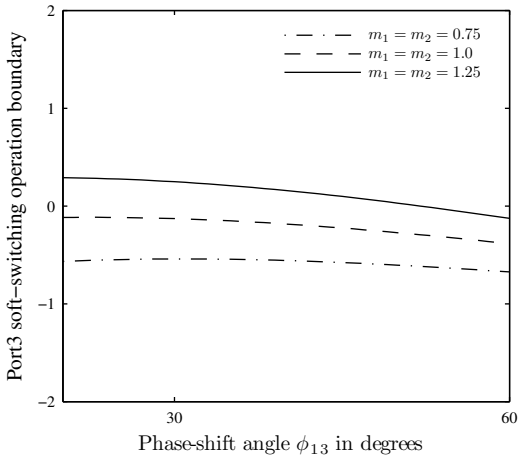

Figure 2.6: Port3 soft-switching operation boundary for various values of m_1 and m_2

Hence in design m_1 and m_2 are chosen to be 1.

2.4 Peak currents in tank circuit

The peak tank currents $\hat{I}_{L_1}$ and $\hat{I}_{L_2}$ are normalized with respect to corresponding tank impedance. The final expressions are given by (2.24) and (2.25). A plot of port2 peak current as a function of ϕ_{13} for various values of load quality factors is shown in Fig. 2.7. In this plot ϕ_{12} is chosen in such a way to maintain output voltage constant at 1 *pu*. Also, the values of m_1 and m_2 are chosen as 1.0. From Fig. 2.7 and Fig. 2.5b, it can be observed that port2 peak tank current is maximum when it is supplying the full load and is minimum when it is not supplying any power. In Chapter 4, a specific design is explained and peak currents are calculated for all operating conditions.

$$\hat{I}_{L_1(norm)} = \frac{4}{\pi}\sqrt{1 + \left(\frac{V_{o,pu}}{m_1}\right)^2 - \frac{2V_{o,pu}}{m_1}\cos\phi_{13}} \tag{2.24}$$

$$\hat{I}_{L_2(norm)} = \frac{4}{\pi}\sqrt{1 + \left(\frac{V_{o,pu}}{m_2}\right)^2 - \frac{2V_{o,pu}}{m_2}\cos\left(\phi_{13} - \phi_{12}\right)} \tag{2.25}$$

$$\text{where} \quad \hat{I}_{L_i(norm)} = \frac{\hat{I}_{L_i}}{Z_i\left(F_i - \frac{1}{F_i}\right)} \quad ; \quad i = 1, 2 \tag{2.26}$$

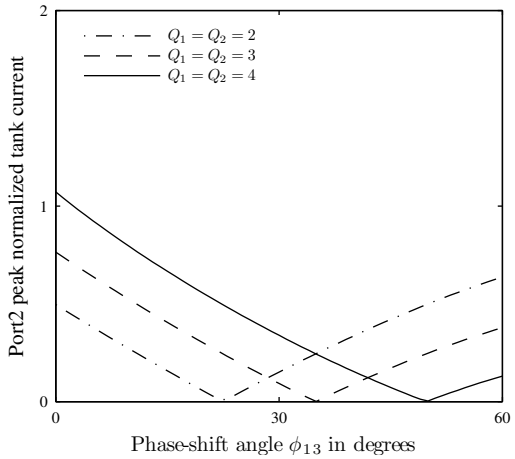

Figure 2.7: Port2 peak normalized current vs ϕ_{13} for various values of load quality factors

It is clear from the plot in Fig. 2.7 that the peak currents increase as the quality factor is increased. This is one of the drawbacks of resonant converters. High quality factor is required for validity of sinusoidal approximation. A trade-off is required in choosing Q at full load to justify sinusoidal approximation and to achieve lower peak currents. In this thesis the quality factor at full load is chosen as 4.0.

2.5 Three-winding transformer model

In this section, the effect of the non-idealities of the three-winding transformer is discussed. Specifically, the effect of the magnetizing inductance L_m and the three leakage inductances L_{lk1}, L_{lk2} and L_{lk3}, as shown in Fig. 2.8, on the output voltage and port power expressions are examined. As explained in Section 2.1.2, the winding1 and winding 2 leakage inductances appear in series with the resonant inductors and the values L_1, L_2 include the value of these leakage inductances as shown in Fig. 2.8. To analyze the power flow it is necessary to convert the T-model of the transformer into a π model or an extended cantilever model [11].

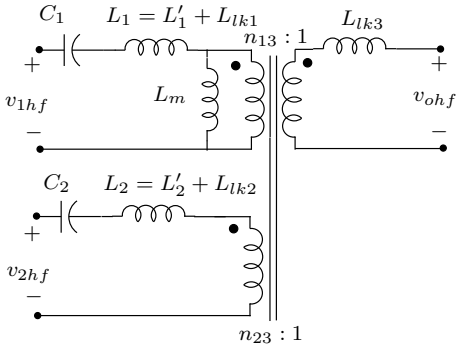

Figure 2.8: Three-winding transformer model including the leakage inductances

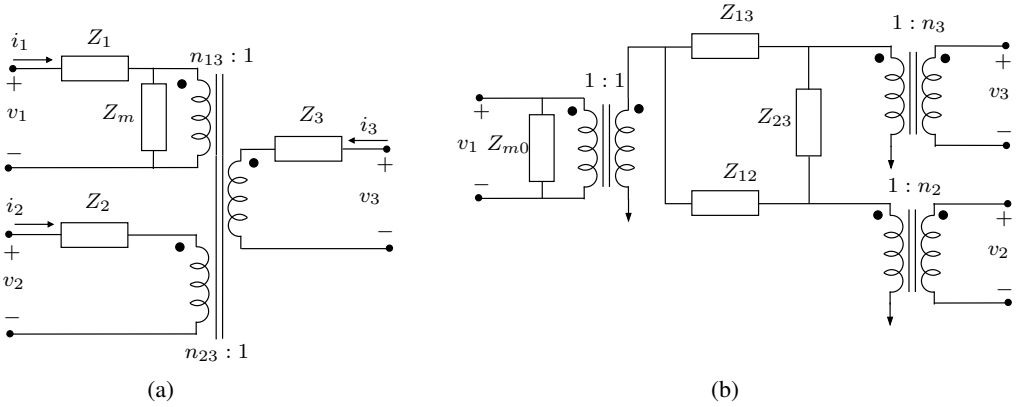

Figure 2.9: Three-winding transformer (a) T-equivalent circuit (b) Extended Cantilever circuit or π equivalent model

2.5.1 Extended cantilever model of three-winding transformer

Multi-winding transformers are commonly used in multi-output dc power supplies. In the context of cross-regulation i.e., the effect of closed loop control in one output over the other output, an extended cantilever model has been proposed in [11]. This model along with the T-model is shown in Fig. 2.9. There are three separate two-winding transformers with the impedances connected in between. The magnetizing inductance is reflected to one of the transformers. Instead of inductances, Fig. 2.9 shows impedances since the three-port converter has resonant circuit elements. The relation between the parameters derived in [11] using inductances is extended here using the impedances of the resonant tanks.

Using the T-model in Fig. 2.9, we can write,

$$\begin{pmatrix} v_1 \\ v_2 \\ v_3 \end{pmatrix} = \begin{pmatrix} Z_1 + Z_m & Z_m \frac{n_{23}}{n_{13}} & Z_m \frac{1}{n_{13}} \\ Z_m \frac{n_{23}}{n_{13}} & Z_2 + Z_m \frac{n_{23}^2}{n_{13}^2} & Z_m \frac{n_{23}}{n_{13}^2} \\ Z_m \frac{1}{n_{13}} & Z_m \frac{n_{23}}{n_{13}^2} & Z_3 + Z_m \frac{1}{n_{13}^2} \end{pmatrix} \begin{pmatrix} i_1 \\ i_2 \\ i_3 \end{pmatrix} \tag{2.27}$$

$$V = ZI = (z_{jk}) \tag{2.28}$$

$$Y = Z^{-1} = (b_{jk}) \quad j \neq k \tag{2.29}$$

Then the elements of the equivalent model in Fig. 2.9 can be represented as,

$$Z_{m0} = Z_m + Z_1 \tag{2.30}$$

$$n_2 = \frac{z_{12}}{z_{11}} = \frac{Z_m}{Z_1 + Z_m} \frac{n_{23}}{n_{13}} \tag{2.31}$$

$$n_1 = \frac{z_{13}}{z_{11}} = \frac{Z_m}{Z_1 + Z_m} \frac{1}{n_{13}} \tag{2.32}$$

$$Z_{jk} = -\frac{1}{n_j n_k b_{jk}} \quad j \neq k \tag{2.33}$$

Using (2.33), the values of Z_{12}, Z_{13} and Z_{23} in the π equivalent model can be determined. The parameters in the extended cantilever model can be directly measured, but since the three-port converter has external inductance and capacitor connected in series, the parameters of the T-model of the transformer are individually determined first and then the circuit in Fig. 2.8 is transformed to the extended cantilever model.

2.5.2 Power flow equations using the equivalent model

The power flow between port1 and port3 assuming sinusoidal voltages and currents is given by,

$$P_{13} = \frac{16}{\pi^2} \frac{V_1 V_2 \frac{1}{n_2}}{Z_{13}} \sin \phi_{13} \tag{2.34}$$

$$v_1 = \frac{4}{\pi} V_1 \sin \omega_s t \tag{2.35}$$

$$v_2 = \frac{4}{\pi} V_2 \sin (\omega_s t - \phi_{13}) \tag{2.36}$$

$$Z_{13} = \left(\frac{Z_1 + Z_m}{Z_m} \right) \left(\frac{Z_1 Z_m (Z_2 + n_{23}^2 Z_3) + n_{13}^2 Z_2 Z_3 (Z_1 + Z_m)}{Z_2 Z_m} \right) \tag{2.37}$$

Simplifying this equation and representing in per unit, the power flow between port1 and port3 $P_{13,pu}$ (2.38) is obtained.

$$P_{13,pu} = \frac{m_1 I_{o,pu} \quad \sin\phi_{13}}{Q_1\left(F_1 - \frac{1}{F_1}\right) + Q_{lk3}\left(1 + \frac{Q_1}{Q_m}\left(F_1 - \frac{1}{F_1}\right) + \frac{Q_1}{Q_2}\frac{\left(F_1 - \frac{1}{F_1}\right)}{\left(F_2 - \frac{1}{F_2}\right)}\right)} \tag{2.38}$$

$$Q_{lk3} = \frac{\omega_s L_{lk3}}{\frac{8}{\pi^2}R} \; ; \quad Q_m = \frac{\omega_s L_m}{\frac{8}{\pi^2}n_{13}^2 R} \tag{2.39}$$

Similarly the two other power flow equations are derived and given in (2.40) and (2.41) respectively. Using the power flow between ports, the total power from each of the ports can be determined using (2.42-2.44).

$$P_{12,pu} = \frac{m_1 m_2 / R_{pu} \quad \sin\phi_{12}}{Q_1\left(F_1 - \frac{1}{F_1}\right) + Q_2\left(F_2 - \frac{1}{F_2}\right)\left(1 + \frac{Q_1}{Q_m}\left(F_1 - \frac{1}{F_1}\right) + \frac{Q_1}{Q_{lk3}}\left(F_1 - \frac{1}{F_1}\right)\right)} \tag{2.40}$$

$$P_{23,pu} = \frac{m_2 I_{o,pu} \quad \sin\left(\phi_{13} - \phi_{12}\right)}{Q_2\left(F_2 - \frac{1}{F_2}\right) + Q_{lk3}\left(1 + \frac{Q_2}{Q_m}\left(F_2 - \frac{1}{F_2}\right) + \frac{Q_2}{Q_1}\frac{\left(F_2 - \frac{1}{F_2}\right)}{\left(F_1 - \frac{1}{F_1}\right)}\right)} \tag{2.41}$$

$$P_{1,pu} = P_{13,pu} + P_{12,pu} \tag{2.42}$$

$$P_{2,pu} = P_{23,pu} - P_{12,pu} \tag{2.43}$$

$$P_{o,pu} = P_{1,pu} + P_{2,pu} \tag{2.44}$$

To summarize, following are the steps involved in determining the extended cantilever model:

1. Measure the parameters in the T-model of the transformer i.e., L_{lk1}, L_{lk2}, L_{lk3} and L_m.

2. Construct the T-model along with the resonant circuit elements as in Fig. 2.8.

3. Transform the T-model to the extended cantilever model and determine the equivalent circuit parameters Z_{m0}, Z_{12}, Z_{23}, Z_{13}, n_2 and n_3.

4. Calculate the power flow between ports and hence the net power flow from each of the ports

The magnetizing inductance L_m is very large when compared to the impedance offered by the resonant tank circuit and hence $Q_m \gg Q_1 \left(F_1 - \frac{1}{F_1}\right)$. Since the resonant tank circuit operates at high quality factor $Q \geq 4$, it can be assumed that $Q_{lk3} \ll Q_i \left(F_i - \frac{1}{F_i}\right)$ with $F_i = 1.1$. With the above two simplifying assumptions along with the high impedance between port1 and port2 contributed by Q_1 and Q_2 in (2.40), the power flow between port1 and port2, $P_{12,pu}$, is negligible. Also the power flow between port1 and port3, $P_{13,pu}$, reduces to $P_{1,pu}$ in (2.15). In the following sections, these assumptions are applied. In Section 4.2.3, a plot of the phase shifts with and without the leakage inductance L_{lk3} is given.

2.6 Conclusion

In this chapter the three-port series resonant converter is proposed. Steady state analysis is presented to determine the power flow equations in the three-port converter. It can be concluded from the analysis that the power flow between ports in any direction can be controlled by the phase-shift angles. Further, soft-switching operation is possible in the full operating range of the converter provided the design constraints are met. The effect of non-idealities in the three-winding transformer on the power flow between ports are discussed using an equivalent model.

Chapter 3

Three-port Series Resonant Converter - Dynamic Analysis

Dynamic analysis of the proposed three-port series resonant converter is presented in this Chapter. The analysis aids in designing controller for regulating power flow in the converter. The analysis approach uses averaging and time-scaling with sinusoidal approximation. Different approaches for feedback controller design are also discussed in this Chapter.

3.1 Dynamic equations for the converter

The triple active bridge series resonant converter is shown in Fig. 3.1. Dynamic equations are given for the resonant tank currents, tank voltages and the output voltage (3.1-3.5). The variable ω_s is defined as $\omega_s = 2\pi F_s$ where F_s is the switching frequency. The voltage polarity and current direction are indicated in the Fig. 3.1.

$$L_1\dot{i}_{L_1} = V_1 \text{ sgn}(\sin(\omega_s t)) - v_{C_1} - n_{13}v_o \text{ sgn}(\sin(\omega_s t - \phi_{13})) \tag{3.1}$$

$$C_1\dot{v}_{C_1} = i_{L_1} \tag{3.2}$$

$$L_2\dot{i}_{L_2} = V_2 \text{ sgn}(\sin(\omega_s t - \phi_{12})) - v_{C_2} - n_{23}v_o \text{ sgn}(\sin(\omega_s t - \phi_{13})) \tag{3.3}$$

$$C_2\dot{v}_{C_2} = i_{L_2} \tag{3.4}$$

$$C_o\dot{v}_o = (n_{13}i_{L_1} + n_{23}i_{L_2}) \text{ sgn}(\sin(\omega_s t - \phi_{13})) - \frac{v_o}{R} \tag{3.5}$$

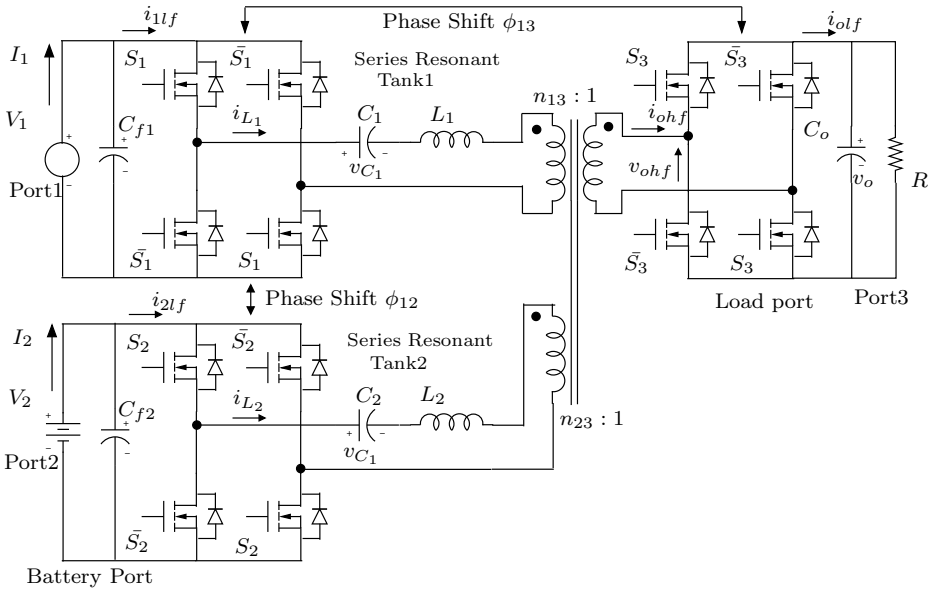

Figure 3.1: Three-port series-resonant converter circuit indicating the dynamic variables

The function $sgn(.)$ is the signum function which denotes the sign of the signal (3.1). The resonant inductors' series resistance and the on-state resistance $r_{ds(on)}$ of the Mosfets are not included in the equations.

$$\text{sgn}(x) = \begin{cases} 1 & \text{if } x > 0 \\ -1 & \text{if } x > 0 \\ 0 & \text{if } x = 0 \end{cases}$$

3.2 Averaged model of three-port series resonant converter

To simplify the averaging process the following assumptions are made:

1. The switching frequency of the converter is kept above the resonant frequency of both the resonant tanks i.e., $F_1, F_2 > 1$. This also ensures soft-switching operation as discussed in Chapter 2.

2. Due to the filtering action of the resonant tanks, the tank currents and voltages are assumed sinusoidal

With the above assumptions, an averaged model for the converter can be derived. The following section explains the method adopted for averaging this circuit.

3.2.1 Generalized averaging method

The generalized averaging method was proposed in [27] to analyze all types of switching converters. It is briefly explained here from [27] and applied for the proposed converter. A waveform $x(\cdot)$ can be approximated on the interval $(t-T, t]$ with a Fourier series representation of the form

$$x(t-T+s) = \sum_k < x >_k (t) e^{jk\omega_s(t-T+s)} \tag{3.6}$$

where the sum is over all integers k, $\omega_s = 2\pi/T, s \in (0, T]$ and $< x >_k (t)$ are complex Fourier coefficients which can also be referred to as phasors. These Fourier coefficients are functions of time since the interval under consideration slides as a function of time. The k^{th} coefficient is determined by

$$< x >_k (t) = \frac{1}{T} \int_o^T x(t-T+s) e^{-jk\omega_s(t-T+s)} \tag{3.7}$$

This type of averaging method is used in power electronic circuits where the model has some periodic time-dependence. In this converter it is the function $\text{sgn}(\sin \omega_s t)$ having a period $T = 2\pi/\omega_s = 1/F_s$ where F_s is the switching frequency. Some applications of this method are given in [28, 29, 30, 31, 32, 33]

3.2.2 Application to three-port converter

Following assumption 2, the states can be approximated with the fundamental frequency terms in the Fourier series (3.6). This can be obtained by application of the operator $< \cdot >_1$ and $< \cdot >_0$ to the model (3.1-3.5). The paper [27] also gives some properties of the Fourier coefficients (3.7) which will be used in further derivations.

$$\begin{aligned} \left\langle \dot{i}_{L_1} \right\rangle_1 = &-j\omega_s \langle i_{L_1} \rangle_1 + \frac{1}{L_1} V_1 \ \langle \text{sgn}(\sin(\omega_s t)) \rangle_1 - \frac{1}{L_1} \langle v_{C_1} \rangle_1 \\ &- \frac{n_{13}}{L_1} \langle v_o \ \text{sgn}(\sin(\omega_s t - \phi_{13})) \rangle_1 \end{aligned} \tag{3.8}$$

$$\langle \dot{v}_{C_1} \rangle_1 = -j\omega_s \langle v_{C_1} \rangle_1 + \frac{1}{C_1} \langle i_{L_1} \rangle_1 \tag{3.9}$$

$$\left\langle \dot{i}_{L_2} \right\rangle_1 = -j\omega_s \left\langle i_{L_2} \right\rangle_1 + \frac{1}{L_2} V_2 \ \left\langle \text{sgn}(\sin(\omega_s t - \phi_{12})) \right\rangle_1 - \frac{1}{L_2} \left\langle v_{C_2} \right\rangle_1 - \frac{n_{23}}{L_2} \left\langle v_o \ \text{sgn}(\sin(\omega_s t - \phi_{13})) \right\rangle_1 \tag{3.10}$$

$$\left\langle \dot{v}_{C_2} \right\rangle_1 = -j\omega_s \left\langle v_{C_2} \right\rangle_1 + \frac{1}{C_2} \left\langle i_{L_2} \right\rangle_1 \tag{3.11}$$

$$\left\langle \dot{v}_o \right\rangle_0 = \frac{1}{C_o} \left\langle (n_{13} i_{L_1} + n_{23} i_{L_2}) \ \text{sgn}(\sin(\omega_s t - \phi_{13})) \right\rangle_0 - \frac{\left\langle v_o \right\rangle_0}{RC_o} \tag{3.12}$$

The evaluation of Fourier series coefficients for the important terms in (3.8-3.12) is given below.

$$\left\langle \text{sgn} \sin(\omega_s t - \phi_{13}) \right\rangle_1 = -j\frac{2}{\pi} e^{-j\phi_{13}} \tag{3.13}$$

$$\left\langle v_o \ \text{sgn}(\sin(\omega_s t - \phi_{13})) \right\rangle_1 = \left\langle v_o \right\rangle_0 \left\langle \text{sgn}(\sin(\omega_s t - \phi_{13})) \right\rangle_1 \tag{3.14}$$

$$\left\langle (i_{L_1} + i_{L_2}) \text{sgn}(\sin(\omega_s t - \phi_{13})) \right\rangle_0 = \left\langle (i_{L_1} + i_{L_2}) \right\rangle_{-1} \left\langle \text{sgn}(\sin(\omega_s t - \phi_{13})) \right\rangle_1 + \left\langle (i_{L_1} + i_{L_2}) \right\rangle_1 \left\langle \text{sgn}(\sin(\omega_s t - \phi_{13})) \right\rangle_{-1} \tag{3.15}$$

The generalized averaging method is applied to the converter with the assumption that only the first harmonics of the tank currents and voltages are retained. These are denoted by the phasors as in $I_{L_1} = \hat{I}_{L_1} \angle \theta_1$. In these phasors, both the magnitude and phase vary with time. The system can then be represented using the tank current and voltage phasors as in (3.16)-(3.20) usually referred to in literature as dynamic phasor model. The equations (3.8-3.12) can be rewritten substituting the terms evaluated in (3.13-3.15).

$$L_1 \dot{I}_{L_1} = -j\omega_s I_{L_1} - j\frac{2}{\pi} V_1 - V_{C_1} + n_{13} V_o j\frac{2}{\pi} e^{-j\phi_{13}} \tag{3.16}$$

$$C_1 \dot{V}_{C_1} = -j\omega_s V_{C_1} - I_{L_1} \tag{3.17}$$

$$L_2 \dot{I}_{L_2} = -j\omega_s I_{L_2} - j\frac{2}{\pi} V_2 e^{-j\phi_{12}} - V_{C_2} + n_{23} V_o j\frac{2}{\pi} e^{-j\phi_{13}} \tag{3.18}$$

$$C_2 \dot{V}_{C_2} = -j\omega_s V_{C_2} - I_{L_2} \tag{3.19}$$

$$C_o \dot{v}_o = -j\frac{2}{\pi} n_{13} I_{L_1} e^{-j\phi_{13}} + j\frac{2}{\pi} n_{13} I_{L_1} e^{j\phi_{13}} - j\frac{2}{\pi} n_{23} I_{L_2} e^{-j\phi_{13}} + j\frac{2}{\pi} n_{23} I_{L_2} e^{j\phi_{13}} - \frac{v_o}{R} \tag{3.20}$$

It is known that the Fourier series coefficient $\langle\cdot\rangle_1$ is a complex value. Hence the state equations (3.16-3.20) can be expanded into 9 state equations considering the dynamics of both the real and imaginary terms of the coefficients. The states are redefined as follows,

$$\langle i_{L_1}\rangle_1 = x_1 + jx_2 \tag{3.21}$$

$$\langle v_{C_1}\rangle_1 = x_3 + jx_4 \tag{3.22}$$

$$\langle i_{L_2}\rangle_1 = x_5 + jx_6 \tag{3.23}$$

$$\langle v_{C_2}\rangle_1 = x_7 + jx_8 \tag{3.24}$$

$$\langle v_o\rangle_0 = x_9 \tag{3.25}$$

After simplification, the final state space equations with 9 states are given by (3.26-3.34),

$$\dot{x}_1 = \omega_s x_2 - \frac{1}{L_1}x_3 + \frac{1}{L_1}\frac{2}{\pi}n_{13}x_9\sin\phi_{13} \tag{3.26}$$

$$\dot{x}_2 = -\omega_s x_1 - \frac{1}{L_1}x_4 + \frac{1}{L_1}\frac{2}{\pi}n_{13}x_9\cos\phi_{13} - \frac{2}{\pi}\frac{V_1}{L_1} \tag{3.27}$$

$$\dot{x}_3 = \omega_s x_4 + \frac{1}{C_1}x_1 \tag{3.28}$$

$$\dot{x}_4 = -\omega_s x_3 + \frac{1}{C_1}x_2 \tag{3.29}$$

$$\dot{x}_5 = \omega_s x_6 - \frac{1}{L_2}x_7 + \frac{1}{L_2}\frac{2}{\pi}n_{23}x_9\sin\phi_{13} - \frac{2}{\pi}\frac{V_2}{L_2}\sin\phi_{12} \tag{3.30}$$

$$\dot{x}_6 = -\omega_s x_5 - \frac{1}{L_2}x_8 + \frac{1}{L_2}\frac{2}{\pi}n_{23}x_9\cos\phi_{13} - \frac{2}{\pi}\frac{V_2}{L_2}\cos\phi_{12} \tag{3.31}$$

$$\dot{x}_7 = \omega_s x_8 + \frac{1}{C_2}x_5 \tag{3.32}$$

$$\dot{x}_8 = -\omega_s x_7 + \frac{1}{C_2}x_6 \tag{3.33}$$

$$\begin{aligned}\dot{x}_9 = &-\frac{1}{C_o}\frac{4}{\pi}n_{13}x_1\sin\phi_{13} - \frac{1}{C_o}\frac{4}{\pi}n_{23}x_5\sin\phi_{13}\\ &-\frac{1}{C_o}\frac{4}{\pi}n_{13}x_2\cos\phi_{13} - \frac{1}{C_o}\frac{4}{\pi}n_{23}x_6\cos\phi_{13} - \frac{x_9}{RC_o}\end{aligned} \tag{3.34}$$

3.3 Normalization of the state equations

The system of equations (3.26-3.34) can be normalized to obtain dimensionless expressions. The normalized variables for resonant tank1 are defined in (3.35-3.36). Similar definitions apply for resonant tank2. The normalized output voltage state is given in (3.39). The time t is also normalized by using $t_n = t/(RC_o)$.

$$x_{1n} = \frac{x_1}{V_1/\sqrt{\frac{L_1}{C_1}}} \quad x_{5n} = \frac{x_5}{V_2/\sqrt{\frac{L_2}{C_2}}} \tag{3.35}$$

$$x_{2n} = \frac{x_2}{V_1/\sqrt{\frac{L_1}{C_1}}} \quad x_{6n} = \frac{x_6}{V_2/\sqrt{\frac{L_2}{C_2}}} \tag{3.36}$$

$$x_{3n} = \frac{x_3}{V_1} \quad x_{7n} = \frac{x_7}{V_2} \tag{3.37}$$

$$x_{4n} = \frac{x_4}{V_1} \quad x_{8n} = \frac{x_8}{V_2} \tag{3.38}$$

$$x_{9n} = \frac{x_9}{\frac{V_1}{n_{13}m_1}} = \frac{x_9}{\frac{V_2}{n_{23}m_2}} \tag{3.39}$$

The normalized state equations (3.40-3.48) are obtained by substituting the defintions for the normalized state variables including the normalized time t_n.

$$\epsilon\dot{x}_{1n} = F_1 x_{2n} - x_{3n} + \frac{2}{\pi}\frac{1}{m_1}x_{9n}\sin\phi_{13} \tag{3.40}$$

$$\epsilon\dot{x}_{2n} = -F_1 x_{1n} - x_{4n} + \frac{2}{\pi}\frac{1}{m_1}x_{9n}\cos\phi_{13} - \frac{2}{\pi} \tag{3.41}$$

$$\epsilon\dot{x}_{3n} = F_1 x_{4n} + x_{1n} \tag{3.42}$$

$$\epsilon\dot{x}_{4n} = -F_1 x_{3n} + x_{2n} \tag{3.43}$$

$$\epsilon\dot{x}_{5n} = F_2 x_{6n} - x_{7n} + \frac{2}{\pi}\frac{1}{m_2}x_{9n}\sin\phi_{13} - \frac{2}{\pi}\sin\phi_{12} \tag{3.44}$$

$$\epsilon\dot{x}_{6n} = -F_2 x_{5n} - x_{8n} + \frac{2}{\pi}\frac{1}{m_2}x_{9n}\cos\phi_{13} - \frac{2}{\pi}\cos\phi_{12} \tag{3.45}$$

$$\epsilon\dot{x}_{7n} = F_2 x_{8n} + x_{5n} \tag{3.46}$$

$$\epsilon\dot{x}_{8n} = -F_2 x_{7n} + x_{6n} \tag{3.47}$$

$$\begin{aligned}\dot{x}_{9n} = &-\frac{4}{\pi}\frac{m_1}{Q_1}x_{1n}\sin\phi_{13} - \frac{4}{\pi}\frac{m_1}{Q_1}x_{2n}\cos\phi_{13} \\ &-\frac{4}{\pi}\frac{m_2}{Q_2}x_{5n}\sin\phi_{13} - \frac{4}{\pi}\frac{m_2}{Q_2}x_{6n}\cos\phi_{13} - x_{9n}\end{aligned} \tag{3.48}$$

3.3.1 Steady-state results using averaged model

Steady state solutions can be obtained by equating the dynamics of (3.40-3.48) to zero. Steady state solution depends on the constant input voltages V_1, V_2 and the load resistance R. The phase shifts ϕ_{12} and ϕ_{13} are the inputs used for control. The steady-state value X_{9n} is given in (3.49) which is same as the solution obtained in (2.14). The solutions of the remaining states as a function of X_{9n} are given in (3.50-3.57).

$$X_{9n} = \frac{m_1}{Q_1\left(F_1 - \frac{1}{F_1}\right)}\sin\phi_{13} + \frac{m_2}{Q_2\left(F_2 - \frac{1}{F_2}\right)}\sin\left(\phi_{13} - \phi_{12}\right) \tag{3.49}$$

$$X_{1n} = \frac{2}{\pi}\frac{1}{\left(F_1 - \frac{1}{F_1}\right)}\left[-1 + \frac{1}{m_1}X_{9n}\cos\phi_{13}\right] \tag{3.50}$$

$$X_{2n} = \frac{2}{\pi}\frac{1}{\left(F_1 - \frac{1}{F_1}\right)}\left[-\frac{1}{m_1}X_{9n}\sin\phi_{13}\right] \tag{3.51}$$

$$X_{3n} = \frac{1}{F_1}X_{2n} \tag{3.52}$$

$$X_{4n} = -\frac{1}{F_1}X_{1n} \tag{3.53}$$

$$X_{5n} = \frac{2}{\pi}\frac{1}{\left(F_2 - \frac{1}{F_2}\right)}\left[-\cos\phi_{12} + \frac{1}{m_2}X_{9n}\cos\phi_{13}\right] \tag{3.54}$$

$$X_{6n} = \frac{2}{\pi}\frac{1}{\left(F_2 - \frac{1}{F_2}\right)}\left[\sin\phi_{12} - \frac{1}{m_2}X_{9n}\sin\phi_{13}\right] \tag{3.55}$$

$$X_{7n} = \frac{1}{F_2}X_{6n} \tag{3.56}$$

$$X_{8n} = -\frac{1}{F_2}X_{5n} \tag{3.57}$$

3.4 Time-Scaling for the dynamic system

The original system (3.1-3.5) has been converted to the autonomous system (3.40-3.48) using averaging, sinusoidal approximation and normalization. These equations can be now represented in a standard singular perturbation model (3.58-3.59) with a small

parameter ϵ defined as $\sqrt{L_i C_i}/RC_o$.

$$\dot{x} = f(x, z, \epsilon) \tag{3.58}$$

$$\epsilon \dot{z} = g(x, z, \epsilon) \tag{3.59}$$

$$\text{where } z = [x_1\ x_2\ x_3\ x_4\ x_5\ x_6\ x_7\ x_8\ x_9]^T\ ;\ x = x_9 \tag{3.60}$$

$$\epsilon = \frac{\sqrt{L_i C_i}}{RC_o}\ i = 1, 2 \tag{3.61}$$

Considering that in the design, the resonant frequency of both the resonant tanks are almost the same, the parameter ϵ remains the same for both resonant tanks. The capacitor C_o is large to filter the switching ripple current at the output port. The time constant RC_o is very large when compared to the resonant tank period. In the hardware prototype it is 10^5 times larger than the resonant tank time constant. Hence the perturbation parameter ϵ is very small.

Setting $\epsilon = 0$ in (3.59) gives the solution for states as in (3.50-3.57) considering the inputs to the system, the phase shifts ϕ_{12} and ϕ_{13}, are kept constant. This solution as a function of the state x is referred to as the quasi-steady state $\tilde{z}$. These equations are given in (3.50-3.57). The boundary-layer system [34] is found to be globally exponentially stable if the series resistances of the inductor, Mosfet on-state resistance are included in the state equations. The reduced model can be written as in (3.62) where u^* is the pseudo-control input. This has an unique solution as given in (3.64).

$$\dot{x} = u^* - x \tag{3.62}$$

$$\text{where } \ u^* = \frac{m_1}{Q_1(F_1 - \frac{1}{F_1})} \sin(\phi_{13}) + \frac{m_2}{Q_2(F_2 - \frac{1}{F_2})} \sin(\phi_{13} - \phi_{12}) \tag{3.63}$$

$$x(t_n) = u^* \left(1 - e^{-t_n}\right) \qquad x(0) = 0 \tag{3.64}$$

3.5 Controller design

Since the system can be represented in two timescales, the overall feedback system can be represented as in Fig. 3.2 using a static non-linear block whose input is the pseudo-control input $I_{o(ref)}$. The phase-shifts ϕ_{12} and ϕ_{13} are calculated from (3.65) and (3.66)

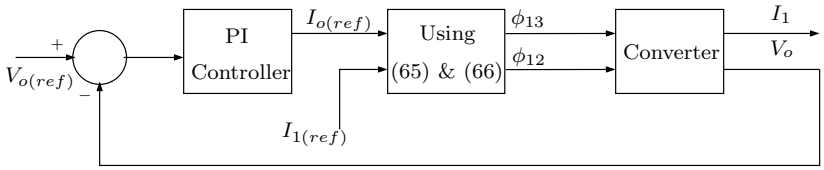

Figure 3.2: Block diagram for controlling the three-port converter

which are obtained by converting back the normalized state equations.

$$\phi_{13} = \sin^{-1}\left(\frac{I_{1(ref)}Z_1(F_1-\frac{1}{F_1})}{V_{o(ref)}n_{13}\frac{8}{\pi^2}}\right) \tag{3.65}$$

$$\phi_{12} = \phi_{13} - \sin^{-1}\left(\frac{I_{o(ref)} - \frac{8}{\pi^2}\frac{n_{13}V_1}{Z_1(F_1-\frac{1}{F_1})}\sin(\phi_{13})}{\frac{8}{\pi^2}\frac{n_{23}V_2}{Z_2(F_2-\frac{1}{F_2})}}\right) \tag{3.66}$$

It is to be noted that the phase-shifts ϕ_{13} and ϕ_{12} from equations (3.65)-(3.66) do not depend on the load. A block diagram of control is shown in Fig. 3.2. A proportional plus integral controller (PI) is used whose output is $I_{o(ref)}$. Externally a reference is set for port1 current $I_{1(ref)}$. The static block in Fig. 3.2 converts the reference currents to phase-shifts. The PI controller is designed for the worst-case load. The static block and the PI controller block can be implemented using FPGA or DSP. Since port1 current I_1 is not regulated in closed loop, a steady-state error is introduced between the reference I_{1ref} and the actual current. But the control restricts sudden transients in the current. The steady-state error may be contributed by sinusoidal approximation, parameter variations and conduction losses. This error can be removed by adding another slow control loop to regulate the port1 current. Simulation and experimental results using this method of control is given in the following Chapter.

Nonlinear dissipative controller for a 2-port series resonant converter with control input as switching frequency is proposed in [31] and [28]. A similar technique is adopted in this 3-port converter with the difference being the control variable. In this case, it will be the phase-shifts rather than the switching frequency. The state equation with the pseudo-control input is given in (3.67). Consider $G = \frac{1}{R}$ as the unknown conductance of the circut and $\hat{G}$ its estimate. The error signal e is defined as $e = v_o - V_o^*$. Consider

the quadratic function 3.68 with the error terms in the state and the load. The function relates to the energy in the output capacitor C_o.

$$\dot{v}_o = \frac{I^*}{C_o} - \frac{v_o}{RC_o} \tag{3.67}$$

$$V = \frac{1}{2}C_o e^2 + \frac{V_o^*}{2g}\left(\hat{G} - G\right)^2 \tag{3.68}$$

$$\frac{d\hat{G}}{dt} = -ge \tag{3.69}$$

$$\dot{V} = eI^* - V_o^*\hat{G}e - Ge^2 \tag{3.70}$$

The pseudo-control input I^* can be calculated from e using (3.71).

$$\text{Let} \quad I^* = \left(V_o^*\hat{G} - k\right)e \tag{3.71}$$

$$\dot{V} = -\left(G + k\right)e^2 \tag{3.72}$$

By appropriately choosing the quantities g and k, the controller can be designed. The phase-shifts can be calculated from (3.65) and (3.66). The characteristic polynomial is $C_o s^2 + (G + k)s + V_o^* g$, the dominant real pole being $-V_o^*/(k + G)$. The simulation results of this type of controller are given in the following Chapter. It is to be noted that $\dot{V}$ is negative semi-definite i.e., the output voltage exponentially converges to the desired value, but the estimate $\hat{G}$ may not converge to the actual value [28].

3.6 Conclusion

In this chapter the dynamic model of the three-port series resonant converter is presented. It is found that using sinusoidal approximation and generalized averaging, a dynamic phasor model can be obtained for the converter. Further analysis of the system leads to a two-timescale behaviour of the system which simplifies the controller design. The following chapter gives a design procedure along with simulation and experimental results.

Chapter 4

Three-port Series Resonant Converter - Design and Results

In this chapter the design of the three-port series resonant converter is discussed. The design procedure ensures soft-switching operation in all switches. Bi-directional power flow is possible in two of the three ports since the sources connected to port1 such as fuel cell, PV array are normally uni-directional. Simulation results along with experimental results from a laboratory prototype are presented.

4.1 Design requirements

The requirements on the region of operation for the three-port converter are:

1. To supply the load power independently from each of the sources.
2. Share the load between sources.
3. At reduced load, the main source is to supply the load and charge the battery.
4. When the load is regenerative, this power is used to charge the battery.

These requirements can be translated into power constraints (4.1)-(4.3). In these equations the maximum output power is considered as the base P_b. The maximum charging current for the battery used in the hardware prototype is limited and hence

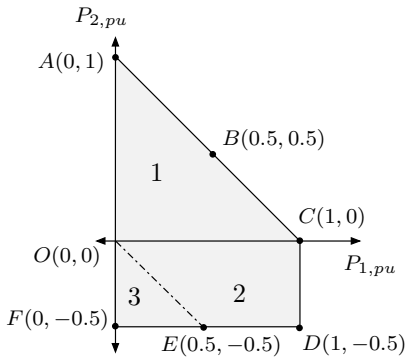

Figure 4.1: Operating region for the converter

the power $P_{2,pu}$ is limited to -0.5 p.u.

$$0 \leq P_{1,pu} \leq 1 \tag{4.1}$$

$$-0.5 \leq P_{2,pu} \leq 1 \tag{4.2}$$

$$\text{Since} \quad P_{1,pu} + P_{2,pu} = P_{o,pu}$$

$$-0.5 \leq P_{o,pu} \leq 1 \tag{4.3}$$

The power constraints are plotted in Fig. 4.1 with the x-axis as port1 power and y-axis as port2 power, both in per unit. The boundary is along the operating points O-A-B-C-D-E-F-O. In region1, power is shared between port1 and port2. In region2, port1 supplies load and port2. In region3, load is regenerative such as a motor-drive with regenerative braking. Along the line F-O, battery is charged from regenerative load. In the remaining points in region3, both the port1 and the regenerative load charge the battery. At the boundary between region2 and region3, the power supplied to the load is zero.

4.2 Design procedure

4.2.1 Prototype specifications

Some of the applications of a three-port converter are fuel-cell based automobiles and self sufficient residential and commercial buildings with fuel cells or PV array. In both

Table 4.1: Converter specifications

Specification	**Value**
Port1 voltage V_1	$50V$
Port2 voltage V_2	$36V$
Output power P_o	$0.5kW$
Output voltage V_o	$200V$

these applications energy storage using batteries is essential. A power level of 500W is chosen in this prototype design. At the end of this Chapter, a theoretical comparison is made with an existing three-port converter and a power level of $2.5kW$ is chosen to meet the typical peak power demand in a residential home. Fuel cells manufactured by companies such as Nuvera [35] give a regulated $48V$ output with power level between 2.5 to $50kW$. Port2 has batteries Lead Acid or NiMH with voltage level of $36V$. For example, voltage level of NiMH batteries used by a mild hybrid car [36] is around $36V$to$42V$. The output voltage to be maintained is chosen as $200V$ which is slightly above the rectified single phase ac voltage. The prototype specifications are summarized in Table 4.1.

4.2.2 Resonant converter parameters

At any given phase-shift angle and switching frequency, the quality factor which is load dependent, decides the voltage gain and peak currents. As an example, for a two-port converter as in Fig. 2.1, the voltage gain is given by (4.4) and the normalized peak current in the resonant tank is given by (4.5). For example, the normalized peak current not to exceed a value of 1.0, the lower limit on the quality factor is 8.5, calculated from (4.4) and (4.5) at maximum phase-shift angle $\theta = 90^o$. But the voltage gain at this Q is very low. In the prototype the quality factor is chosen as 4.0. The ratio of switching frequency to resonant frequency is chosen as 1.1 and switching frequency as $100kHz$. Higher quality factor also ensures the validity of sinusoidal approximation in the analysis.

$$\frac{V_o}{V_{in}} = \frac{1}{Q(F - \frac{1}{F})} \sin\theta \tag{4.4}$$

Table 4.2: Three-port converter parameters

Converter Parameter	**Value**
Resonant Inductor L_1	$28.4\mu H$
Resonant Capacitor C_1	$0.1\mu F$
Resonant Inductor L_2	$14.7\mu H$
Resonant Capacitor C_2	$0.22\mu F$
Turns ratio n_{13}	0.25
Turns ratio n_{23}	0.18

$$\hat{I}_{norm} = \frac{4}{\pi}\sqrt{1 + (\frac{V_o}{V_{in}})^2 - 2\frac{V_o}{V_{in}}\cos\theta} \tag{4.5}$$

To determine the voltage transfer ratios m_1 and m_2, an iterative procedure is adopted. For each value of m_1 and m_2, the phase-shifts along the boundary of the operating regions in Fig. 4.1 are calculated using (2.7), (2.15) and (2.16). The solution for the phase-shifts should exist and also lie between $-\pi/2$ and $\pi/2$. This iteration is performed using software Mathematica©. It is found that the values $m_1 = 1$ and $m_2 = 1$ satisfy the equations in all operating regions. It is also known from the steady state analysis that soft-switching operation is possible in all switches when $m_1 = 1$ and $m_2 = 1$. The resonant tank parameters are summarized in Table 4.2. With the load quality factor chosen as $Q = 4$, the maximum load power as $P_o = 500W$ and output voltage as $V_o = 200V$, the resonant tank inductance and capacitance are calculated from (2.6) and (2.8). The transformer turns ratio is calculated using (2.18).

The converter parameters as realized in hardware prototype are given in Table 4.2. Using the calculated values, as one traverses along the operating points boundary O-A-B-C-D-E-F-O, the corresponding phase-shifts are plotted in Fig. 4.2. Region3 phase-shifts are calculated using negative load currents.

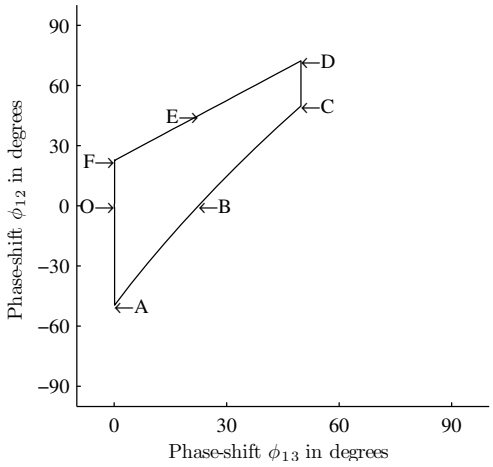

Figure 4.2: Calculated phase-shifts along the boundary of operating region

Table 4.3: Three-winding transformer prototype details

Parameter	**Value**
Transformer core area	$A_c = 113mm^2$
Primary side magnetizing inductance L_m	$70\mu H$
Primary side leakage inductance L_{lk1}	$0.6\mu H$
Secondary side leakage inductance L_{lk2}	$0.7\mu H$
Load side leakage inductance L_{lk3}	$2\mu H$
Turns ratio n_{13}	0.25
Turns ratio n_{23}	0.18

4.2.3 Transformer design

The three-winding transformer uses ferrite core designed for a maximum flux density of $0.3T$. The transformer is designed using the area product method [37]. The transformer parameters are measured using the method explained in [38, 11]. The values of the leakage inductances and the magnetizing inductances are summarized in Table 4.3. The magnetizing inductance measured in the transformer prototype is $L_m = 70\mu H$ resulting in $Q_m = 10.8$ which is 14 times greater than $Q_1\left(F_1 - \frac{1}{F_1}\right)$ for $Q_1 = 4$ and $F_1 = 1.1$. The magnitude of the leakage inductance is $L_{lk3} = 2\mu H$ with $Q_{lk3} = 0.019$ whose value is 40 times lesser than $Q_1\left(F_1 - \frac{1}{F_1}\right)$. Including the effect of leakage inductance L_{lk3},

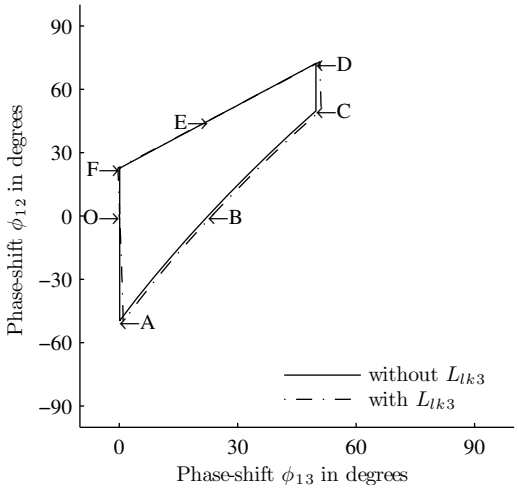

Figure 4.3: Calculated phase-shifts along the boundary of operating region with and without the effect of leakage inductance

the phase shifts are calculated and plotted in Fig. 4.3. It is observed that the change in phase shifts is not significant.

In the design, it is assumed that the source connected to port1 is unidirectional and hence $\phi_{13} > 0$. But, bi-directional power flow can be enabled in this port also, if constraint of $\phi_{13} > 0$ is removed. The soft-switching operation conditions given in (2.19), (2.21) and (2.23) are always satisfied in this design since $m_1 = m_2 = 1$ and the output voltage is regulated to 1 pu. The maximum value of peak normalized tank current for port1 for the entire operating region is found to be 1.1, equivalent to 17.8A, occurring at the boundary C-D. Similarly for port2, the peak normalized tank current is 1.1, equivalent to 25A at operating point A.

4.3 Simulation results

Simulation results of the converter in Saber© for operating points B, C, D and F are given in this section. Effect of leakage inductance is also discussed. Controller design is explained and results from closed loop simulation in Matlab are given.

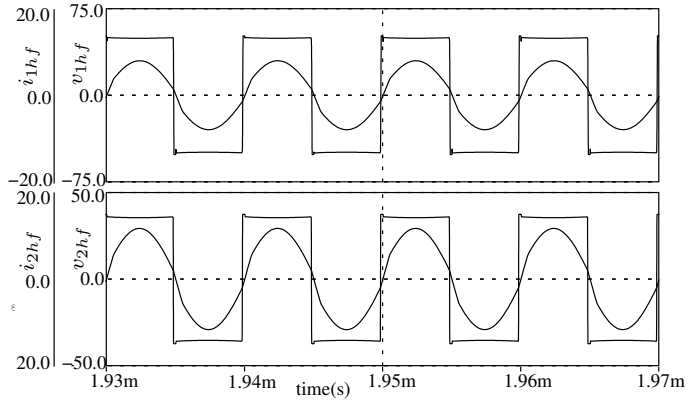

Figure 4.4: Simulation results of applied port1 voltages v_{1hf}, v_{2hf} (square waves) and tank currents i_{1hf}, i_{2hf} around operating point B

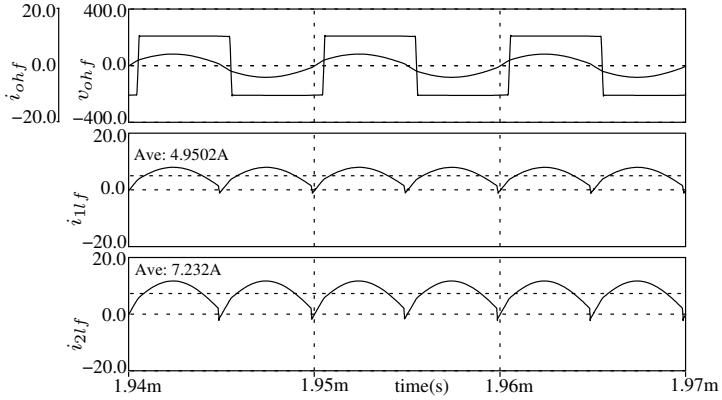

Figure 4.5: Simulation results of port3 voltage v_{ohf}, winding3 current i_{ohf}, port1 and port2 unfiltered input currents around operating point B

4.3.1 Simulations results at different operating points

Simulation results of port1 applied resonant tank voltage (square wave) along with the tank current is shown in Fig. 4.4 for operation around point B in Fig. 4.1. Soft-switching operation is possible when the tank current lags the applied voltage. For port1 and port2 this is true as seen from Fig. 4.4, although the magnitude of current available for soft-switching operation is $< 1A$. The simulation is done in open loop with the phase-shift angles selected using Fig. 4.2. The load-side transformer winding3 voltage v_{ohf} is shown in Fig. 4.5 along with the winding3 current i_{ohf} which leads the

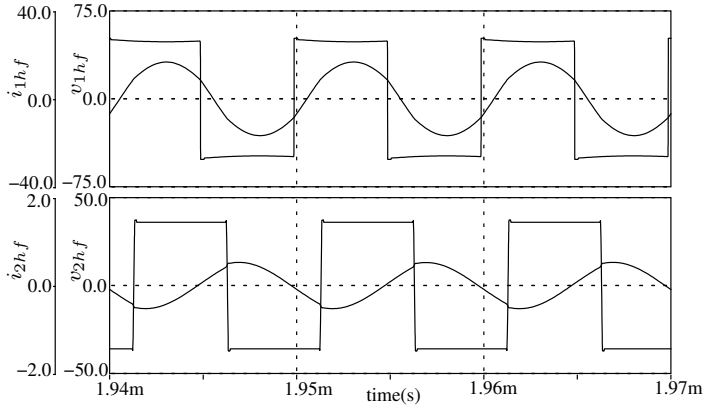

Figure 4.6: Simulation results of applied port1 voltages v_{1hf}, v_{2hf} (square waves) and tank currents i_{1hf}, i_{2hf} around operating point C

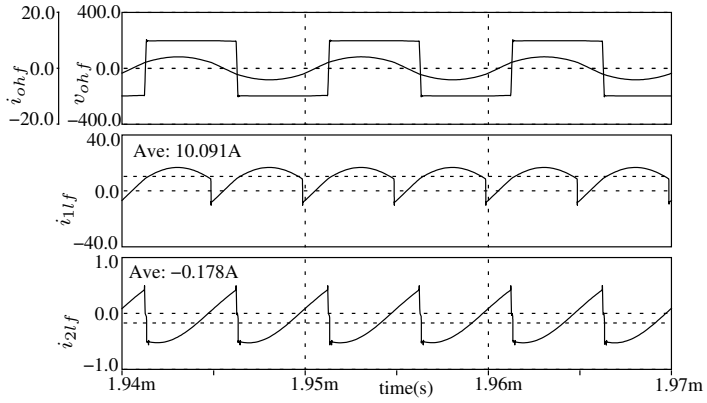

Figure 4.7: Simulation results of port3 voltage v_{ohf}, winding3 current i_{ohf}, port1 and port2 unfiltered input currents around operating point C

voltage. It is known from analysis that this is the condition for soft-switching operation in port3 which is more critical from switching loss point of view due to the high voltage, $200V$ in this converter. The waveform v_{ohf} switches between $\pm 200V$ indicating the output voltage as $200V$. The unfiltered port1 and port2 input currents are also shown in Fig. 4.5 to indicate the equal power sharing between the ports for a $500W$ load.

At operating point C in Fig. 4.1, the port2 supplies zero power and the entire load power is supplied by port1. The simulation results at this operating point is shown in Fig. 4.6 and Fig. 4.7. It can be observed that the port2 unfiltered current has an average

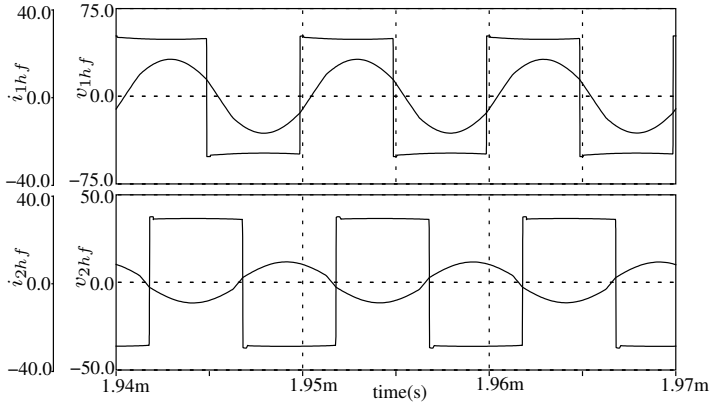

Figure 4.8: Simulation results of applied port1 voltages v_{1hf}, v_{2hf} (square waves) and tank currents i_{1hf}, i_{2hf} around operating point D

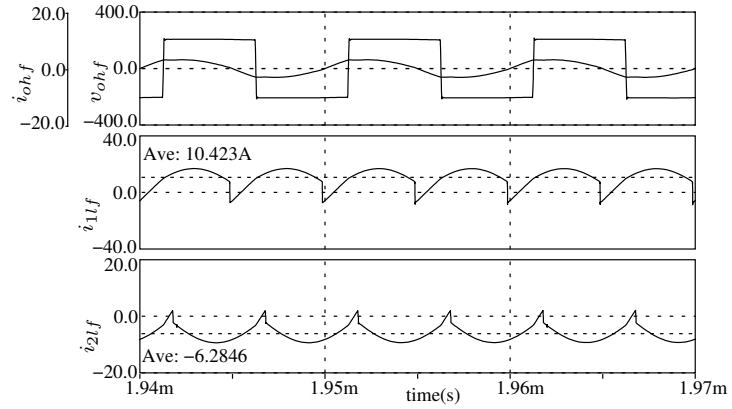

Figure 4.9: Simulation results of port3 voltage v_{ohf}, winding3 current i_{ohf}, port1 and port2 unfiltered input currents around operating point D

value almost equal to zero. The tank2 current peak reduces at this operating point which can also be seen from the analysis graph in Fig. 2.7. Soft-switching operating condition is satisfied in port1 and port3 as observed from Fig. 4.6. The output voltage has a magnitude of $200V$ as observed from v_{ohf} in Fig. 4.7.

At operating point D in Fig. 4.1, the port2 power is negative i.e., the load is reduced by half and the port1 extra power is used to charge the battery. Results at this operating point are shown in Fig. 4.8 and Fig. 4.9. From these figures, it can be concluded that ZVS occurs in port1 and port2 due to the lagging nature of the tank currents. ZVS occurs in port3 since the winding3 current i_{ohf} leads the winding3 voltage v_{ohf}. The

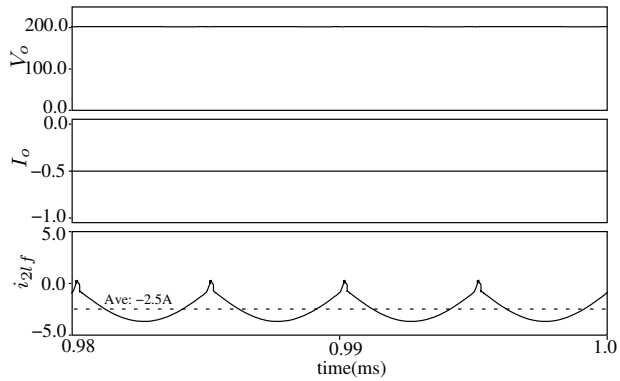

Figure 4.10: Simulated port2 unfiltered input current i_{2lf} for operation in region3

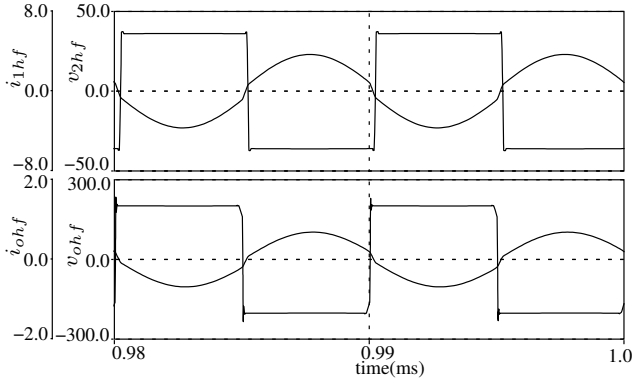

Figure 4.11: Port2 and Port3 high frequency current for regenerative load operation

output voltage is $200V$ as observed from v_{ohf} in Fig. 4.9.

Operation in region3 takes place when the load is regenerative. This is modeled as a current source of magnitude $-I_o$ at the load-end. The reference for port1 current $I_{1(ref)}$ is set at zero. This operating point is along the line F-O. Simulation result of the port2 unfiltered current i_{2lf} is shown in Fig 4.10, for a load current of $-0.5A$. The port2 applied high frequency voltage along with the tank current are shown in Fig. 4.11 proving ZVS operation. Soft-switching operation occurs in port3 also, as seen from the current direction during transitions in Fig. 4.11. The simulation results presented so far prove that the proposed three-port converter can operate in all regions shown in Fig. 4.1.

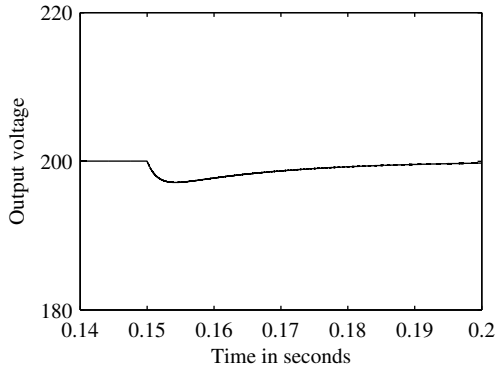

Figure 4.12: Output voltage response with PI controller for a step increase in load from $400W$ to $500W$

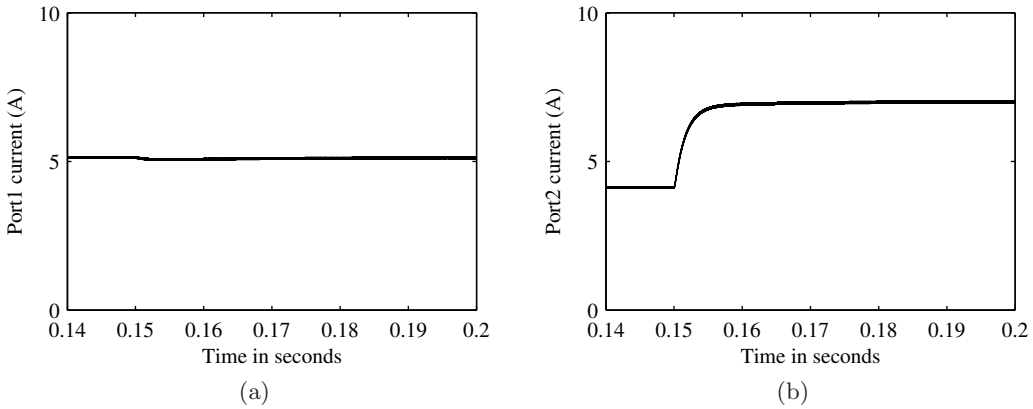

Figure 4.13: Port current response with PI controller for a step increase in load from $400W$ to $500W$ (a) Port1 (b) Port2

4.3.2 Closed loop controller simulation

The dynamic analysis, presented in Chapter 3, resulted in a simplified block diagram shown in Fig. 3.2. The PI controller is designed in such a way that the zero introduced by the controller equals the load side filter time constant RC_o, the pole of the reduced system. The value of R is chosen to be the full load value to take care of the worst case operating condition. The gain is adjusted to give a bandwidth of $100Hz$. The state equations (3.1-3.5) are realized in Simulink and the closed loop simulation is performed for a step increase in load from $400W$ to $500W$. The output voltage response for

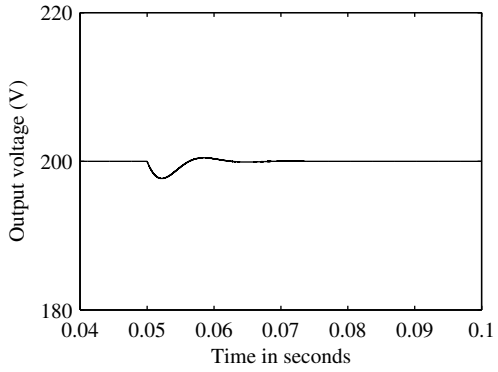

Figure 4.14: Output voltage response with nonlinear controller for a step increase in load from $400W$ to $500W$

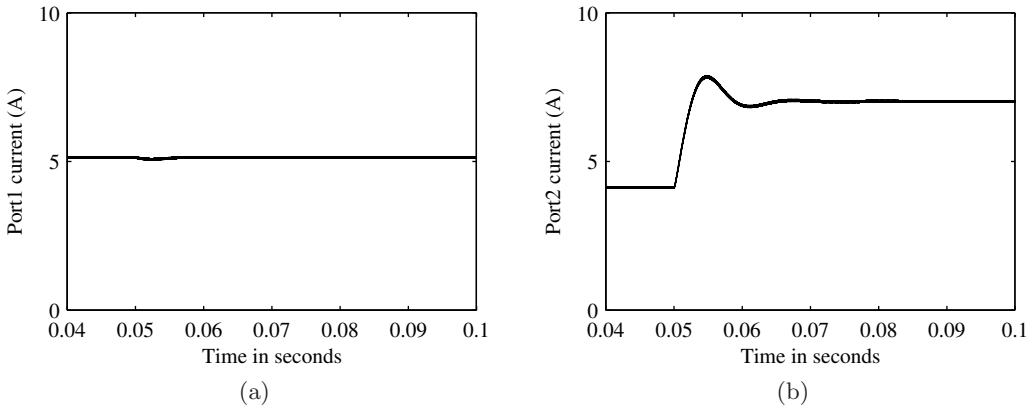

Figure 4.15: Port current response with nonlinear controller for a step increase in load from $400W$ to $500W$ (a) Port1 (b) Port2

a step increase in load is shown in Fig. 4.12. It can be observed that the settling time is around $30ms$ which satisfies the required bandwidth condition. The response of port1 and port2 currents are shown in Fig. 4.13a and Fig. 4.13b. It can be seen that port1 current continues to be maintained at the constant value of $I_{1ref} = 5A$ and port2 or the battery current increases to cater to the step load increase. Since port1 current I_1 is not regulated in closed loop, a steady-state error is introduced between the reference I_{1ref} and the actual current. But the control restricts sudden transients in the current. The steady-state error in port1 current I_1 may be contributed by sinusoidal approximation, parameter variations and conduction losses. This error can be removed

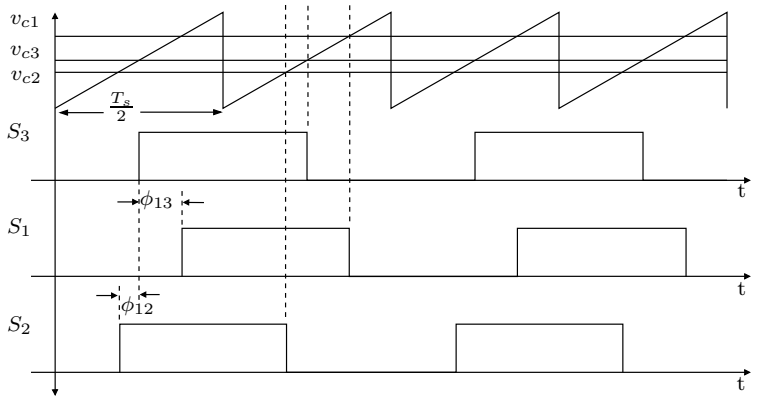

Figure 4.16: Carrier signal and control voltages for generating the PWM pulses for the three-port converter

by adding another slow control loop to regulate the port1 current.

A non-linear controller is designed as explained in Section 3.5 to compare the response with the PI controller. In the equations, R is unknown and it is estimated in the control loop. The results of the $100W$ step increase in load are given in Fig. 4.14 and Fig. 4.15. The values of g and k are chosen to have the dominant pole at $2\pi 100$ rad/s.

4.4 Experimental results

4.4.1 Laboratory setup

A $500W$ prototype is realized in hardware with the controller implemented in Digilent Basys© FPGA board [39]. The pulses for the Mosfets are generated using a ramp carrier signal and two control voltages for the two phase-shifts as shown in Fig. 4.16. The pulse generation module is also implemented in FPGA. Since all the pulses are at 50%, pulse transformers are used for isolation in gate-drive. The converter parameters are given in Table 4.2. The battery port has three $12V, 12Ah$ lead acid batteries connected in series. Port1 uses a dc source with magnitude $50V$, to emulate a renewable energy source. The output voltage is sensed using an LEM sensor whose output is connected to an ADC module with the FPGA. The converter operates in closed loop with output voltage regulated at $200V$. The closed loop controller design is explained in the previous section. The hardware setup for testing is shown in Fig. 4.17.

Figure 4.17: Hardware setup for testing the series resonant three-port converter

4.4.2 Prototype results

Results of applied tank voltage and tank currents for port1 and port2 are shown in Fig. 4.18 and Fig. 4.19, for operation around point B in Fig. 4.1, where the load is equally shared between port1 and port2. It is observed from these figures that the tank currents lag their applied voltages and hence ZVS occurs in all switches of port1 and port2. In Fig. 4.19, the magnitude of current during the switching transition is $1A$, which is sufficient for lossless transition.

The load-side high frequency port voltage v_{ohf} which switches between $\pm 200V$ along with the current in winding3 of the transformer is shown in Fig 4.20. The current leads the voltage, which is the condition for ZVS in port3 based on the current direction mentioned in Chapter 2. The phase-shift ϕ_{12} between the port1 and port2 applied voltages is zero as observed in Fig. 4.21 and also from analysis in Fig. 4.2.

At operating point C in Fig. 4.1, the power supplied by port2 to the load is zero. The results of port2 voltage and current around this operating point is shown in Fig. 4.22. The magnitude of current is $< 1A$ and port2 supplies $< 5\%$ of the load. From Fig. 4.23, it can be observed that the output voltage is $200V$, since the square wave magnitude theoretically equals the output voltage minus the voltage drop in the switches. ZVS occurs in all switches in the converter for this operating point also, as evident from the applied tank voltages and currents in port1 (Fig. 4.24) and port2 (Fig. 4.25).

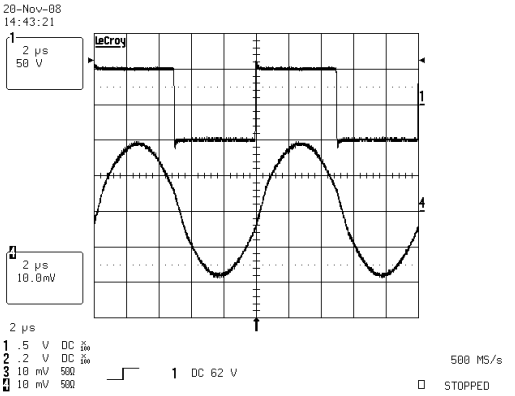

Figure 4.18: Applied port1 voltage v_{1hf} (50V/div) and tank current i_{1hf} (5A/div) around operating point B

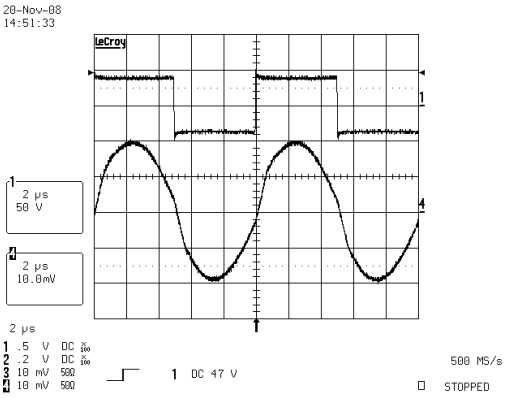

Figure 4.19: Applied port2 voltage v_{2hf} (50V/div) and tank current i_{2hf} (5A/div) around operating point B

The port2 power is negative along the line C-D in Fig 4.1. This operating point can be reached by keeping the port1 current reference $I_{1(ref)}$ same as the point C and reducing the load. The port2 or battery current is negative in Fig. 4.26 and its average value is $-2.0A$. The phase-shift ϕ_{12} between port1 and port2 applied voltage in Fig. 4.27 is 55^o. The port2 tank current current is shown in Fig. 4.28 where it is observed that during the switching transition $-V_2$ to V_2, the current is negative resulting in ZVS. From Fig. 4.29, it can be observed that the power output is reduced because of the reduction in the current magnitude when compared with Fig. 4.23. Also output voltage is regulated to $200V$ and port3 switches perform ZVS. The average of the efficiency for

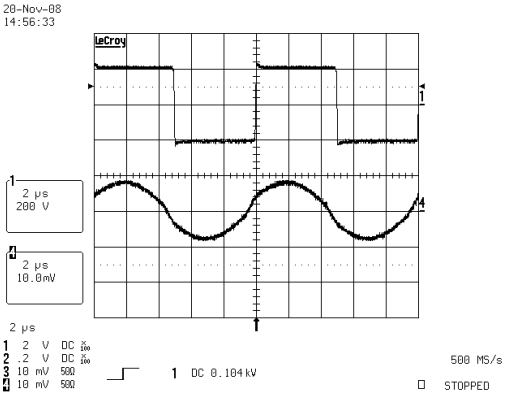

Figure 4.20: Transformer winding3 voltage v_{ohf} (200V/div) and current i_{ohf} (5A/div) around operating point B

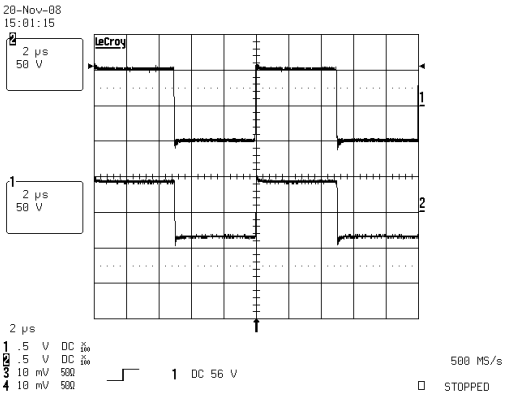

Figure 4.21: Applied port1 voltage v_{1hf} (50V/div) and applied port2 voltage v_{2hf} (50V/div) showing zero phase-shift around operating point B

the three operating points is 91%.

Operation in region3 takes place when the load is regenerative. This is modeled as a current source of magnitude $-I_o$ at the load-end. The reference for port1 current $I_{1(ref)}$ is set at zero. This operating point is along the line F-O. Simulation results for this operating point are given in the previous section.

The response of the converter for a step-load increase from $400W$ to $500W$ is shown in Fig. 4.30. It is observed that the port1 current I_1 maintains its value of $6A$ and the port2 battery current I_2 increases to supply the extra power to the load. This is useful when a slow dynamic response fuel-cell is connected to port1. The output voltage

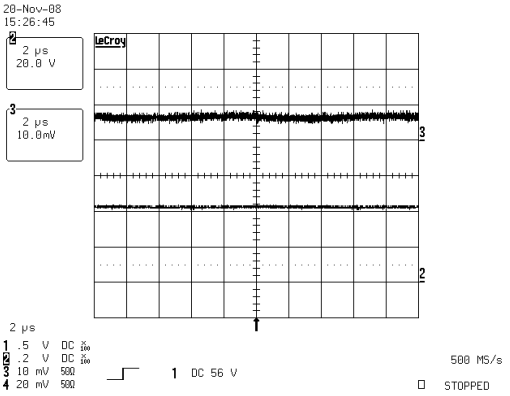

Figure 4.22: Port2 dc voltage V_2 (50V/div) and dc current I_2 (2A/div) around operating point C

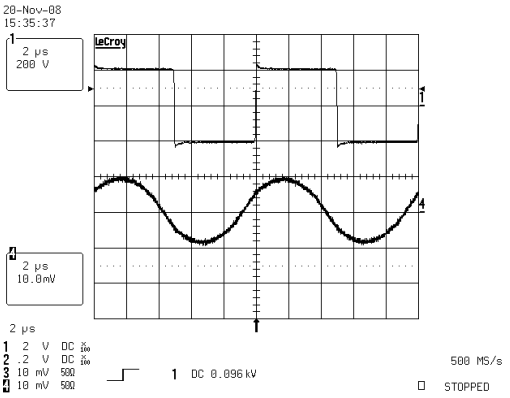

Figure 4.23: Transformer winding3 voltage v_{ohf} (200V/div) and current i_{ohf} (5A/div) around operating point C

settles back to its original value after $30ms$ as seen from the response. The designed bandwidth is low due to hardware implementation constraints.

4.5 Comparison with existing three-port converter

The proposed series resonant based triple active bridge (TABSRC) three-port dc-dc converter Fig. 2.2 is compared with a triple active bridge converter (TAB) with inductors only Fig. 1.4. A $2.5kW$ power converter is designed using both types of converter circuits. A power level of $2.5kW$ is chosen to meet the typical peak power demand in a

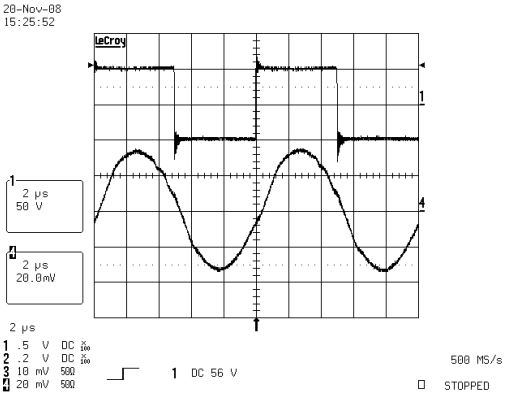

Figure 4.24: Applied port1 voltage v_{1hf} (50V/div) and tank current i_{1hf} (5A/div) around operating point C

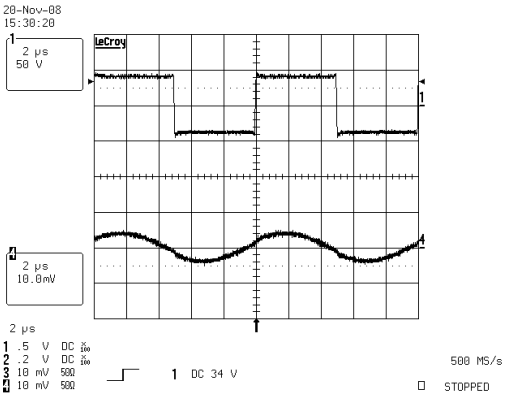

Figure 4.25: Applied port2 voltage v_{2hf} (50V/div) and tank current i_{2hf} (5A/div) around operating point C

residential home and using commercially available Nuvera Fuel Cell [35] and NiMH or lead acid batteries. The specifications for comparison is summarized in Table 4.4. The two converters are compared based on transformer size, component stress and softswitching. A theoretical comparison is presented to indicate the advantages of TABSRC over TAB. Sinusoidal approximation is used for both the converters for ease of comparison and equation simplifications.The transformer winding3 leakage inductance is assumed to be low to minimize the power flow between ports.

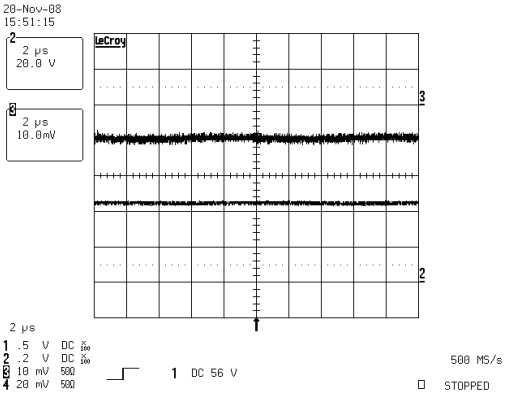

Figure 4.26: Port2 dc voltage V_2 (50V/div) and dc current I_2 (2A/div) around operating point D

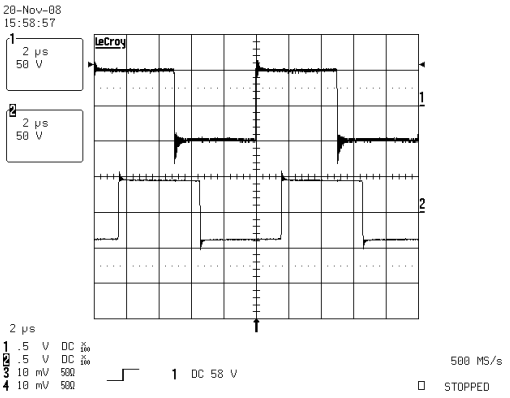

Figure 4.27: Applied port1 voltage v_{1hf} (50V/div) and applied port2 voltage v_{2hf} (50V/div) showing phase-shift around operating point D

4.5.1 Comparison at constant switching frequency

In this comparison, the switching frequency is held constant at $100kHz$. The ratio of switching frequency to resonant frequency in the series resonant converter is chosen as 1.1. The output current for both the converters under sinusoidal approximation is given in (4.6) and (4.7). Note that the only change is in the value of the impedance offered by the resonant tank circuit versus inductance alone.

$$I_o = \frac{8}{\pi^2}\frac{n_{13}V_1}{Z_1(F_1 - \frac{1}{F_1})}\sin\phi_{13} + \frac{8}{\pi^2}\frac{n_{23}V_2}{Z_2(F_2 - \frac{1}{F_2})}\sin\left(\phi_{13} - \phi_{12}\right) \quad (TABSRC) \quad (4.6)$$

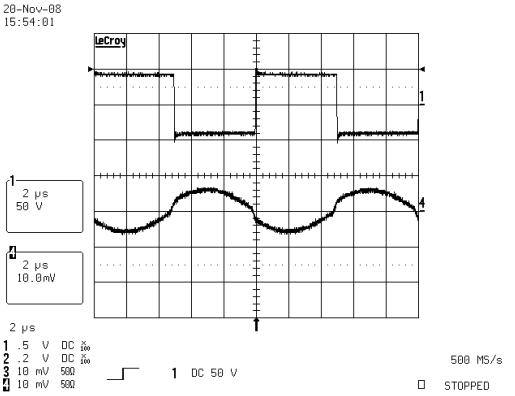

Figure 4.28: Applied port2 voltage v_{2hf} (50V/div) and tank current i_{2hf} (5A/div) around operating point D

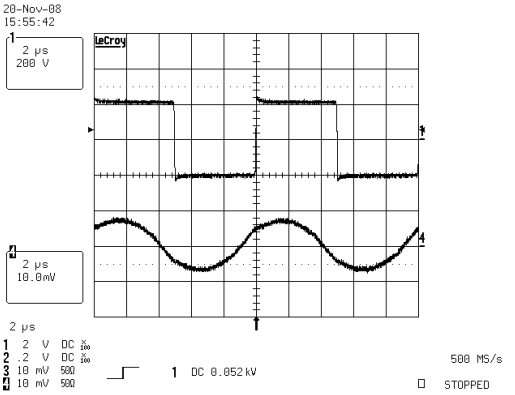

Figure 4.29: Transformer winding3 voltage v_{ohf} (200V/div) and current i_{ohf} (5A/div) around operating point D

$$I_o = \frac{8}{\pi^2}\frac{n_{13}V_1}{w_s L_1}\sin\phi_{13} + \frac{8}{\pi^2}\frac{n_{23}V_2}{w_s L_2}\sin\left(\phi_{13}-\phi_{12}\right) \quad (TAB) \tag{4.7}$$

The voltage ratios m_1 and m_2 are chosen in such a way that the inductors in both the circuits are easily realizable i.e, equal to or more than the leakage inductance of the transformer. The design method is explained in Section 4.2.2. The results of the calculations done in Mathematica© are given in Table 4.5.

The boundary O-A-B-C-D-E-F in Fig. 4.1 is traversed for both the converters and the corresponding phase shifts are determined theoretically. With the value of the phase shifts, the rms currents through all three windings are found out. Note that the

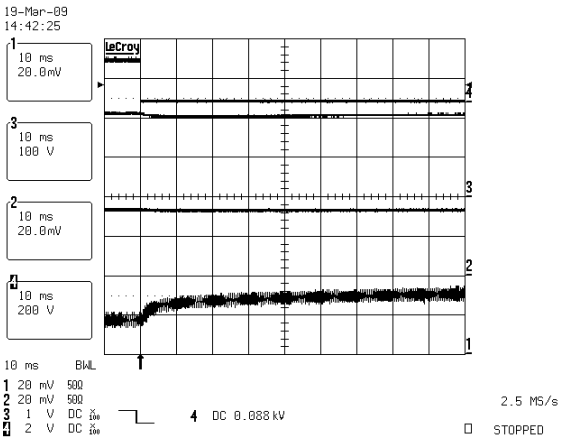

Figure 4.30: Dynamic response of the converter for a step-load increase from $400W$ to $500W$ Ch.1 Battery current (4A/div), Ch.2 Port1 current (4A/div) Ch.3 Output voltage (100V/div) and Ch.4 Trigger input

Table 4.4: Converter specifications for comparison between TAB and TABSRC

Specification	**Value**
Port1 voltage V_1	$48V$
Port2 voltage V_2	$36V$
Output power P_o	$2.5kW$
Output voltage V_o	$200V$

normalized peak or rms current remains the same for both the converters. But the factor used for normalization, which is the applied voltage divided by the impedance offered by the tank or inductor alone, is different. Hence (2.24) and (2.25) are used in calculating the normalized port1 and port2 high frequency currents. The rms current of port3 is found out both by simulation and solving (2.4). The maximum of these values calculated using Matlab are given in Table 4.6 for both the converters.

The transformer size is proportional to the Area Product. This is obtained from the rms voltages, rms currents and the switching frequency, with core material selected as Ferrite and the results are given in Table 4.6. The inductances are low enough to be realized using the three-winding transformer and hence comparison of size for the inductors is not given. Besides the rms currents through port1 and port2 side windings are almost same.

Table 4.5: Converter parameters for TAB, TABSRC at constant switching frequency

Converter Parameter	**TAB**	**TABSRC**
Resonant Inductor1 L_1	$3.3\mu H$	$6.5\mu H$
Resonant Inductor2 L_2	$1.4\mu H$	$3.3\mu H$
Resonant Capacitor1 C_1	NA	$0.47\mu F$
Resonant Capacitor2 C_2	NA	$0.94\mu F$
Turns ratio n_{13}	0.8	0.27
Turns ratio n_{23}	0.5	0.19
Voltage ratio $d_1 = \frac{V_1}{n_{13}V_o}$	0.3	0.9
Voltage ratio $d_2 = \frac{V_2}{n_{23}V_o}$	0.35	0.95
Switching Frequency f_s	$100kHz$	$100kHz$

Table 4.6: Comparison of TAB and TABSRC based on rms currents and transformer size at the same switching frequency

Converter Parameter	**TAB**	**TABSRC**
Maximum rms current through winding 1 I_{L_1}	$60.5A$	$63.7A$
Maximum rms current through winding 2 I_{L_2}	$83.7A$	$78.8A$
Maximum rms current through winding 3 I_{L_3}	$60.0A$	$17.9A$
Maximum load current I_0	$12.5A$	$12.5A$
Area Product	$42.06cm^4$	$13.84cm^4$

From Table 4.6, it is clear that there is 3 times increase in transformer size for TAB when compared to TABSRC. Also the rms current through winding3 minus the load current directly gives the size of the filter capacitor required at the output. From Table 4.6, it is clear that there is more than 4 times increase in output filter size. Soft switching region for both the converters remain same and hence lowered switching losses for both the converters.

Table 4.7: Converter parameters for TAB, TABSRC for constant voltage ratios

Converter Parameter	**TAB**	**TABSRC**
Resonant Inductor1 L_1	$4.4\mu H$	$6.5\mu H$
Resonant Inductor2 L_2	$2.22\mu H$	$3.3\mu H$
Resonant Capacitor1 C_1	NA	$0.47\mu F$
Resonant Capacitor2 C_2	NA	$0.94\mu F$
Turns ratio n_{13}	0.27	0.27
Turns ratio n_{23}	0.19	0.19
Voltage ratio m_1	0.9	0.9
Voltage ratio m_2	0.95	0.95
Switching Frequency f_s	$25kHz$	$100kHz$

4.5.2 Comparison at constant voltage ratios

The difference between the previous comparison and this comparison is that the voltage ratios m_1 and m_2 are kept constant in this case. Hence to achieve realizable inductor values the switching frequency had to be reduced to $25kHz$. A similar procedure as explained in previous section is followed to determine the parameters. They are summarized in Table 4.8 with the determined values given in Table 4.7.

From Table 4.8, it is clear that there is 4 times increase in transformer size for TAB when compared to TABSRC due to reduction in switching frequency. Also the rms current through winding 3 is the same for both TAB and TABSRC, hence the ripple rms current rating in the output filter capacitor remains same. But since the switching frequency reduces 4 times, the size of the filter increases 4 times. Soft switching region for both the converters remain same and hence lowered switching losses for both the converters.

4.5.3 Comparison based on magnetizing inductance

During transients, it is possible that the inductor current in TAB will have an average value which can saturate the transformer. To prevent transformer saturation, an air gap is introduced in the transformer [10]. This decreases the magnetizing inductance and also complicates the equivalent circuit as explained in Section 2.5. Whereas in

Table 4.8: Comparison of TAB and TABSRC based on rms currents and transformer size at the same voltage ratio

Converter Parameter	**TAB**	**TABSRC**
Maximum rms current through winding 1 I_{L_1}	$62.7A$	$63.7A$
Maximum rms current through winding 2 I_{L_2}	$83.9A$	$78.8A$
Maximum rms current through winding 3 I_{L_3}	$17.7A$	$17.9A$
Maximum load current I_0	$12.5A$	$12.5A$
Area Product	$55.6cm^4$	$13.84cm^4$

TABSRC, the resonant capacitor blocks dc and prevents saturation. Hence high value of magnetizing inductance is possible, increasing Q_m. This inherent advantage of TABSRC effectively simplifies transformer realization.

4.5.4 Comparison conclusion

In this section the TAB and the proposed TABSRC converters are compared at constant switching frequency and at constant voltage ratios. It is observed that at constant switching frequency, the transformer size of TABSRC is $1/3^{rd}$ of TAB. Also the output side filter capacitor's ripple rms current rating of TABSRC is $1/4^{th}$ of TABSRC. At constant voltage ratios, the switching frequency need to be reduced to get realizable value of inductors. At the reduced switching frequency, the transformer size of TABSRC is $1/4^{th}$ of TAB. Also the output filter capacitor size of TAB increases 4 times due to reduction in switching frequency. Hence it is advantageous to use the proposed TABSRC at higher switching frequencies and higher power output.

4.6 Conclusion

In this section, a design procedure for the proposed three-port series resonant converter is explained. It can be seen from the results that the design ensures soft-switching and bi-directional power flow operation. Simulation and experimental results confirm the analysis results. The advantages of the proposed converter over existing topologies is explained using a sample design.

Chapter 5

Three-port Series Resonant Converter - Load-side Diode Bridge

The active bridge in the proposed three-port series resonant converter can be replaced by a diode bridge for uni-directional load applications. This is useful in reducing the switching losses in the load-side converter especially at loads less than 50% of the maximum load and at very high output voltages. It also reduces the drive circuitry necessary for the load-side active bridge if application does not demand regenerative load capability. Load-side diode bridge is more economical in such applications. In this Chapter, phase-shift modulation (PSM) control techniques are proposed for the three-port series resonant converter with load-side diode bridge. Analysis, simulation and experimental results are presented.

5.1 Proposed topology and modulation schemes

The series resonant three-port converter with load-side diode bridge is shown in Fig. 5.1. Port1 can be a Fuel cell or any constant dc power source and port2 is shown as Battery. L_1 and C_1 form the resonant tank circuit for port1 and L_2 and C_2 for port2. Capacitors C_{f1} and C_{f2} form the filter capacitors at the input of each of the ports. The

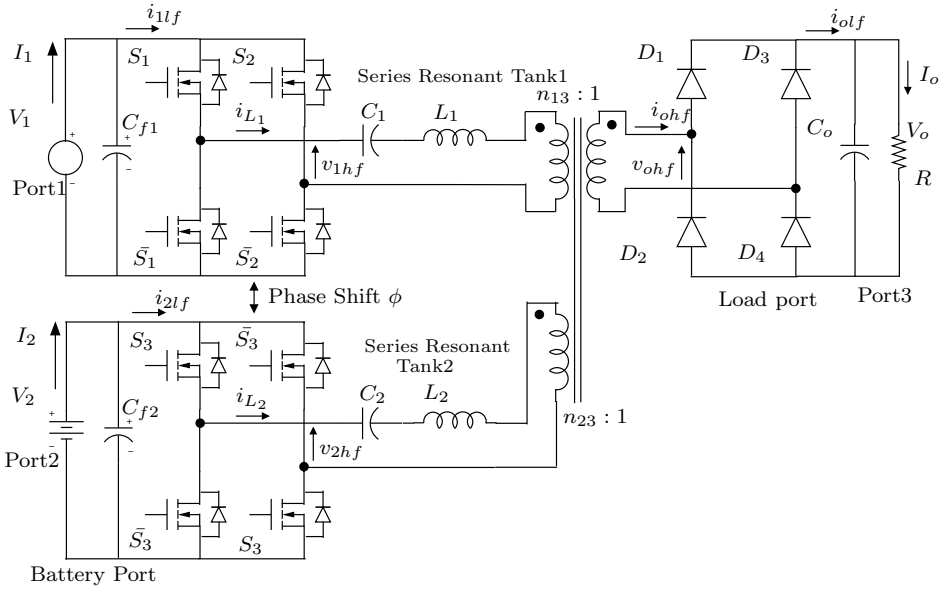

Figure 5.1: Proposed three-port series-resonant converter circuit with load-side diode bridge

transformer shown is a three-winding transformer whose third winding is connected to diode bridge and output capacitor. The converter operates at constant switching frequency F_s above resonant frequency of both the resonant tanks.

Due to the absence of an active bridge at the load-side, the phase-shift ϕ_{13} described in Chapter 2 cannot be used. Rather this phase-shift is now fixed by the diode bridge and not controllable. The control variables are defined using bridge voltage waveforms in Fig. 5.2. The phase-shift angle ϕ controls the phase angle between the fundamental of v_{1hf} and v_{2hf}. It is negative when v_{2hf} lags v_{1hf}. The phase shift angle θ controls the magnitude of the fundamental of v_{1hf}. Note that the port1 PWM uses center modulation to have independent variation of θ and ϕ. In other words, if θ varies, only the magnitude of the fundamental of v_{1hf} varies and not the phase-shift between v_{1hf} and v_{2hf}. Center modulation [40] achieves this by varying the phase-shift of right leg and left leg of the active bridge opposite to each other from a constant reference. The switches in each leg are complimentary.

In the following section, an analysis using sinusoidal approximation is presented and the expressions of port power and output voltage as a function of θ and ϕ are derived.

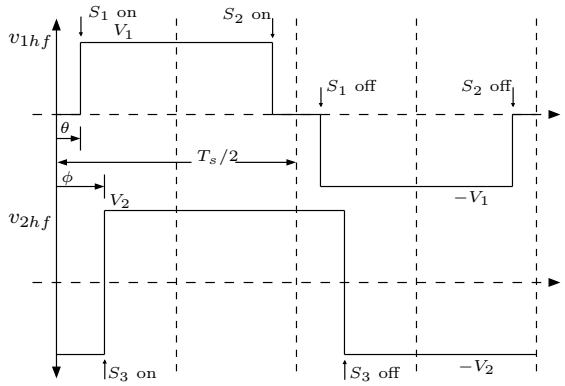

Figure 5.2: Bridge voltage waveforms v_{1hf}, v_{2hf} showing definitions of θ and ϕ

In Section 5.3 design of the three-port resonant converter is explained. In Section 5.4 and 5.5, simulation and experimental results are presented.

5.2 Steady-state analysis

5.2.1 Equivalent circuit

The steady state analysis is performed using sinusoidal approximation [7,41,37] i.e., the resonant circuit filters all the higher harmonic voltages and the tank current is essentially sinusoidal. This approximation does lead to an error of around 5% in steady state values. An exact analysis of the circuit without this approximation is complicated due to the presence of two resonant tanks and two control variables. But when operated in closed loop the controller compensates for the minimal error introduced by sinusoidal analysis. In Section 5.4 output voltage using sinusoidal approximation and exact simulation model is calculated for an operating point and compared. The derivation of equivalent circuit and conversion ratio extends the methodology given in [41] for a three-port series resonant converter.

The ac equivalent circuit for the resonant tank is shown in Fig. 5.3. The load can be reflected as an ac resistance R_{ac} since the voltage v_{ohf} and current i_{ohf} are in phase because of the diode bridge [41]. The transfer function $V_{t3}(s)$ as a function of $V_{1hf}(s)$ and $V_{2hf}(s)$ is given by (5.1). The variables are converted to capital letters to indicate transfer function. The turns ratio of the transformer is changed from the earlier

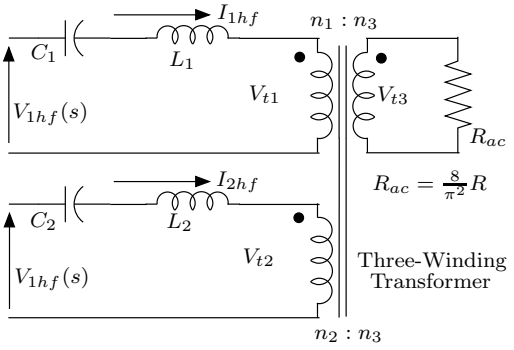

Figure 5.3: AC equivalent circuit of the resonant tank network for analysis

converter to distinguish the final steady-state expressions.

$$V_{t3}(s) = H_1(s)\frac{n_3}{n_1}V_{1hf}(s) + H_2(s)\frac{n_3}{n_2}V_{2hf}(s) \tag{5.1}$$

The quality factor and the ratio of switching frequency F_s to the resonant frequency are defined in (5.2). ω_1 and ω_2 are the resonant frequencies in rad/s for resonant tank 1 and 2 respectively.

$$F_i = \frac{\omega_s}{\omega_i};\quad \omega_s = 2\pi F_s;\quad \omega_i = \frac{1}{\sqrt{L_i C_i}};\quad Q_i = \frac{\sqrt{\frac{L_i}{C_i}}}{\frac{8}{\pi^2}R_{ac}\left(\frac{n_i^2}{n_3^2}\right)};\quad i = 1, 2 \tag{5.2}$$

5.2.2 Steady-state equations

The gain of the transfer functions $H_1(s)$ and $H_2(s)$ is evaluated at switching frequency (5.3).

$$\|H_i(j\omega_s)\| = \left[\left(F_i - \frac{1}{F_i}\right)^2 Q_i^2 + \left(1 + \frac{Q_i F_j\left(1 - F_i^2\right)}{Q_j F_i\left(1 - F_j^2\right)}\right)^2\right]^{-0.5} \tag{5.3}$$
$$\text{where } i = 1, 2;\ j = 1, 2;\ i \neq j$$

The phase shift angle θ changes the magnitude of the fundamental component of v_{1hf} co-sinusoidally as determined from Fourier series. The phase shift angle ϕ, which is the phase difference between the two fundamental sinusoidal components v_{1hf} and

v_{2hf}, changes the phase angle of the resultant sine voltage in the second part of (5.1). In a two port series resonant converter the magnitude of transfer function at switching frequency directly gives the voltage gain of the converter. The analysis here is done in a similar way but the effects of both θ and ϕ have to be included since the currents i_{1hf} and i_{2hf} are not in phase. After some algebra, the dc output voltage V_o as a function of input dc voltages V_1 and V_2 is derived and shown in (5.4).

$$\begin{aligned} V_o = \Big[&\left(V_1 \frac{n_3}{n_1} H_{1m} \cos\theta\right)^2 + \left(V_2 \frac{n_3}{n_2} H_{2m}\right)^2 \\ &+ 2V_1 \frac{n_3}{n_1} H_{1m} V_2 \frac{n_3}{n_2} H_{2m} \cos\theta \cos\phi \Big]^{0.5} \\ \text{where } H_{im} &= \|H_i(j\omega_s)\|; \quad i = 1, 2 \end{aligned} \tag{5.4}$$

The expressions can be converted to per unit representation for ease of calculations, design and comparison. Let the base voltage be defined as V_b and the base power as P_b. In design, the values of these are chosen as the required output voltage and the required output power. The voltage conversion ratios are defined in (5.5).

$$m_i = \frac{V_i \left(\frac{n_3}{n_i}\right)}{V_b}; \quad i = 1, 2 \tag{5.5}$$

The expression of the output voltage (5.4) can then be converted to per unit as given in (5.6).

$$V_{o,pu} = \sqrt{(m_1 H_{1m} \cos\theta)^2 + (m_2 H_{2m})^2 + 2m_1 H_{1m} m_2 H_{2m} \cos\theta \cos\phi} \tag{5.6}$$

The current transfer functions $I_{1hf}(s)$ and $I_{2hf}(s)$ from Fig. 5.3 can be written as a function of $V_{1hf}(s)$ and $V_{2hf}(s)$ in a form similar to (5.1). Transferring to the dc side using the magnitude and phase of the corresponding transfer functions expressions, the per unit power from port1 $P_{1,pu}$ and port2 $P_{2,pu}$ are derived and given in (5.7) and (5.8) where $P_{o,pu}$ is the output power in per unit.

$$\begin{aligned} P_{1,pu} = \Big[&I_{12m} m_1 m_2 \cos(I_{12ph} + \phi) \\ &+ I_{11m} m_1^2 \cos\theta \cos(I_{11ph}) \Big] \cos\theta \ P_{o,pu} \end{aligned} \tag{5.7}$$

$$\begin{aligned} P_{2,pu} = \Big[&I_{21m} m_1 m_2 \cos\theta \cos(I_{21ph} - \phi) \\ &+ I_{22m} m_2^2 \cos(I_{22ph}) \Big] \cos\theta \ P_{o,pu} \end{aligned} \tag{5.8}$$

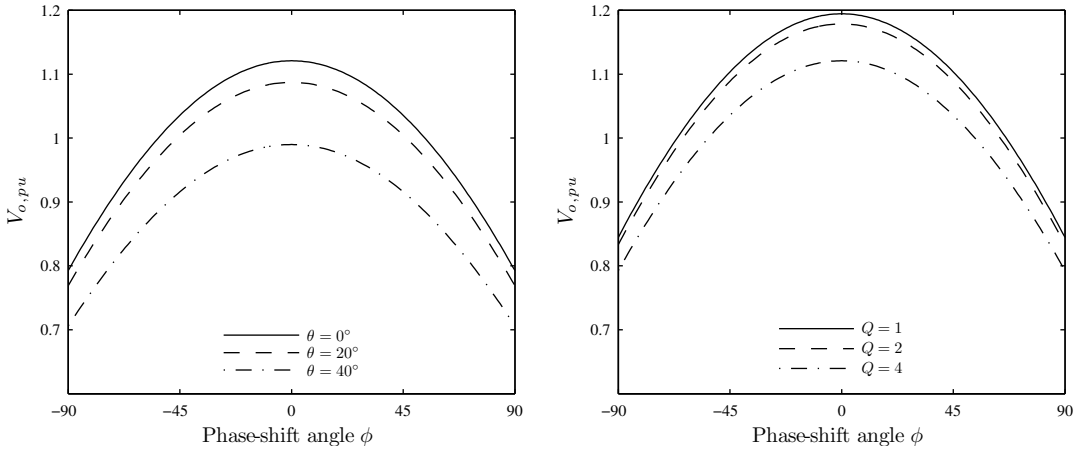

Figure 5.4: Output voltage in pu Vs phase shift angle ϕ for different values of (a) Phase shift angle θ (b) Load quality factor Q

$$I_{ijm} = \|I_{ij}(j\omega_s)\|;\ I_{ijph} = \angle I_{ij}(j\omega_s);\ i,j = 1,2 \tag{5.9}$$

5.2.3 Plots of output voltage and port power

At constant switching frequency, the transfer functions magnitude and phase depend on the load only and not on the phase shift angles θ and ϕ. A plot of the output voltage in per unit $V_{o,pu}$ as a function of ϕ for various values of θ is given in Fig. 5.4a. In this plot the values of F_1 and F_2 are kept constant at 1.1, Q_1 and Q_2 kept constant at 4.0 under full load and m_1 and m_2 kept constant at 1.2. In the actual design Q_1 and Q_2 and F_1 and F_2 are made approximately equal, but m_1 and m_2 can take on different values based on voltage levels at the ports. It is also to be noted that when compared to the converter proposed in Chapter 2, the values of m_1, m_2 have to be higher. From the plot it is seen that the output voltage can be kept constant at $1pu$ by varying the phase-shift angles. A plot of the output voltage as a function of ϕ for various values of load quality factor under constant θ is given in Fig. 5.4b. The load quality factor is kept approximately the same for both the ports as per design. It is observed from Fig. 5.4b that variation of output voltage with load is not significant due to the effect of two

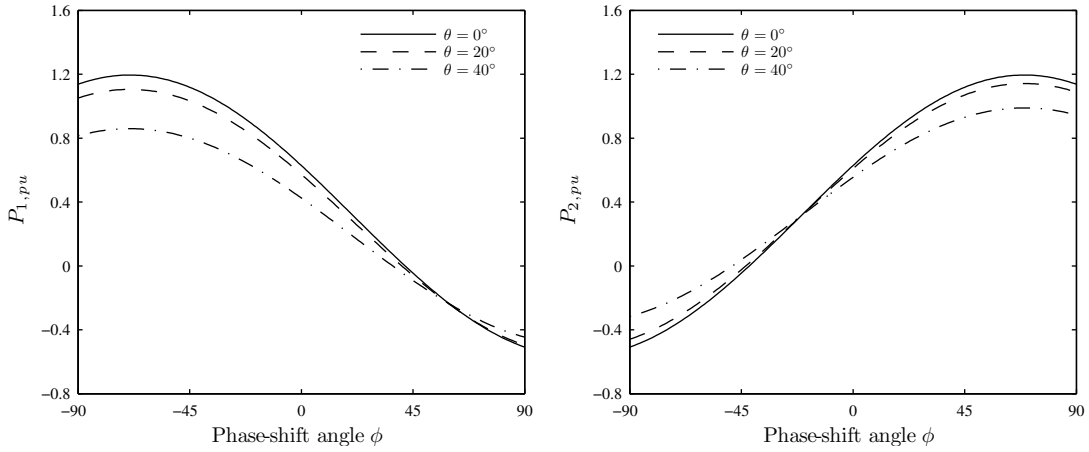

Figure 5.5: Port power plot Vs phase shift angle ϕ (a) Port1 $P_{1,pu}$ (b) Port2 $P_{2,pu}$

resonant circuits.

A plot of per unit power for both the ports as a function of ϕ for various values of θ is given in Fig. 5.5a & 5.5b. It is observed from Fig. 5.5b that port2 power goes negative for negative values of ϕ. Hence a battery can be charged during this region of operation. The power delivered to the load $P_{o,pu}$ can be calculated from Fig. 5.4a by squaring each point since the quantities are in per unit. Hence from Figs. 5.4a, 5.5a & 5.5b it can be seen that the power from input ports is equal to the power through the load port.

It is known that the voltage gain for a two-port series resonant converter with load-side active bridge is more than the load-side diode bridge. This is due to the fact that the phase-shift angle between the input-side and load-side active bridge can reach a maximum angle of 90^o. The same is true for a three-port converter. A plot of per unit output voltage using (5.6) and (2.14) is shown in Fig. 5.6a and 5.6b respectively. In the plot, the values of m_1 and m_2 are chosen as 1.0, Q_1 and Q_2 as 4.0 and F_1 and F_2 as 1.1. It is observed that the maximum possible output voltage for the load-side active bridge is 2.8 times the output voltage for the load-side diode bridge. Also the output voltage has a wider range in Fig. 5.6b due to the additional control variable ϕ_{13}.

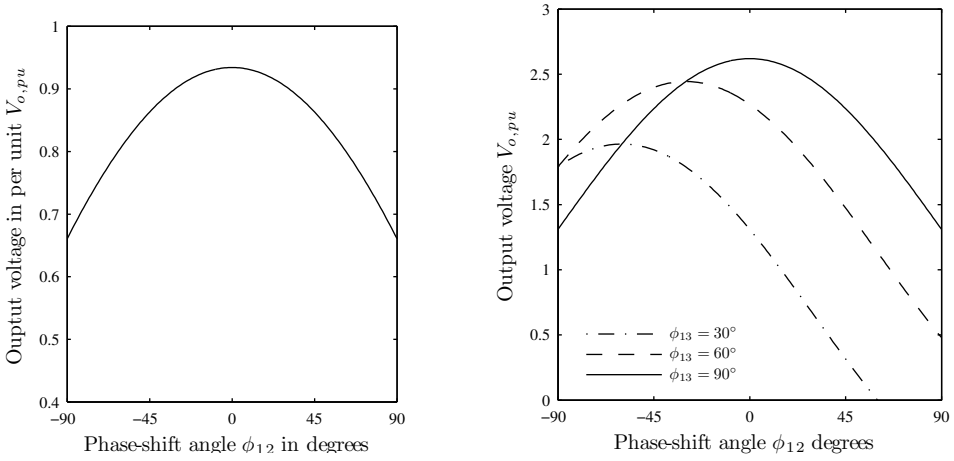

Figure 5.6: Output voltage in per unit Vs phase-shift angle ϕ_{12} for different values of ϕ_{13} (a) Load-side diode bridge (5.6) (b) Load-side active bridge (2.14)

5.2.4 Peak tank currents

The peak of the normalized tank currents $i_{1hf(pk)}$ and $i_{2hf(pk)}$ can be calculated using sinusoidal analysis and is presented in Fig. 5.7a & 5.7b. The normalization is done with respect to the corresponding port voltage and characteristic impedance. The peak of the tank currents increase as the operating point moves away from equal load sharing. The peak currents in series resonant based three port converter are lower due to the sinusoidal nature of currents when compared to dual active bridge based three-port converter. But the peak currents with diode bridge at the load side is more than the peak currents observed with active bridge at the load side as can be seen from Figs. 5.7b and 2.7.

5.2.5 Soft-switching operation

Zero Voltage Switching (ZVS) is possible in a series-resonant circuit when operated above resonant frequency [37, 41]. The region of ZVS is analyzed in this three-port converter. The magnitude of tank current at the instant of switching in each bridge is calculated. When the current is negative before turn-on of any switch, the anti-parallel diode across the switch conducts and hence the switch turns on at zero voltage. In the

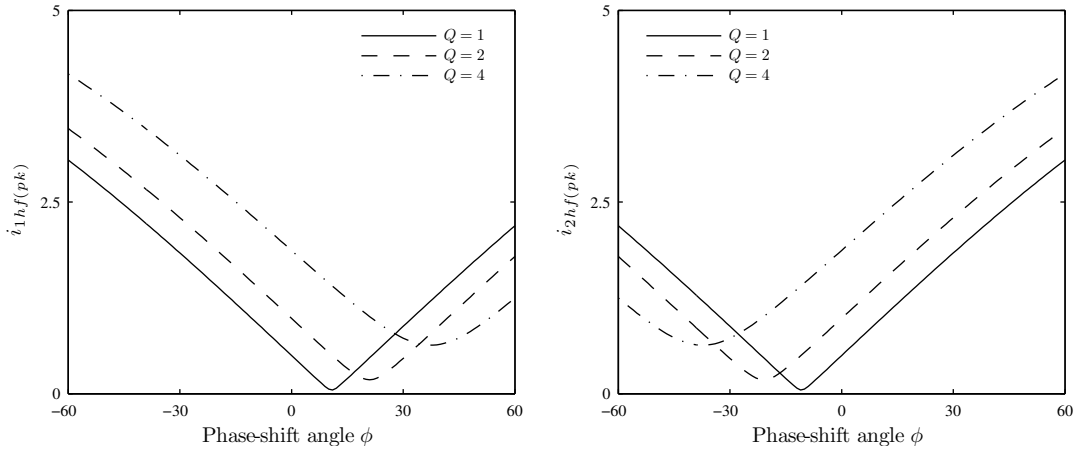

Figure 5.7: Normalized peak tank currents for (a) Port1 $i_{1hf(pk)}$ (b) Port2 $i_{2hf(pk)}$

following plots m_1 and m_2 are kept constant at 1.2 , the phase shift angle $\theta = 20^\circ$ and the currents are normalized. A plot of the magnitude of current at the instant of turnon of switch S_1 in port1 bridge is shown in Fig. 5.8a. S_1 loses ZVS as the load increases and also as the phase shift ϕ lags further. Due to phase modulation in the port1 bridge, ZVS for both the legs in the entire range of operation is not achieved. Whereas in Fig. 5.8b the current before switch S_3 turnon is always negative enabling ZVS for the entire range of operation of varying load and power distribution between sources.

There is an alternate method of arriving at the steady-state equations for the three-port series resonant converter with load-side diode bridge. This method also assumes sinusoidal tank currents and voltages. It can be derived from the results presented for the three-port series resonant converter with load-side active bridge. The angle ϕ_{13} is now determined by the load side bridge. In other words, the waveforms of v_{ohf} and i_{ohf} in Fig. 2.3 are now in phase because of the diode bridge. Hence in (2.3), the load current can now be obtained by equating ϕ_{13} with θ_3. The value of θ_3 is solved using (2.4). This method is simpler with two ports but the algebra is complicated with three ports in solving θ_3. Hence the transfer function based approach is used with an equivalent ac resistance across the load-side winding of the transformer.

The effect of leakage inductance of the three-winding transformer can be similarly

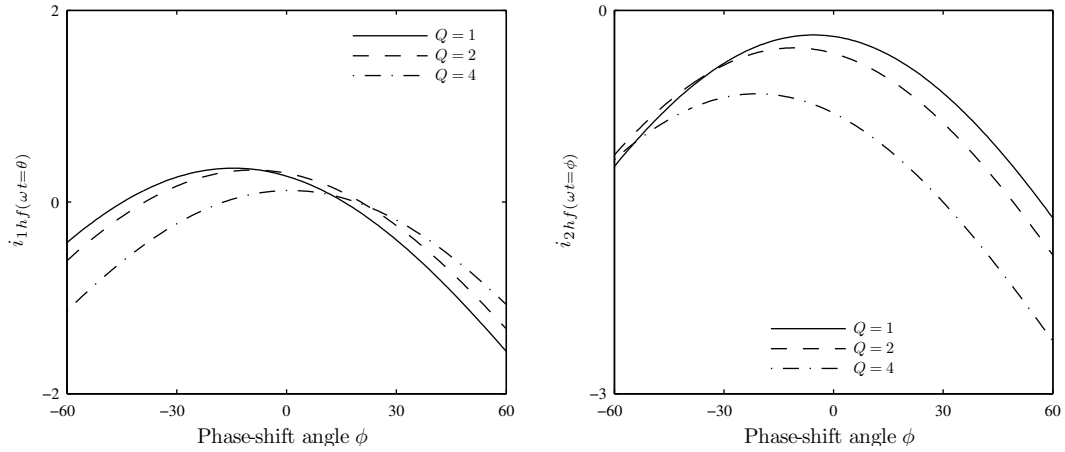

Figure 5.8: Normalized current at turn-on of switch indicating ZVS region (a) Switch S_1 (b) Switch S_3

analyzed as in Section 2.5. But it has been proved in Section 2.5 that if the quality factors are chosen high, the effect of leakage inductance in winding3 of the transformer can be neglected. This assumption is extended in this topology also, so that the equations are simplified. The following section gives a detailed design procedure for the proposed converter.

5.3 Design Procedure

In the previous section steady state analysis of the converter was explained and in this section a method for design of three-port series resonant converter with load-side diode bridge is discussed. The region of operation for the converter is shown in Fig. 5.9 as a function of both the input port power in per unit. The constraints that were used to draw the graph are given in (5.10). As the operating point moves from B to C, the load decreases. Battery charging occurs at reduced load so that the extra power available from port1 is utilized effectively. The maximum power during battery charging given in (5.10) is lower than the power output to the load and in this design it is chosen to be 0.36 *pu*. It depends on the battery used for the converter. Note the difference in the

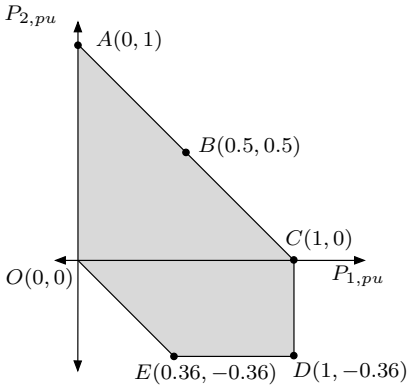

Figure 5.9: Operating region of series resonant three-port converter with load-side diode bridge

operating regions of Fig. 4.1 and Fig. 5.9.

$$\begin{aligned} 0 \leq P_{1,pu} + P_{2,pu} &\leq 1 \\ -0.36 \leq P_{2,pu} &\leq 1 \\ 0 \leq P_{1,pu} &\leq 1 \end{aligned} \tag{5.10}$$

The parameters m_1 and m_2 are selected such that the converter is able to operate at points A and D shown in Fig. 5.9 for a chosen value of quality factor. In other words there must exist finite values of θ and ϕ such that the output voltage is maintained at 1 pu and satisfy points A and D in the graph. This is found out by numerically evaluating (5.6), (5.7) and (5.8). From known values of input voltages V_1 and V_2 the turns ratio can be selected using (5.5). Given the switching frequency F_s and the ratio of switching frequency to resonant frequency which in this case chosen as 1.1, the series resonant parameters are calculated using (5.2). As the design satisfies at extreme operating points A and D, it is found that the converter can operate at any point inside and the boundary of the region in Fig. 5.9 by varying θ and ϕ. As the operating point moves from A to D along the boundary, the port 2 side bridge does ZVS as explained in Section 5.2.

Using the design procedure mentioned above, the values of the converter parameters are chosen with the calculation done in Mathematica©. The results of the design of a $500W$ converter using this procedure is summarized in Table 5.1. The values of m_1 and m_2 are found to be 1.2 and 1.4 respectively.

Table 5.1: Designed component values of a $P_o = 500W$ output three-port series resonant converter with load-side diode bridge

Parameter	Value	Units
L_1	15.0	μH
L_2	7.1	μH
C_1	0.22	μF
C_2	0.47	μF
C_o	220	μF
V_1	50	V
V_2	36	V
$n_1 : n_3$	0.208:1	
$n_2 : n_3$	0.125:1	

5.4 Simulation results

5.4.1 Simulation method

Simulation of the three-port series resonant converter is performed in Saber© with input voltages chosen as $V_1 = 50V$ and $V_2 = 36V$ which is equivalent to three $12V$ batteries connected in series. The output voltage V_o is kept around $200V$ by adjusting the phase shifts. Simulation is performed in open loop. The converter switches at $F_s = 100kHz$ which is 1.1 times above the resonant frequency of both the resonant tanks.

Simulation is also performed in Matlab using an exact model of the converter (5.11-5.15). Using the exact model, the series resonant tank parameters such as the peak tank currents and voltages which are needed to design the tank inductor and capacitor are calculated. Other parameters such as the transformer VA rating, switch currents, input and output filter design are also estimated in simulation. The analysis presented in the previous section uses sinusoidal approximation. A comparison of results obtained through sinusoidal approximation and the exact model are also presented.

$$L_1\dot{i}_{L_1} = \frac{V_1}{2}\left(\text{sgn}(\sin(\omega_s t - \theta) + \text{sgn}(\sin(\omega_s t + \theta))\right) - v_{C_1} - \frac{n_1}{n_3} v_o \ \text{sgn}\left(\frac{n_1}{n_3} i_{L_1} + \frac{n_2}{n_3} i_{L_2}\right) \tag{5.11}$$

$$C_1\dot{v}_{C_1} = i_{L_1} \tag{5.12}$$

$$L_2\dot{i}_{L_2} = V_2 \ \text{sgn}(\sin(\omega_s t + \phi)) - v_{C_2}$$

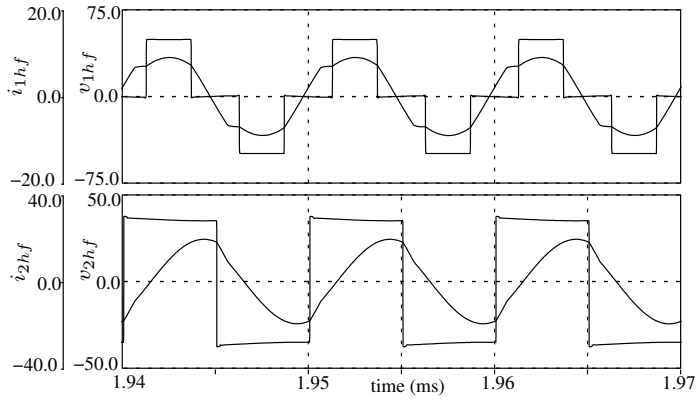

Figure 5.10: Simulated port1, port2 bridge voltages v_{1hf}, v_{2hf} & resonant tank currents i_{1hf}, i_{2hf} for a power sharing ratio of 1 : 1

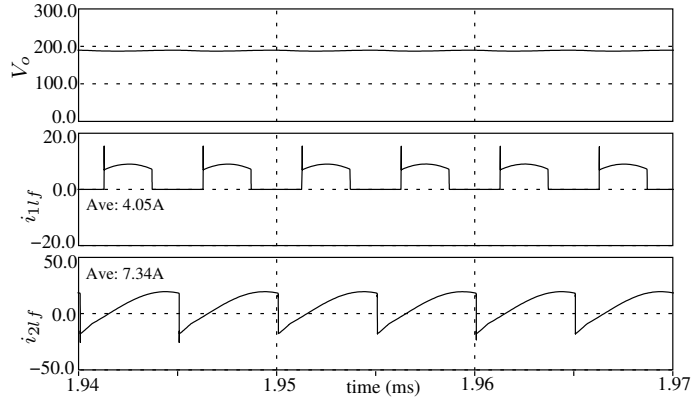

Figure 5.11: Simulated port1 and port2 input currents i_{1lf}, i_{2lf} along with the output voltage V_o for operating point B

$$- \frac{n_2}{n_3} v_o \operatorname{sgn}\left(\frac{n_1}{n_3} i_{L_1} + \frac{n_2}{n_3} i_{L_2}\right) \tag{5.13}$$

$$C_2 \dot{v}_{C_2} = i_{L_2} \tag{5.14}$$

$$C_o \dot{v}_o = \left|\frac{n_1}{n_3} i_{L_1} + \frac{n_2}{n_3} i_{L_2}\right| - \frac{v_o}{R} \tag{5.15}$$

5.4.2 Simulation results at different operating points

The simulated waveforms of port1 bridge voltage and resonant tank current and port2 bridge voltage and resonant tank current for a power sharing ratio of 1 : 1 are shown in

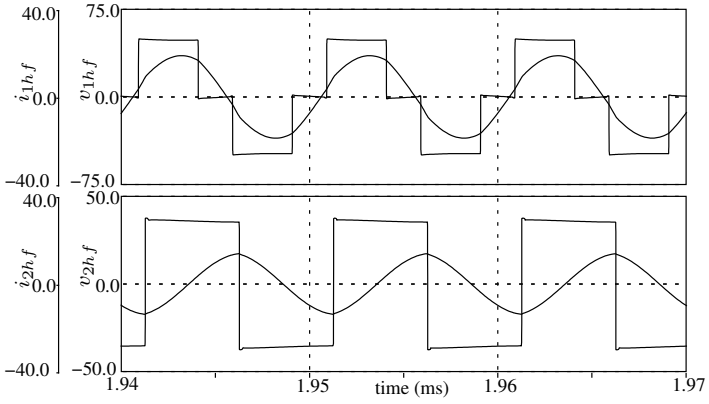

Figure 5.12: Simulated port1, port2 bridge voltages v_{1hf}, v_{2hf} & resonant tank currents i_{1hf}, i_{2hf} for operating point C

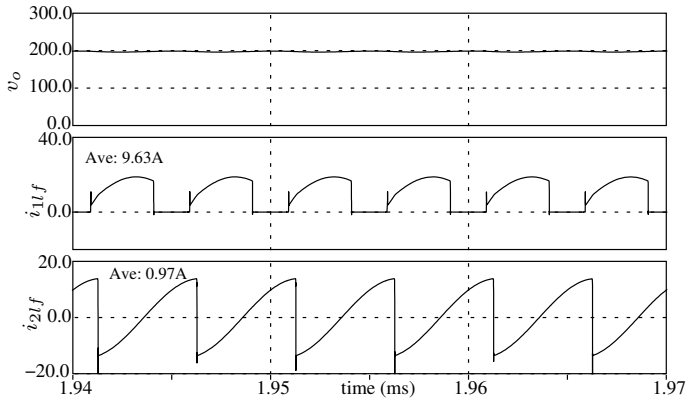

Figure 5.13: Simulated port1 and port2 input currents i_{1lf}, i_{2lf} along with the output voltage V_o for operating point C

Fig. 5.10. This is for operating point B in Fig. 5.9. It is seen from Fig. 5.10 that switch S_1 does hard switching since current at turnon of switch is positive and switch S_2 does ZVS. The unfiltered port1 and port2 currents are shown in Fig. 5.11. The tank current waveforms are not purely sinusoidal and hence an error occurs between calculated and simulated values. For this operating point B, the calculated value of output voltage using sinusoidal approximation is $200V$ and the actual simulated value is $188V$ leading to an error of around 5%. The voltage drops are also due to the Mosfet conduction losses since the simulation uses IRF540Z which has finite on-state resistance.

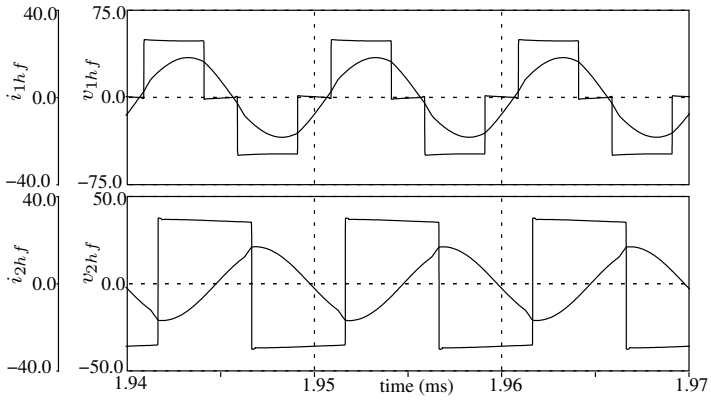

Figure 5.14: Simulated port1, port2 bridge voltages v_{1hf}, v_{2hf} & resonant tank currents i_{1hf}, i_{2hf} for operating point D

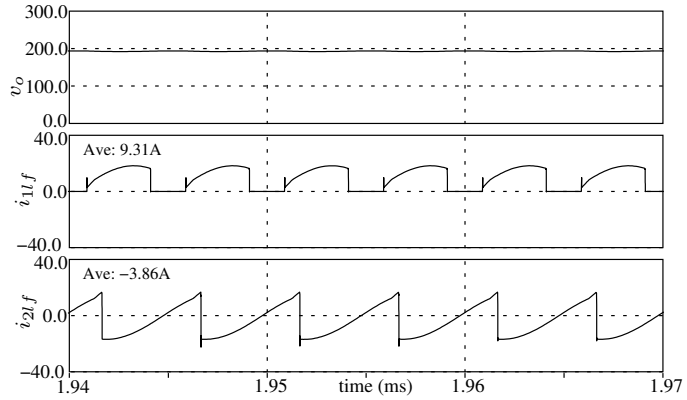

Figure 5.15: Simulated port1 and port2 input currents i_{1lf}, i_{2lf} along with the output voltage V_o for operating point D

The simulated waveforms for operating point C are shown in Figs. 5.12 and 5.13. At this operating point the full power of the load is supplied by port1 and the battery current is almost zero. To achieve this, the phase shift between the port1 and port2 has to go negative, so that the power flow in port2 starts reversing. The phase-shift angle ϕ can be observed from Fig. 5.12. Soft-switching operation is ensured in port2 but the left leg switches in port1 lose ZVS due to phase-modulation. The output voltage is around $200V$ as shown in Fig. 5.13. Although the average current in port2 is low, the ripple in the current is high which requires the use of filter capacitors at the input. This is true for port1 and the load-side port.

Table 5.2: Comparison of outputs calculated using sinusoidal approximation model (SM) and exact model (EM)

Parameter	A		C		D	
	SM	EM	SM	EM	SM	EM
$V_o(V)$	200	197	200	187.9	200	191.6
$P_1(W)$	500	483.5	0	-13.5	500	476
$P_2(W)$	0	1.5	500	455.4	-180	-181.8
$P_o(W)$	500	485.1	500	441.5	320	293.7

For operating point D in Fig. 5.9 the tank currents are shown in Fig. 5.14 and Fig. 5.15. The average value of the unfiltered port2 input current I_2 shown in Fig. 5.15 is negative and hence the battery is charging during this mode of operation. Filter capacitors are required to filter the ripple in these currents since port currents need to be dc. Input current in port1 is not negative due to phase modulation in port1 bridge. For this operating point, ZVS occurs in all switches in port2 bridge. The phase lag $\phi = -61.5^\circ$ between the bridge voltages v_{1hf} and v_{2hf} can be observed from Fig. 5.12. The output voltage is still maintained around $200V$ and the load is reduced.

5.4.3 Component specifications

The model given in (5.11-5.15) can be solved using ode45 or any other differential equation solver with nested function loop structure in Matlab environment. The equations can also be solved using predefined blocks in Simulink. Both methods are used in calculating the component parameters such as rms currents, peak voltages, rms ripple currents, conduction losses and soft-switching operating conditions. In this section, calculations of these component parameters using the model (5.11-5.15) is presented. Since analytical solutions are complicated, simulation is used. The values of the components used in the converter are given in Table 5.1. It is to be noted that analytical solutions were easy to obtain for the three-port series resonant converter proposed in Chapter 2 due to the absence of the absolute function in (3.5) when compared to (5.15).

Sinusoidal approximation introduces an error between the calculated and the observed values. For the three operating points A, C and D, the phase-shifts ϕ, θ are calculated using the equations presented in the analysis Section 5.2. These phase-shift

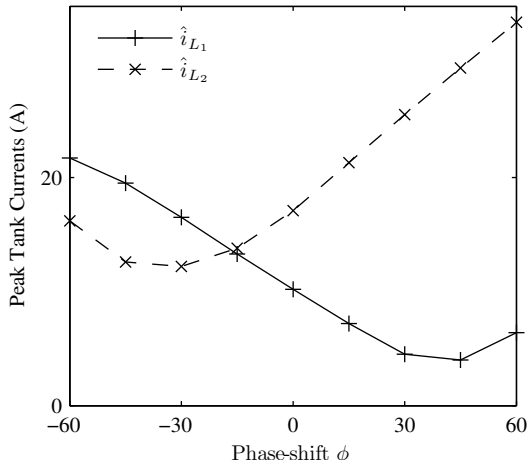

Figure 5.16: Simulation results of peak resonant tank currents $\hat{i}_{L_1}$ and $\hat{i}_{L_2}$ at various phase shift angles ϕ

values are then substituted in the exact model (EM) (5.11-5.15) and simulated in Matlab. The results of the observed output voltage along with port power are given in Table 5.2. It can be observed that the error does not exceed 5%.

The peak current and rms current through the inductor are required to design the magnetics. Peak current determines the maximum flux in the core material and the rms current determines the area of cross-section of the copper conductor used in the winding. Simulation is performed by varying the phase shift ϕ with constant $\theta = 15^o$ at full load. The peak currents $\hat{i}_{L_1}$, $\hat{i}_{L_2}$ for resonant tank 1 and 2 respectively are plotted for several values of ϕ in Fig. 5.16. The rms currents $i_{L_1(rms)}$ and $i_{L_2(rms)}$ can also be calculated using the same procedure. For the operating points A, B, C, D in Fig. 5.9, the results for the peak and rms currents along with other component specifications are summarized in Table 5.4. From the graph and the table the maximum peak current for which the core is to be selected should be at least $19A$ for tank1 and $30A$ for tank2. An increase in $\hat{i}_{L_2}$ in Fig. 5.16 at negative phase shifts is due to battery charging.

To choose the resonant capacitor given its value, the maximum voltage rating and the rms current through the capacitor are required. The rms current along with the equivalent series resistance of the capacitor determines the temperature rise and voltage drop in the capacitor. The rms currents are already calculated for the resonant inductor.

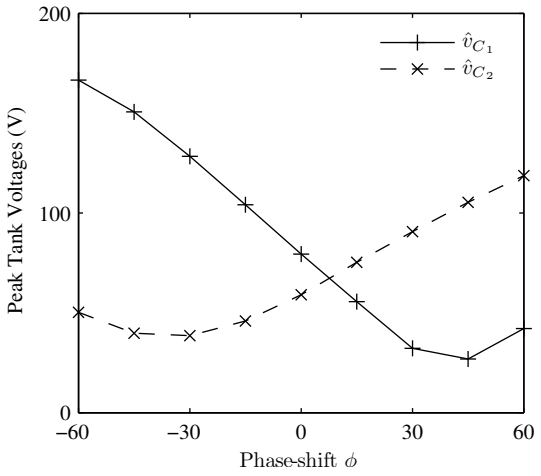

Figure 5.17: Simulation results of peak resonant tank voltages $\hat{v}_{C_1}$ and $\hat{v}_{C_2}$ at various phase shift angles ϕ

The maximum voltage that appears across the capacitor is plotted in Fig. 5.17 for various phase shift angles ϕ with constant θ at full load. Specific results at the operating points are given in Table 5.4. The capacitor is to be chosen for a peak voltage of at least $143V$ for tank1 and $108V$ for tank2 from Table 5.4. The plot in Fig. 5.17 forms the same pattern as in Fig. 5.16. It is to be noted that the peak voltages across the capacitors are very high when compared to their dc port voltages due to the resonant nature of the circuit.

As with the design of resonant inductor, the rms currents through each of the windings are required. The applied voltage across the transformer in one of the windings can be calculated from the output voltage . This determines the maximum flux density to be used in design of the core and number of turns. Due to the presence of diode bridge at the output side, the waveform that appears across the third winding of the transformer is a square wave with V_o as its maximum. A plot of the output voltage at various phase shift angles ϕ with constant θ at full load is shown in Fig. 5.18. It is observed that the output voltage does not vary widely with phase-shift angle ϕ. The maximum VA rating of the transformer is $550VA$ from Table 5.4 which is 1.1 times higher than the maximum output power. This is one of the disadvantages of using resonant converters as opposed to phase-shift converters where the ratio is almost unity. The calculation

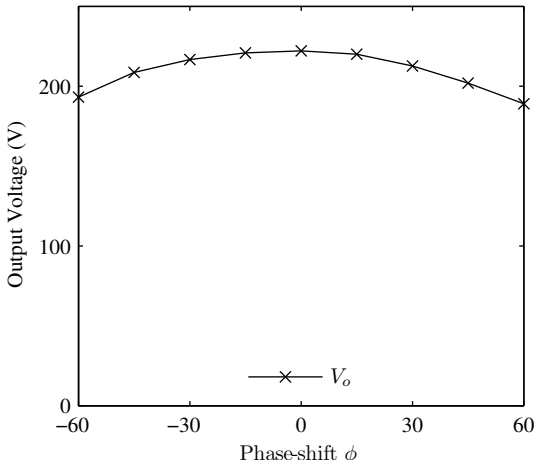

Figure 5.18: Simulation results of output voltage V_o at various phase shift angles ϕ

Table 5.3: Soft-switching range at various loads

Parameter	Load Percentage		
	100%	75%	50%
V_o	198.4	198	198.4
P_o	492	367.8	246
$i_{S1(on)}$	2.4	3.1	3.4
$i_{S2(on)}$	-8.3	-5.8	-3.5
$i_{S3(on)}$	-12.8	-11.3	-10.3

does not include the value of leakage inductance which will increase this ratio further since the leakage inductance forms a part of the resonant tank.

Power losses in the semiconductor switches can be divided into conduction and switching losses. Switching losses can be reduced to zero if Zero Voltage Switching (ZVS) is possible. Since rms currents are already determined, the conduction losses can be estimated from the on-state resistance $r_{ds(on)}$ of the Mosfets chosen. Current rating of the devices is chosen based on the conduction losses estimated above by simulation. The estimate of the conduction losses P_{cond} at various operating points of the converter is given in Table 5.4 as a function of $r_{ds(on)}$ of the chosen Mosfet denoted as r_d. Since the voltage across the switches when off is equal to the port voltage, the switches can be rated same as the input voltage ideally.

Softswitching or Zero Voltage Switching (ZVS) turn-on of switches in this case,

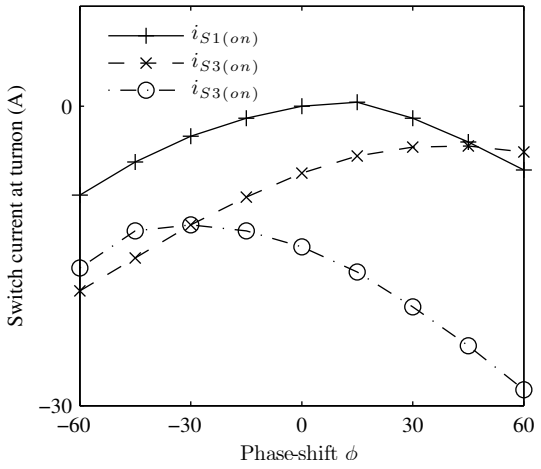

Figure 5.19: Simulation results of switch currents at turnon for various phase shift angles ϕ

is possible due to the resonant nature of the converter. If the current in the switch to be turned on is negative then the capacitor across the switch resonates with the resonant inductor reducing the switch voltage to zero. At that instant the free-wheeling diode across the switch starts conducting and the switch can be now turned on at zero voltage. The energy available to discharge the switch capacitance depends on the load and also the power flow between the sources. To determine the load range in which the converter switches perform ZVS, the magnitude and direction of current through the switches before turnon can be calculated from equations (5.11-5.15). Since the switches are complementary only three of the switches S_1, S_2 and S_3 currents are calculated. The magnitude and direction of the currents are plotted in Fig. 5.19 for various phase shift angles ϕ with constant θ at full load. In Table 5.3 the load is changed from full load to 50% load in steps of 25% while maintaining constant output voltage. It is observed from simulation that all the switches in the battery side converter perform ZVS. But ZVS in left leg switches S_1 and $\bar{S_1}$ depend on the load and power flow ratio.

The rms ripple current rating decides which capacitor to choose from datasheet since the value of the capacitor to be used is already known. The equivalent series resistance of the capacitor together with ripple current will contribute to a voltage drop and temperature rise. A plot of the rms ripple current in both input and output filters

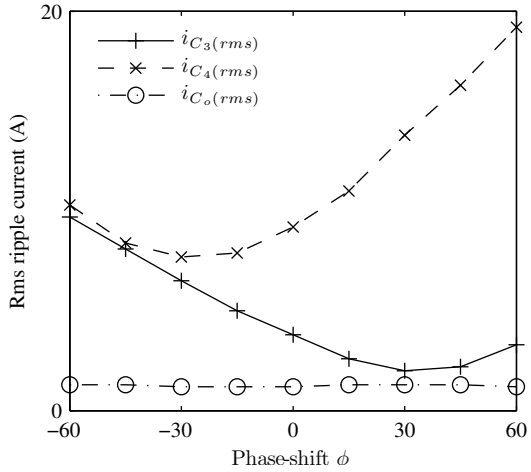

Figure 5.20: Simulation results of rmsripple currents at the input and output filter for various phase shift angles ϕ

for various phase shift angles ϕ with constant θ at full load is given in Fig. 5.20. As seen from the plot the output filter rms ripple current remains constant. The port2 filter current has its maximum when supplying the full load. From Table 5.4 the maximum rms ripple current rating for the input filters in port1 and port2 should be at least $9A$ and $16A$ respectively.

A summary of the simulated results in four operating points of the converter is presented in Table 5.4. Operating point B is for equal sharing of load between sources. The results presented in Table 5.4 are calculated in such a way to maintain approximately constant voltage of $200V$ at the output by varying the phase shifts. Switching frequency $F_s = 100kHz$ is used in all simulations which is 1.1 times the resonant frequencies of both the resonant tanks. The high frequency transformer is considered ideal since the leakage inductance will form part of the resonant tanks. All the results presented are in open loop. All the component ratings or specifications can be determined from Table 5.4 since the results are at worst-case operating points.

Table 5.4: Summary of simulation results at various operating points A, B, C and D of converter

Parameter	A	B	C	D	Units
P_1	2.2	248.4	493.4	493.2	W
P_2	476.9	238.99	1.5	-184.8	W
V_o	194.7	198.4	199.3	194	V
P_o	473.8	492	496.6	301.1	W
$\hat{i}_{L_1}$	5.9	9.6	18.6	18.4	A
$\hat{i}_{L_2}$	30.1	15.4	9.1	14.3	A
$i_{L_1(rms)}$	3.9	6.9	13.5	13.5	A
$i_{L_2(rms)}$	22.1	11.1	6.0	10.1	A
$\hat{v}_{C_1}$	39.6	71.1	142.5	141.5	V
$\hat{v}_{C_2}$	107.9	53	28.6	47.7	V
$P_{cond(S1)}$	$8r_d$	$23r_d$	$90r_d$	$90r_d$	W
$P_{cond(S3)}$	$243r_d$	$61r_d$	$19r_d$	$52r_d$	W
$(VA)_{tr}$	526.9	544.6	548.1	346.3	VA
$i_{S1(on)}$	-5.9	2.4	-6.4	-13.4	A
$i_{S2(on)}$	-5.9	-8.3	-15.2	-13.4	A
$i_{S3(on)}$	-23.5	-12.8	-9.0	-12.9	A
$i_{C_3(rms)}$	3.9	4.0	-23.5	9.2	A
$i_{C_4(rms)}$	16.3	8.3	6.0	8.3	A
$i_{C_o(rms)}$	1.2	1.2	1.2	.9	A

5.5 Experimental results

5.5.1 Experimental setup

A laboratory prototype of a three-port series resonant converter is constructed and tested in open loop. The converter is powered through an external dc source of $50V$ for port1. Three $12V, 20Ah$ batteries are used in series for port2. Since the PWM waveforms are always at 50% duty cycle, gate drive is easily implemented using pulse transformers. The output voltage is regulated in open loop at $200V$ by varying the phase-shift angles and an external load resistance of 125Ω is used. The Mosfets are IRF540Z with a rating of $100V$, $36A$ to reduce conduction losses. Filter capacitors are used at the input of each port. m_1 and m_2 are chosen to be 1.2 and 1.4 respectively which results in the three winding transformer turns ratio as 0.208 : 0.125 : 1. The converter parameters and switching frequency are kept same as in simulation. Digilent

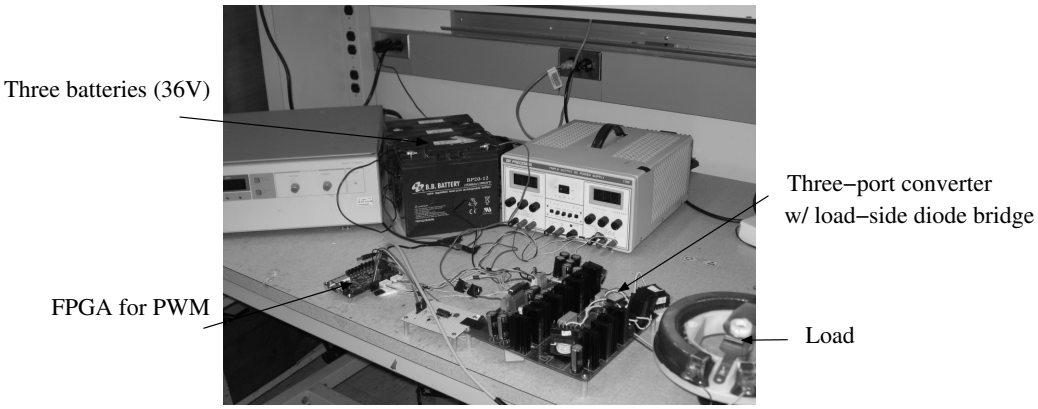

Figure 5.21: Hardware setup for testing the series resonant three-port converter with load-side diode bridge

Basys© FPGA board is used to program the phase shift angles and generate the PWM pulses for both the bridges. The pulses for the Mosfets are generated using a double-ramp carrier signal [40] and two control voltages for the two phase-shifts. It is to be noted that the phase-shift modulation for port1 bridge uses center modulation, i.e., the left and right legs get phase-shifted by the same angle from a center reference. The hardware setup for testing is shown in Fig. 5.21

5.5.2 Prototype results

Experimental waveforms of port1 bridge voltage and resonant tank current and port2 bridge voltage and resonant tank current are shown in Fig. 5.22 and Fig. 5.23 respectively for almost equal sharing of $350W$ load. The observed efficiency is 91%. All switches in port2 bridge turnon at zero voltage as can be observed from Fig. 5.23 since the tank current lags the applied port2 voltage. In port1 only the right leg having the switch $S3$ performs ZVS. $S1$ loses ZVS since the current before turn-on is positive as seen from Fig. 5.22. The winding3 voltage waveform is shown in Fig. 5.24 which is a square wave voltage with a magnitude of $200V$ and the current through the diode bridge is in phase with the voltage. Port1 dc voltage along with the port1 filtered input current is shown in Fig. 5.25 to indicate equal sharing of load. The zero phase-shift between the port1 and port2 bridge voltages can also be observed from Fig. 5.22 and Fig. 5.23, since they are triggered at the same time in the oscilloscope.

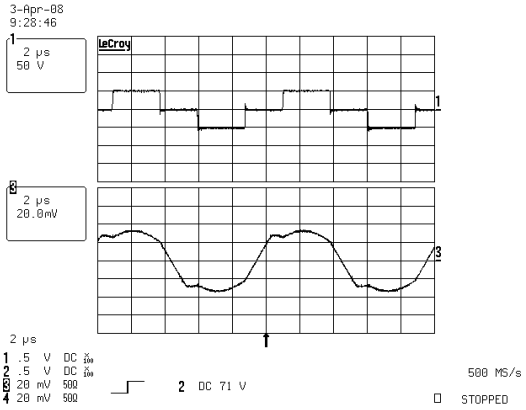

Figure 5.22: Observed Port1 bridge voltage v_{1hf}(50V/div) & resonant tank current i_{1hf}(4A/div) for

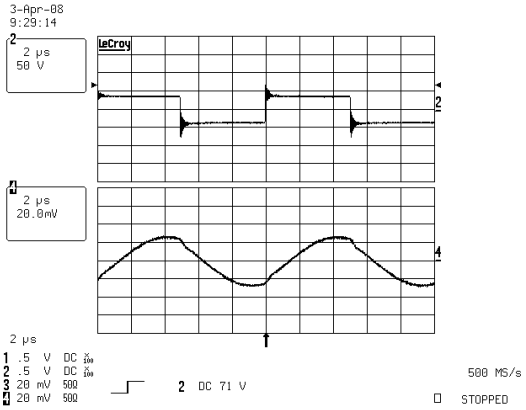

Figure 5.23: Observed Port2 bridge voltage $v_{2hf}(50V/div)$ & resonant tank current $i_{2hf}(10A/div)$ for operating point B

Results around operating point C are shown in Fig. 5.26 and Fig. 5.27. At this operating point, the power supplied by the battery is almost zero. The battery port voltage and the filtered battery currents are shown in Fig. 5.26 to indicate operation around the point B in Fig. 5.9. The output voltage is $200V$ as seen from Fig. 5.27. At this operating point also, port2 bridge switches operate in ZVS and port1 bridge, the left leg alone loses ZVS.

Fig. 5.28 and Fig. 5.29 show the bridge voltages and tank currents for battery charging mode of operation. In this operating mode also, all switches in port2 bridge

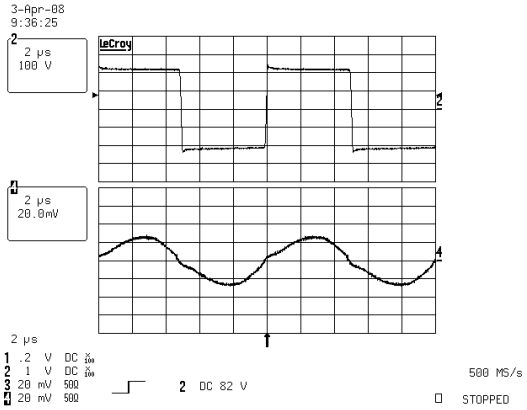

Figure 5.24: Observed Port3 diode bridge voltage v_{ohf}(100V/div) & transformer winding3 current i_{ohf}(2A/div) for operating point B

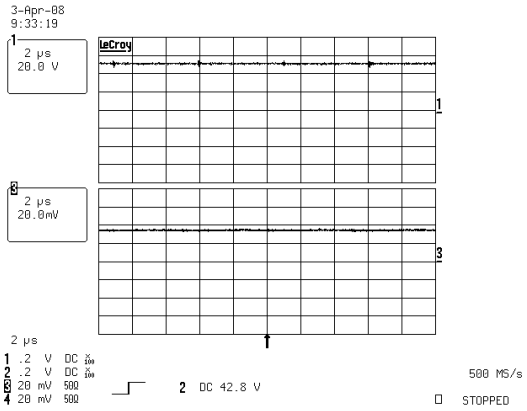

Figure 5.25: Observed port1 voltage V_1(20V/div) and port1 current I_1(2A/div) for operating point B

turnon at zero voltage. The average value of the filtered battery current shown in Fig. 5.30 is $-1.8A$. Port1 tank current has increased since this port is supplying both load and battery. The observed efficiency of the converter during this mode of operation is 85%. The phase-lag of the port2 bridge with respect to the port1 bridge can also be seen from Fig. 5.28 and Fig. 5.29.

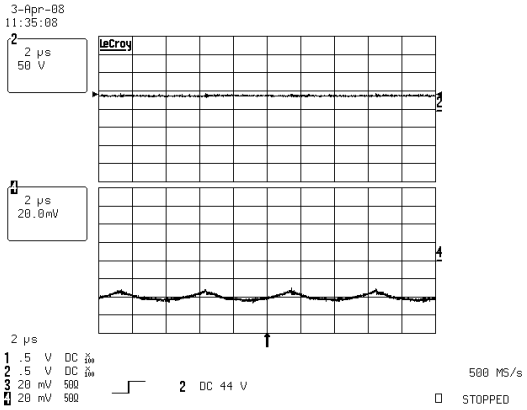

Figure 5.26: Observed port2 voltage V_2(20V/div) and port1 current I_2(0.4A/div) for operating point C

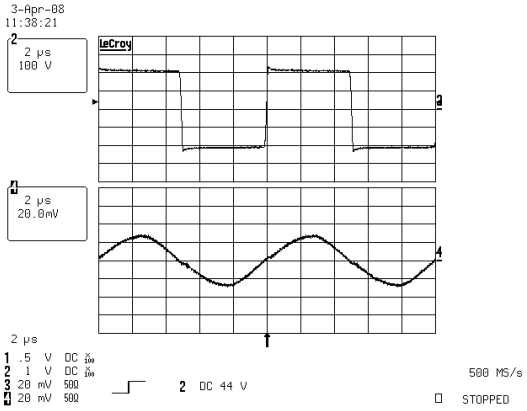

Figure 5.27: Observed Port3 diode bridge voltage v_{ohf}(100V/div) & transformer winding3 current i_{ohf}(2A/div) for operating point C

5.6 Conclusion

In this Chapter a three-port series resonant converter with load-side diode bridge is proposed. Due to the presence of diode bridge at the output of the converter, the phase-shift between the input ports and the output port is fixed. Phase-shift modulation is proposed for port1 bridge in addition to the phase-shift between port1 and port2 bridge outputs. With these two control variables, it has been proved by analysis, simulation and experimental results that the power flow between ports can be controlled. The analysis assumes sinusoidal tank current and voltage waveforms and steady state

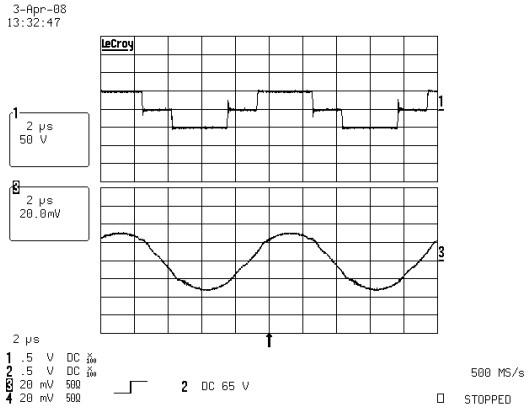

Figure 5.28: Observed Port1 bridge voltage v_{1hf}(50V/div) & resonant tank current I_{1hf}(10A/div) in battery charging mode

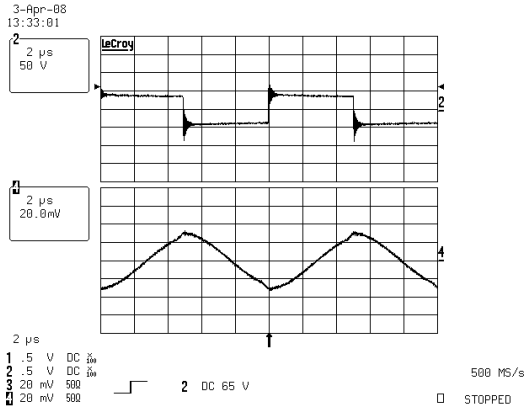

Figure 5.29: Observed Port2 bridge voltage v_{2hf}(50V/div) & resonant tank current i_{2hf}(10A/div) in battery charging mode

output voltage and port power expressions are derived. Error introduced by this approximation is discussed with simulation results. Due to the resonant nature of the circuit ZVS is possible and its region of operation is explained. A design procedure to select the resonant tank parameters and turns ratio of transformer is presented. Component specifications such as the rms currents, soft-switching range, rms ripple currents in filters and high-frequency transformer VA ratings are presented for a specific prototype. Simulation and experimental results of a laboratory prototype in open loop are presented. Bi-directional power flow capability of the converter is demonstrated in

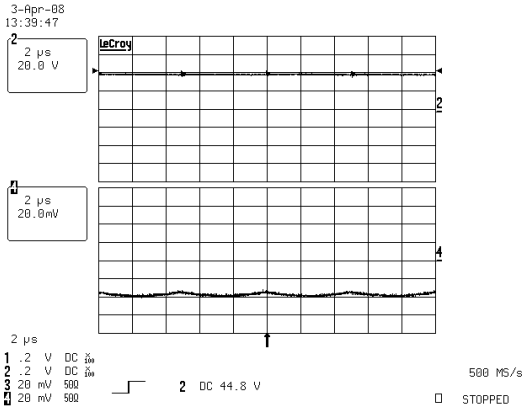

Figure 5.30: Observed battery voltage V_2(20V/div) & charging current I_2(1A/div) in battery charging mode

hardware using battery as one of the sources.

Chapter 6

Current-fed Three-port Converter

In the previous Chapters, three-port dc-dc converters using the principle of series resonance was explained. In this Chapter, another three-port converter topology is introduced which uses current-fed input ports as opposed to voltage-fed input ports. Current-fed input ports ensure dc currents at the input thereby eliminating the need of large filter capacitors. The proposed three-port current-fed converter is presented followed by detailed steady-state and dynamic analysis. Design, simulation and experimental results follow the analysis.

6.1 Introduction

Current-fed topologies have the distinct advantage of dc currents at all ports, over voltage-fed topologies. This is advantageous if the source connected to the port is a battery or fuel-cell. It eliminates the need of large filter capacitors at the input and thereby increasing the overall reliability of the converter. A two-port voltage-fed bi-directional dc-dc converter was proposed in [6] for high power applications. It uses two active bridges at the two ports with the transformer and the inductor at the high frequency side. The power flow is controlled by the phase-shift between active bridges along with or without PWM and frequency control. Such a Dual Active Bridge (DAB) converter [6] is shown in Fig. 6.1. The topology is voltage-fed and hence the converter

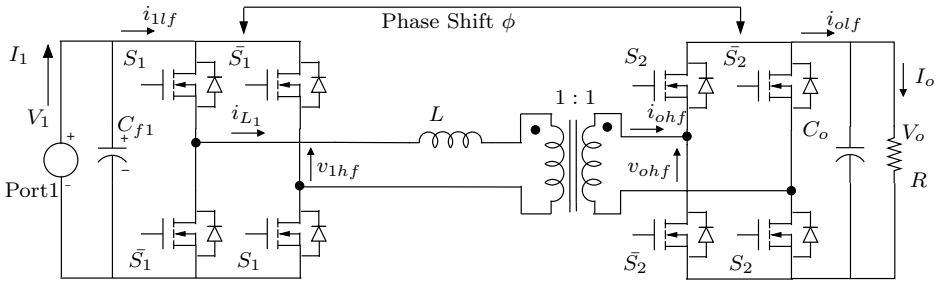

Figure 6.1: Circuit diagram of two-port dual active bridge (DAB) converter

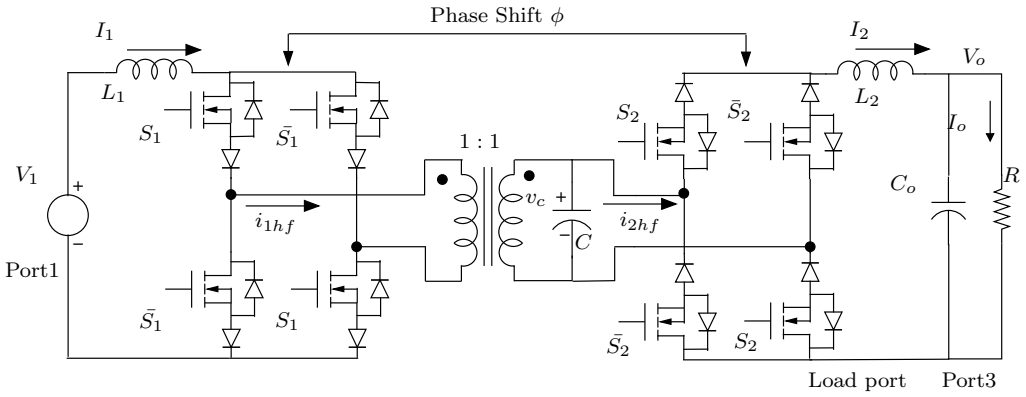

Figure 6.2: Circuit diagram of two-port inverse dual converter (IDC)

in Fig. 6.1 requires the use of input filter capacitors. A dual or a current-fed topology using the same principle of power flow was proposed in [42]. Such a converter is termed as Inverse Dual Converter (IDC) and is shown in Fig. 6.2. The power flow equations for DAB and IDC are given in (6.1) and (6.2) respectively.

$$P = \frac{V_1 V_o}{\omega_s L}\phi\left(1 - \frac{|\phi|}{\pi}\right) \quad \text{DAB} \tag{6.1}$$

$$P = \frac{I_1 I_o}{\omega_s C}\phi\left(1 - \frac{|\phi|}{\pi}\right) \quad \text{IDC} \tag{6.2}$$

$$\text{where} \;\; \omega_s = 2\pi F_s, \quad F_s = \text{Switching Frequency}$$

The waveforms of the two-port IDC is shown in Fig. 6.3. The converter operates with a phase-shift angle ϕ between the active bridges. The equations for the voltage across the capacitor C at different time instants are defined in (6.3)-(6.5). Solving these equations considering that the voltage magnitudes of V_a and V_b are equal, the average

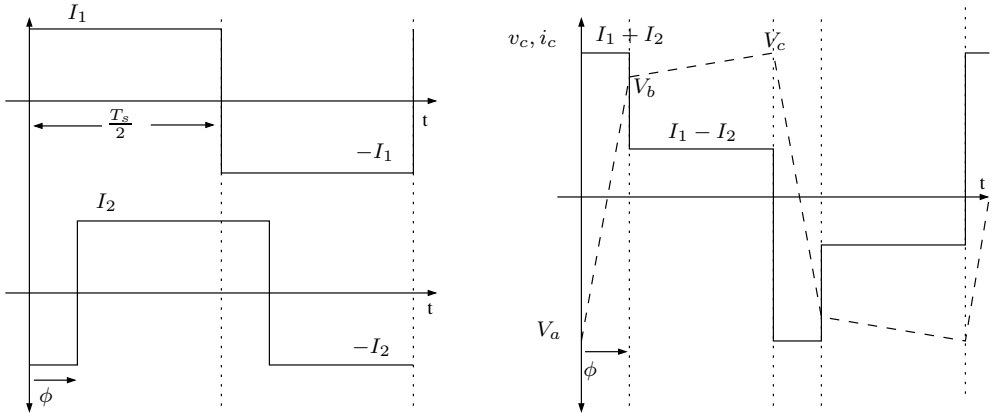

Figure 6.3: Waveforms of inverse dual converter

voltage at the input of each of the ports can be calculated. The output voltage is then given by (6.5). Considering power flow balance at the input and output the resulting power flow equation is given in (6.2).

$$v_c(t) = v_c(0) + \frac{1}{C}(I_1 + I_2)t; \quad 0 \le t \le \phi \tag{6.3}$$

$$= v_c(\phi) + \frac{1}{C}(I_1 - I_2)(t - \phi); \quad \phi \le t \le \frac{T_s}{2} \tag{6.4}$$

$$\text{given} \quad v_c(0) = V_a;\ v_c(\phi) = V_b;\ v_c(\frac{T_s}{2}) = V_c;\ v_c(0) = -v_c(\frac{T_s}{2})$$

$$V_o = \frac{I_1}{\omega_s C}\phi\left(1 - \frac{|\phi|}{\pi}\right) \tag{6.5}$$

In literature, a combination of voltage fed and boost input stage three-port converters have been proposed [15]. These topologies are useful in widely varying port voltage applications such as ultracapacitors. But it increases the number of power conversion stages. In this thesis, the concept of IDC is extended for three-port applications and is explained Section 6.2. This leads a single-stage power conversion using high-frequency ac link.

6.2 Proposed three-port converter

The current-fed three-port dc-dc converter is shown in Fig. 6.4. The converter circuit consists of three active full bridges whose inputs are connected to dc voltage ports

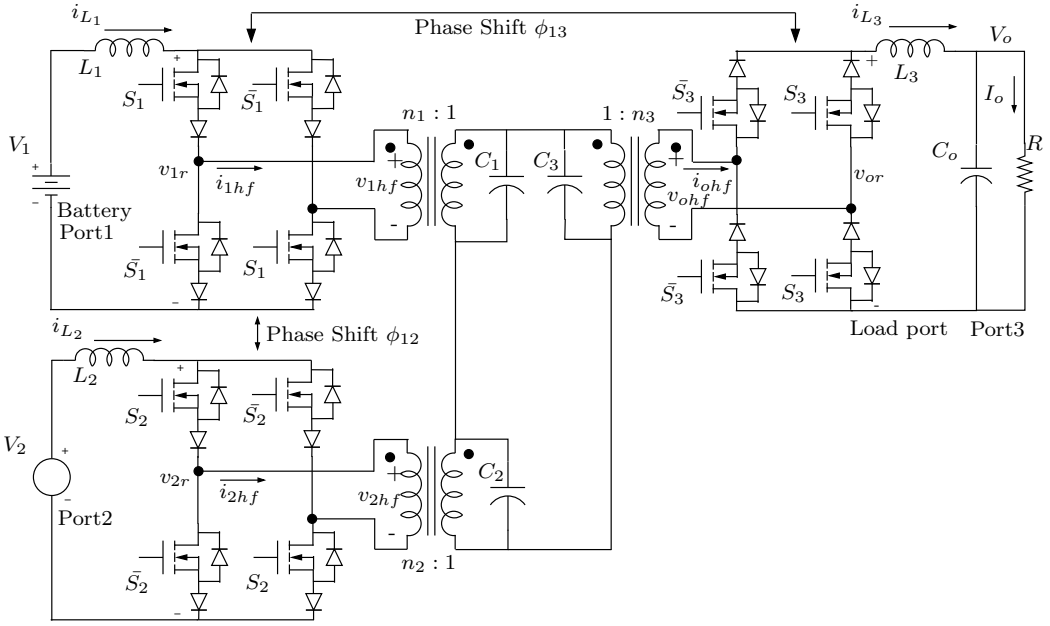

Figure 6.4: Proposed current-fed three-port dc-dc converter

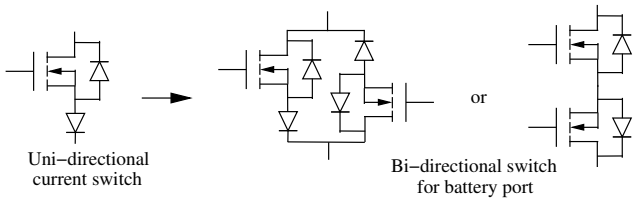

Figure 6.5: Bi-directional switches for battery side active bridge

through series inductors. Each switch in the bridge is realized using a Mosfet in series with a diode making it current unidirectional. The converter shown in Fig. 6.4 is unidirectional, i.e., the power flow can be only in one direction determined by the series diode in each switch. To enable bi-directional power flow in the battery port, a four-quadrant switch of the form shown in Fig. 6.5 is used. Although the four-quadrant switch can be driven as a single switch with the gates of the two Mosfets shorted together, it is not a good option for soft-switching due to commutation problems. Hence, the switches are turned on in such a way that the current is uni-directional. At the instant at which the current changes direction to enable battery charging, the other switch is turned on. In this way, current commutation problem is avoided. The switches operate

at 50% duty cycle with an overlap time between transitions.

The outputs of the bridges are connected to three separate transformers whose secondary are configured in delta, with high frequency capacitors in parallel to each transformer secondary. In voltage-fed converters such as the ones shown in Fig. 1.4 and Fig. 2.2, the three-winding transformer naturally sums the currents through it to zero or in other words, if the load is not regenerative, the current through the winding3 of the transformer is the sum of the currents in the other two windings. Since the current-fed topology is a dual of the voltage-fed topology, the voltages are summed up to zero by the delta connection of the secondaries of the three transformers. In other words, if the load is not regenerative, the voltage that appears across the load is the sum of the voltages across the other two transformer secondaries. The input port currents are dc due to the presence of inductor at the input side as shown in Fig. 6.4.

The capacitors C_1, C_2 and C_3 are high frequency capacitors of very low value $< 0.1\mu F$. The dc side inductors L_1, L_2 and L_3 are designed to have high values $> 2mH$ so that the port currents are dc with low ripple. Also, the resonant time period between the dc side inductors and the high frequency capacitors is very high when compared to the switching time period such that the charging of the capacitors is linear. The converter switches operate at constant switching frequency F_s. The active bridges are phase-shifted by the angles ϕ_{13} and ϕ_{12}. The following section discusses the steady-state analysis of the current-fed three-port converter.

6.3 Steady-state analysis

The square wave outputs and the corresponding phase-shifts are shown in Fig. 6.6a. The phase-shifts ϕ_{13} and ϕ_{12} are considered positive if i_{ohf} lags i_{1hf} and i_{2hf} lags i_{1hf} respectively. I_1, I_2 and I_3 are the magnitudes of the square waves. The waveforms of the capacitor voltages across each transformer primary are shown in Fig. 6.6b. In the series resonant circuit discussed in the previous chapters, sinusoidal approximation was possible due to the filtering action of the resonant circuit. In this current-fed converter, such an approximation is not possible, due to the high third and fifth harmonic component in the voltage waveforms as seen from Fig. 6.6b. Hence a different approach in deriving the steady-state equations is adopted. This approach is similar to the two-port

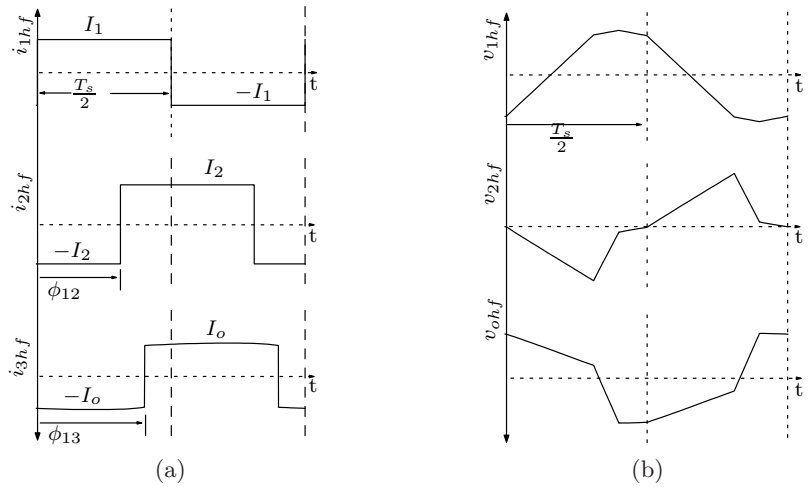

Figure 6.6: (a) High-frequency square wave current waveforms indicating the phase-shifts ϕ_{13}, ϕ_{12} (b) High-frequency voltage waveforms $v_{1hf}, v_{2hf}, v_{ohf}$ across the primary of each transformer

analysis presented in the previous section.

The equivalent circuit for analysis can be reduced to three phase-shifted square-wave current sources derived from input dc currents i_{L1}, i_{L2} and i_{L3}, supplying to the capacitors connected in delta, with transformers as isolation. The capacitors are connected to the secondary side of each transformer to minimize the effect of leakage inductance. The equivalent circuit is shown in Fig. 6.7. The phase shifts ϕ_{13} and ϕ_{12} are defined as in Fig. 6.6a. Since the capacitors are connected in delta, the sum of the voltages across all the secondaries is zero. From the delta circuit in Fig. 6.7, a star equivalent circuit can be constructed as shown in Fig. 6.7. This equivalent circuit can be used to calculate the power flow between ports. The relation between the capacitors in the star and delta equivalent circuits is given in (6.6-6.11).

$$C_1' = \frac{C_1C_2 + C_2C_3 + C_3C_1}{C_2} \tag{6.6}$$

$$C_2' = \frac{C_1C_2 + C_2C_3 + C_3C_1}{C_3} \tag{6.7}$$

$$C_3' = \frac{C_1C_2 + C_2C_3 + C_3C_1}{C_1} \tag{6.8}$$

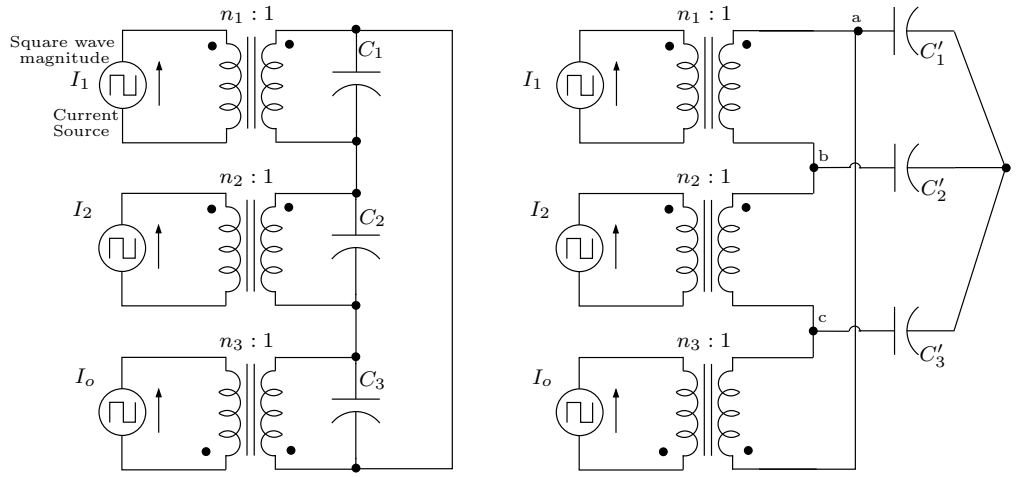

Figure 6.7: Equivalent circuit for steady-state analysis, Delta equivalent with capacitors $C_1, C_2 \& C_3$ and Star equivalent with capacitors $C_1', C_2' \& C_3'$

$$\text{Similarly} \quad C_1 = \frac{C_1' C_2'}{C_1' + C_2' + C_3'} \tag{6.9}$$

$$C_2 = \frac{C_2' C_3'}{C_1' + C_2' + C_3'} \tag{6.10}$$

$$C_3 = \frac{C_1' C_3'}{C_1' + C_2' + C_3'} \tag{6.11}$$

Note that in Section 2.5.1 an extended cantilever model of the transformer has been derived. In Fig. 2.9, the delta connected impedances is used to calculate the power flow between the buses. Once this is known, the net power is calculated using (2.42-2.44). In a similar way, the delta connected capacitors are transformed to a star equivalent such that the voltage developed across each capacitor is due to the difference in the two port currents flowing through it. Using each one of the star equivalent capacitor, the power flow between the ports are calculated. As an example, the power flow between port1 and port3 can be derived by applying Kirchhoff's current law (KCL) at node 'a' in Fig. 6.7. The resulting equation is given in (6.12). Similarly, the power flow equations are derived for the other two capacitors and given in (6.13) and (6.14). Having known the power flow between ports, the net power from each of the ports can be calculated using

(6.15-6.17).

$$P_{13} = \frac{n_1 n_3 I_1 I_o}{\omega_s C_1'} \phi_{13} \left(1 - \frac{|\phi_{13}|}{\pi}\right) \tag{6.12}$$

$$P_{21} = \frac{n_1 n_2 I_2 I_1}{\omega_s C_2'} \phi_{21} \left(1 - \frac{|\phi_{21}|}{\pi}\right) = -P_{12} \tag{6.13}$$

$$P_{32} = \frac{n_2 n_3 I_2 I_o}{\omega_s C_3'} \phi_{32} \left(1 - \frac{|\phi_{32}|}{\pi}\right) = -P_{23} \tag{6.14}$$

$$P_1 = P_{13} + P_{12} \tag{6.15}$$

$$P_2 = P_{23} - P_{12} \tag{6.16}$$

$$P_o = P_{23} + P_{13} \tag{6.17}$$

$$\text{Also, } \phi_{12} = -\phi_{21}; \quad \phi_{23} = -\phi_{32}$$

Under dc steady state, since the average of the voltage across the series inductor is zero, the average voltage that appears at the input of the active bridges can be equated to the port voltage as shown in (6.18). From (6.15-6.17) the power drawn from the input ports and the power delivered to the load can be calculated. The load voltage is given by (6.19) and the load power by (6.21).

$$V_1 = \bar{v}_{1r}; \quad V_2 = \bar{v}_{2r}; \quad V_o = \bar{v}_{or}; \tag{6.18}$$

$$V_o = \frac{n_1 n_3 I_1}{\omega_s C_1'} \phi_{13} \left(1 - \frac{|\phi_{13}|}{\pi}\right) + \frac{n_2 n_3 I_2}{\omega_s C_3'} \phi_{23} \left(1 - \frac{|\phi_{23}|}{\pi}\right) \tag{6.19}$$

$$P_o = V_o I_o = \frac{V_o^2}{R} \tag{6.20}$$

$$P_o = \frac{n_1 n_3 I_1 I_o}{\omega_s C_1'} \phi_{13} \left(1 - \frac{|\phi_{13}|}{\pi}\right) + \frac{n_2 n_3 I_2 I_o}{\omega_s C_3'} \phi_{23} \left(1 - \frac{|\phi_{23}|}{\pi}\right) \tag{6.21}$$

In the output voltage equation (6.19), the values of the port currents I_1 and I_2 are unknown. Since $V_o = I_o R$, the input port currents in terms of the output voltage V_o can be derived from the port power equations and they are given in (6.22) and (6.23). Substituting these values in (6.19), the final equation for the output voltage V_o is given by (6.24).

$$I_1 = \frac{-V_2 + \frac{n_2 n_3 V_o}{\omega_s R C_3'} \phi_{23} \left(1 - \frac{|\phi_{23}|}{\pi}\right)}{\frac{n_1 n_2}{\omega_s C_2'} \phi_{12} \left(1 - \frac{|\phi_{12}|}{\pi}\right)} \tag{6.22}$$

Table 6.1: Current-fed three-port converter specifications

Specification	**Value**
Port1 voltage V_1	$50V$
Port2 voltage V_2	$36 - 40V$
Output power P_o	$0.5kW$
Output voltage V_o	$200V$

$$I_2 = \frac{V_1 - \frac{n_1 n_3 V_o}{\omega_s R C_1'}\phi_{13}\left(1 - \frac{|\phi_{13}|}{\pi}\right)}{\frac{n_1 n_2}{\omega_s C_2'}\phi_{12}\left(1 - \frac{|\phi_{12}|}{\pi}\right)} \tag{6.23}$$

$$V_o = \frac{C_2'/n_1 n_2}{\phi_{12}\left(1 - \frac{|\phi_{12}|}{\pi}\right)}\left[\frac{V_1}{C_3'/n_2 n_3}\phi_{23}\left(1 - \frac{|\phi_{23}|}{\pi}\right) - \frac{V_2}{C_1'/n_1 n_3}\phi_{13}\left(1 - \frac{|\phi_{13}|}{\pi}\right)\right] \tag{6.24}$$

The load voltage V_o (6.24) is independent of the load resistance R, and hence theoretically the output voltage remains constant for load variations. This is one of the advantages of this converter. In the practical circuit, the parasitic resistances and the mosfet on-state resistances $r_{ds(on)}$ will contribute to a drop in voltage as load increases. The final port1 and port2 power equations are given by (6.25) and (6.26) respectively.

$$P_1 = \frac{n_1 n_3 I_1 I_o}{\omega_s C_1'}\phi_{13}\left(1 - \frac{|\phi_{13}|}{\pi}\right) + \frac{n_1 n_2 I_1 I_2}{\omega_s C_2'}\phi_{12}\left(1 - \frac{|\phi_{12}|}{\pi}\right) \tag{6.25}$$

$$P_2 = \frac{n_2 n_3 I_2 I_o}{\omega_s C_3'}\phi_{23}\left(1 - \frac{|\phi_{23}|}{\pi}\right) - \frac{n_1 n_2 I_1 I_2}{\omega_s C_2'}\phi_{12}\left(1 - \frac{|\phi_{12}|}{\pi}\right) \tag{6.26}$$

The design requirements for the current-fed three-port converter are the same as the series resonant three-port converter explained in Chapter 4. The limit equations for the port power and output power are repeated here (6.27-6.28). The converter specifications are given in Table 6.1. The base power and the base voltage are chosen as the required output power and the required output voltage. Hence the converter needs to maintain a constant $V_{o,pu} = 1.0$ under various power sharing ratios and load power. Using the steady-state equations of output voltage (6.24) and port power (6.25-6.26) the converter parameters are designed and presented in Table 6.2. The source-side inductances L_1, L_2 are large enough such that the port currents can be assumed dc and for steady-state

Table 6.2: Current-fed three-port converter parameters

Converter Parameter	**Value**
Port1 Capacitor C_1	$15.0nF$
Port2 Capacitor C_2	$3.3nF$
Port3 Capacitor C_2	$6.2nF$
Turns ratio n_1	0.33
Turns ratio n_2	0.42
Turns ratio n_3	1

analysis the average voltages across these inductors are zero.

$$0 \leq P_{1,pu} \leq 1 \tag{6.27}$$

$$-0.5 \leq P_{2,pu} \leq 1 \tag{6.28}$$

$$\text{Since} \quad P_{1,pu} + P_{2,pu} = P_{o,pu}$$

$$-0.5 \leq P_{o,pu} \leq 1 \tag{6.29}$$

A plot of the output voltage in per unit as a function of phase-shift angle ϕ_{12} at constant ϕ_{13} is shown in Fig. 6.8a. Similarly the output voltage as a function of phase-shift angle ϕ_{13} is plotted in Fig. 6.8b. The requirement for the converter is to maintain a constant output voltage. It can be observed that to maintain an output voltage of $1pu$, the value of phase-shift ϕ_{13} should be higher than 90^o for values of $\phi_{12} > 40^o$. At low values of ϕ_{13}, the output voltage can go negative unless the phase-shift ϕ_{12} is reduced correspondingly.

The output voltage can theoretically reach infinity when phase shift ϕ_{12} tends toward zero, but parasitic resistances limit its magnitude. Hence in the plots, the value of ϕ_{12} is limited to 40^o. The turns ratio of the three high frequency transformers can also be used to vary the voltage step-up ratios. Note that the ports are still voltage ports as used in the three-port series resonant converter but they are converted to current ports through the use of series inductors. Hence the voltage plots with respect to the phase-shifts are very different from what has been presented in the three-port series resonant converter. Several pairs of phase-shifts can achieve $1pu$ output voltage but additional constraint is

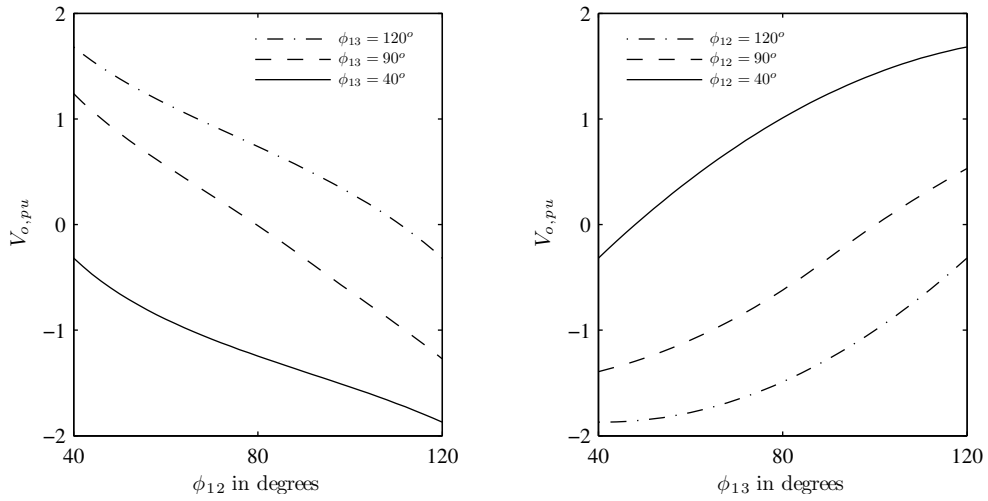

Figure 6.8: Output voltage in per unit Vs (a) Phase-shift angle ϕ_{12} for different values of ϕ_{13} (b)Phase-shift angle ϕ_{13} for different values of ϕ_{12}

specified for port power whose plots are discussed in the following paragraph.

A plot of the port1 power and port2 power in per unit for variations in ϕ_{12} under constant ϕ_{13} are shown in Fig. 6.9. It can be observed from Fig. 6.9b that the variation of port2 power is less when compared to port1 power in Fig. 6.9a. Also port1 power goes both positive and negative. For these reasons, it is more advantageous to connect batteries to port1 and fuel-cell to port2. Fuel cell has very slow dynamic response and it is also required to use constant power from fuel-cell. The output power is the sum of these two plots.

The two plots are repeated in Fig. 6.10 at reduced load, i.e., the load resistance is increased 2.5 times. When the load decreases 2.5 times, the power from port2 reduces slightly and the power from port1 goes negative. This is looking at the same operating point from the two figures Fig. 6.9a and Fig. 6.10a. Note that the output voltage is independent of load and will be still maintained constant. So the phase-shifts need not change much for reduced load and can remain the same as in full load for small load variations. In other words, no output voltage control is ideally necessary if the load is reduced. When port1 is chosen as battery port and port2 as fuel-cell port, the power

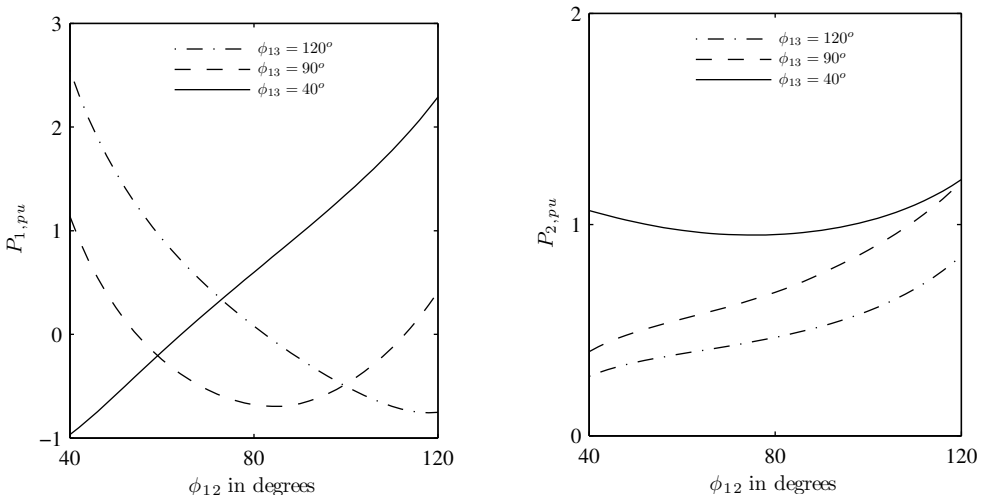

Figure 6.9: Port power in per unit Vs phase-shift angle ϕ_{12} for different values of ϕ_{13} at full load for (a) Port1 and (b) Port2

from fuel-cell under low loads can be used to charge the battery.

The high frequency capacitors and turns ratio are appropriately chosen to make use of the above characteristic. The battery charging current is dc due to the input side inductor. Another mode of operation is that only port2 supplies the load, which can also be achieved by varying the phase-shifts. The battery side full bridge in this case can be switched off. The salient features of the current-fed three-port converter is summarized below based on the analysis presented in this section.

1. The output voltage is independent of load variations

2. As the load decreases, port2 power does not change significantly and this port's extra power is used to charge the battery connected to port1

3. When one of the ports fail or need not be used, it can be switched off and used as a two-port converter

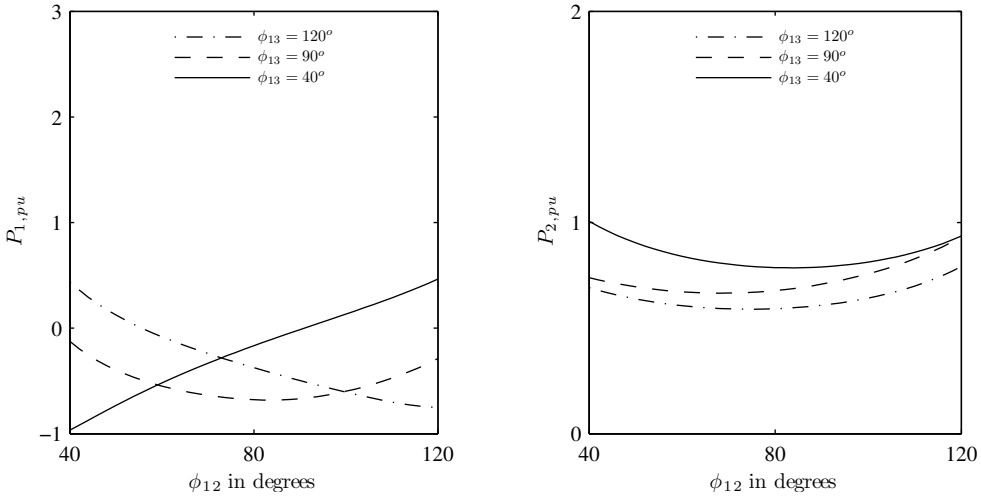

Figure 6.10: Port power in per unit Vs phase-shift angle ϕ_{12} for different values of ϕ_{13} at reduced load for (a) Port1 and (b) Port2

6.4 Dynamic analysis

In this section dynamic analysis of the converter is presented. In the previously proposed three-port series resonant converter, sinusoidal approximation of the tank currents and voltages were possible due to the filtering action of the resonant tanks. But in the current-fed three-port converter such approximations can lead to more error due to the presence of significant third and fifth harmonic components in the voltage waveforms across the capacitors. Generalized averaging method can still be applied by taking the effect of third and fifth harmonics. But the number of state equations increases from 6 to 18. A small signal model is presented in this section for variations around an operating point in this case full load operation.

6.4.1 State-space representation of the converter

The converter has a total of 3 inductors and 4 capacitors and hence 7 state equations can be written. But the voltage across the capacitor placed in winding3 of the transformer is the sum of the other two transformer voltages due to the delta connection of the secondaries. Hence the total number of equations reduce to 6. The state equations

(6.30)-(6.35) are given below. The voltage polarity and current direction are indicated in the Fig. 6.4. The on-state resistance $r_{ds(on)}$ of the Mosfets are not included in the equations.

$$\begin{aligned}\dot{v}_{C_1} &= n_1 i_{L_1}\left(\frac{1}{C_1'}+\frac{1}{C_2'}\right)\mathrm{sgn}(\sin(\omega_s t)) - \frac{n_2}{C_2'} i_{L_2}\mathrm{sgn}(\sin(\omega_s t-\phi_{12})) \\ &\quad - \frac{n_3}{C_1'} i_{L_3}\mathrm{sgn}(\sin(\omega_s t-\phi_{13})) \qquad (6.30)\\ \dot{v}_{C_2} &= -\frac{n_1}{C_2'} i_{L_1}\mathrm{sgn}(\sin(\omega_s t)) - n_2 i_{L_2}\left(\frac{1}{C_2'}+\frac{1}{C_3'}\right)\mathrm{sgn}(\sin(\omega_s t-\phi_{12})) \\ &\quad - \frac{n_3}{C_3'} i_{L_3}\mathrm{sgn}(\sin(\omega_s t-\phi_{13})) \qquad (6.31)\\ \dot{i}_{L_1} &= \frac{V_1}{L_1} - \frac{n_1}{L_1} v_{C_1}\mathrm{sgn}(\sin(\omega_s t)) \qquad (6.32)\\ \dot{i}_{L_2} &= \frac{V_2}{L_2} - \frac{n_2}{L_2} v_{C_2}\mathrm{sgn}(\sin(\omega_s t-\phi_{12})) \qquad (6.33)\\ \dot{i}_{L_3} &= \frac{n_3}{L_3}\left(v_{C_1}+v_{C_2}\right)\mathrm{sgn}(\sin(\omega_s t-\phi_{13})) - \frac{v_o}{L_3} \qquad (6.34)\\ \dot{v}_o &= \frac{i_{L_3}}{C_o} - \frac{v_o}{RC_o} \qquad (6.35)\end{aligned}$$

6.4.2 Averaging

The dynamics of the voltages across the capacitors are very fast when compared to the dynamics of the output and port currents. Using a similar time-scaling process used in Chapter 3, the equations for the fast system can be reduced to a static equation. To remove the switching function in the equation, averaging of the state equations is performed. The port1 side inductor sees the average voltage $\bar{v}_{1r}$ whose value can be calculated from the steady-state equations since the dynamics of this variable is very fast. Hence the averaged state equations are given in (6.36-6.39)

$$\begin{aligned}\dot{\bar{i}}_{L_1} &= \frac{V_1}{L_1} - \frac{n_1 n_2}{L_1\omega_s C_2'}\bar{i}_{L_1}\ \phi_{12}\left(1-\frac{|\phi_{12}|}{\pi}\right) \\ &\quad - \frac{n_1 n_3}{L_1\omega_s C_1'}\bar{i}_{L_3}\ \phi_{13}\left(1-\frac{|\phi_{13}|}{\pi}\right) \qquad (6.36)\\ \dot{\bar{i}}_{L_2} &= \frac{V_2}{L_2} - \frac{n_1 n_2}{L_2\omega_s C_2'}\bar{i}_{L_1}\ \phi_{12}\left(1-\frac{|\phi_{12}|}{\pi}\right)\end{aligned}$$

$$- \frac{n_2 n_3}{L_2 \omega_s C_3'} \bar{i}_{L_3} \ \phi_{23} \left(1 - \frac{|\phi_{23}|}{\pi}\right) \tag{6.37}$$

$$\dot{\bar{i}}_{L_3} = -\frac{v_o}{L_3} + \frac{n_1 n_3}{L_3 \omega_s C_1'} \bar{i}_{L_1} \ \phi_{13} \left(1 - \frac{|\phi_{13}|}{\pi}\right) - \frac{n_2 n_3}{L_3 \omega_s C_3'} \bar{i}_{L_2} \ \phi_{23} \left(1 - \frac{|\phi_{23}|}{\pi}\right) \tag{6.38}$$

$$\dot{v}_o = \frac{\bar{i}_{L_3}}{C_o} - \frac{v_o}{RC_o} \tag{6.39}$$

A small signal model is derived for perturbations in the load $\tilde{i}_o$ and phase shifts $\tilde{\phi}_{13}, \tilde{\phi}_{12}$ around the operating point. The small signal perturbations are defined as in (6.40-6.42). The nominal values are defined with a subscript 'n'.

$$\text{Define} \quad \bar{x} = [\bar{i}_{L_1} \ \ \bar{i}_{L_2} \ \ \bar{i}_{L_3} \ \ v_o]^T \tag{6.40}$$

$$\bar{x} = \bar{X}_n + \tilde{\bar{x}} \tag{6.41}$$

$$\phi_{12} = \phi_{12n} + \tilde{\phi}_{12}; \quad \phi_{13} = \phi_{13n} + \tilde{\phi}_{13} \tag{6.42}$$

Ignoring the second order terms the small signal model can be derived as in (6.43). The matrix A is obtained from (6.36-6.39).

$$\dot{\tilde{\bar{x}}} = A\tilde{\bar{x}} + f_1\tilde{\phi} + f_2\tilde{i}_o \tag{6.43}$$

$$f_1 = \begin{pmatrix} -\frac{n_1 n_3}{L_1 \omega_s C_1'} \bar{X}_{3n} K_{13} & -\frac{n_1 n_2}{L_1 \omega_s C_2'} \bar{X}_{2n} K_{12} \\ -\frac{n_2 n_3}{L_2 \omega_s C_3'} \bar{X}_{3n} K_{23} & \frac{n_2 n_3}{L_2 \omega_s C_3'} \bar{X}_{3n} K_{23} + \frac{n_1 n_2}{L_2 \omega_s C_2'} \bar{X}_{1n} K_{12} \\ \frac{n_1 n_3}{L_3 \omega_s C_1'} \bar{X}_{1n} K_{13} + \frac{n_2 n_3}{L_3 \omega_s C_3'} \bar{X}_{2n} K_{23} & -\frac{n_2 n_3}{L_3 \omega_s C_3'} \bar{X}_{2n} K_{23} \end{pmatrix} \tag{6.44}$$

$$K_{13} = \left(1 - \frac{2|\phi_{13n}|}{\pi}\right); \quad K_{12} = \left(1 - \frac{2|\phi_{12n}|}{\pi}\right);$$

$$K_{23} = \left(1 - \frac{2|\phi_{23n}|}{\pi}\right);$$

$$f_2 = [0 \ \ 0 \ \ 0 \ \ 0 \ \ 1/C_o]^T \tag{6.45}$$

Having obtained the small signal model with two inputs ϕ_{12}, ϕ_{13} and the operating point, controller can be designed to regulate the output voltage and one of the port currents. The following section presents simulation results of the closed loop controller.

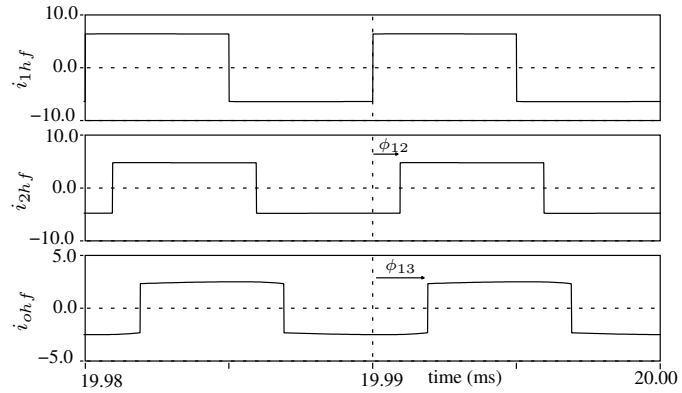

Figure 6.11: Simulation results of the three high-frequency currents through the transformers showing phase-shifts ϕ_{12} and ϕ_{13} for equal load sharing

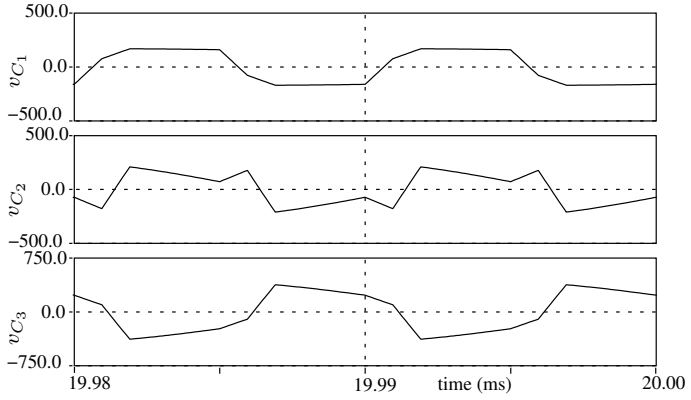

Figure 6.12: Simulation results of the voltage across the three high-frequency capacitors C_1, C_2 and C_3 for equal load sharing

6.5 Results

6.5.1 Simulation results

Simulation of the current-fed three-port dc-dc converter is done in Saber© with port1 chosen as battery port with a voltage range of $36 - 40V$. Port2 is chosen as a constant voltage port with a value of $50V$. The turns ratio, converter parameters given in Table 6.2 are used. The simulation results are given for two operating conditions, equal power sharing of $500W$ load and battery charging under reduced load. The switching frequency for simulation is chosen as $100kHz$.

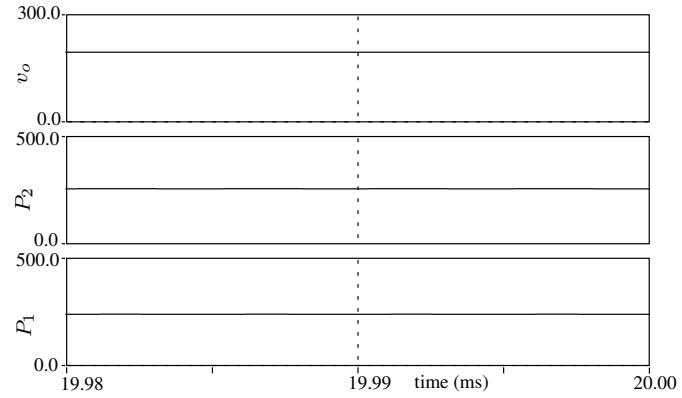

Figure 6.13: Simulation results of the output voltage v_o, port1 power P_1 and port2 power P_2 for equal load sharing

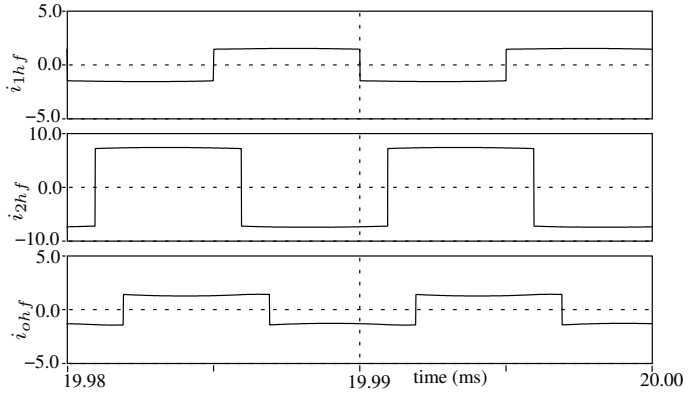

Figure 6.14: Simulation results of the three high-frequency currents through the transformers for battery charging operation

The phase-shifts for equal sharing of output power of $500W$ were found to be $\phi_{13} = 68.9^o$ and $\phi_{12} = 34.1^o$ obtained by solving in Mathematica the equations (6.24) and (6.23). These phase-shifts are substituted in the simulation and the output voltage is obtained as $195V$, the drop due to the conduction losses in the switches. Note that as compared to the previously proposed series resonant three-port converter, the steady-state equations are exact without any sinusoidal approximation. The phase-shift between the high frequency square wave currents into the transformer windings is shown in Fig. 6.11. The values of the input port currents can be deduced from the magnitude of the square wave currents as $6.25A$ and $5.00A$ for port1 and port2 respectively. The

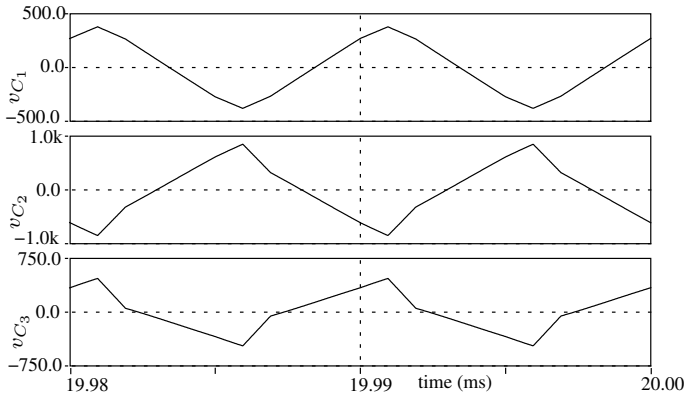

Figure 6.15: Simulation results of the voltage across the three high-frequency capacitors C_1, C_2 and C_3 for battery charging operation

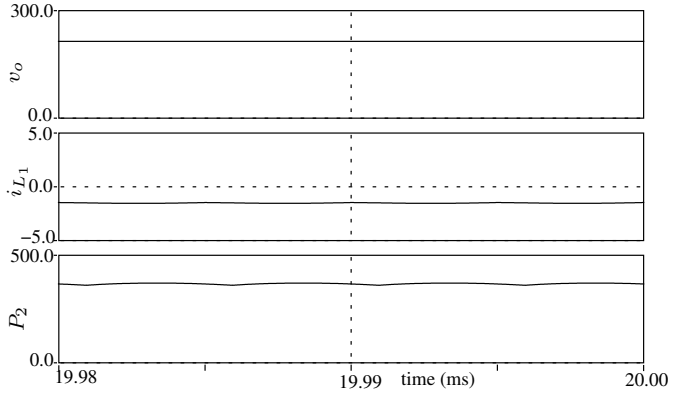

Figure 6.16: Simulation results of the output voltage v_o, port1 current i_{L_1} and port2 power P_2 for battery charging operation

voltages across the three capacitors connected at the secondary of each transformer are shown in Fig. 6.12. The average of the voltages are zero. The voltage magnitudes are high since they are measured at the high-voltage side of the transformer.

The output voltage along with the port1 and port2 power are shown in Fig. 6.13. The load resistance used is 80Ω for a full load of $500W$. The equal power sharing between the two ports can be observed from Fig. 6.13.

Simulation results for battery charging mode of operation are shown in Fig. 6.14-6.16. The load is reduced by half and the current in the battery port reverses direction to $-2A$ as seen from Fig. 6.16. The power supplied by port2 increases to $350W$. The

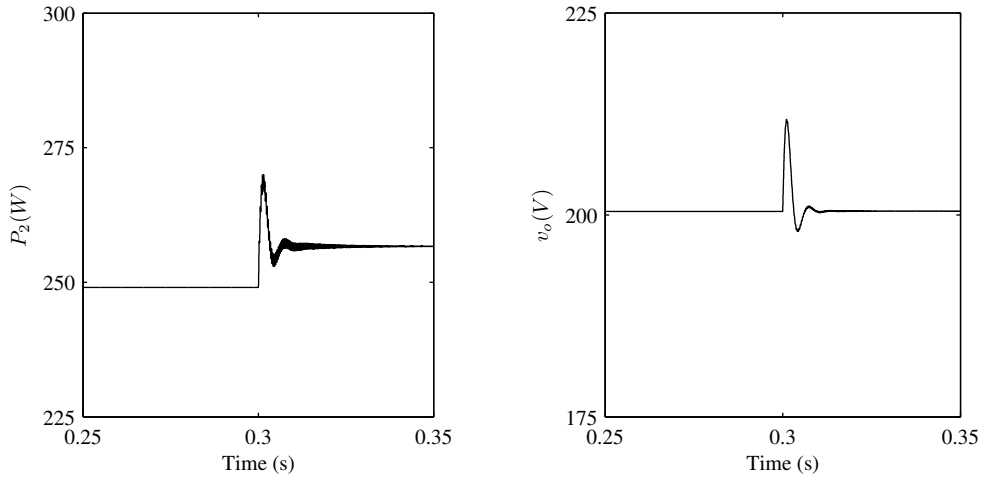

Figure 6.17: The response of (a) Port2 power (b) Output voltage for a 10% step decrease in load in open loop

high frequency capacitor voltages are shown in Fig. 6.15 where the voltage peak across capacitor C_2 reaches almost $1000V$. This is one of the disadvantages of this converter. This high voltage not only increases the peak rating of the devices but also increases the transformer turns. Due to the change in current direction in port1, the phase-shift changes by 180^o but it does not affect the equations due to symmetry around the 180^o point. Also during transients, the current in port1 can go both positive and negative and hence requires a current sensor at the input to decide which of the uni-directional current switches have to be turned on.

The dynamic equations of the averaged model (6.36-6.39) are modeled in Simulink. Open loop simulation for a small perturbation in load (10% decrease from full load) is shown in Fig. 6.17. It can be observed from Fig. 6.17a that the port2 power changes by $8W$ for a $50W$ decrease in load. Since the power variation is less in this port, a source such as fuel-cell can be connected to port2. But a closed loop control can maintain a constant power from this port. The output voltage in Fig. 6.17b returns to its previous steady-state value since it is independent of load.

Closed loop simulation results for the same perturbation in load is shown in Fig. 6.18. From the small-signal model derived in the previous section, proportional plus

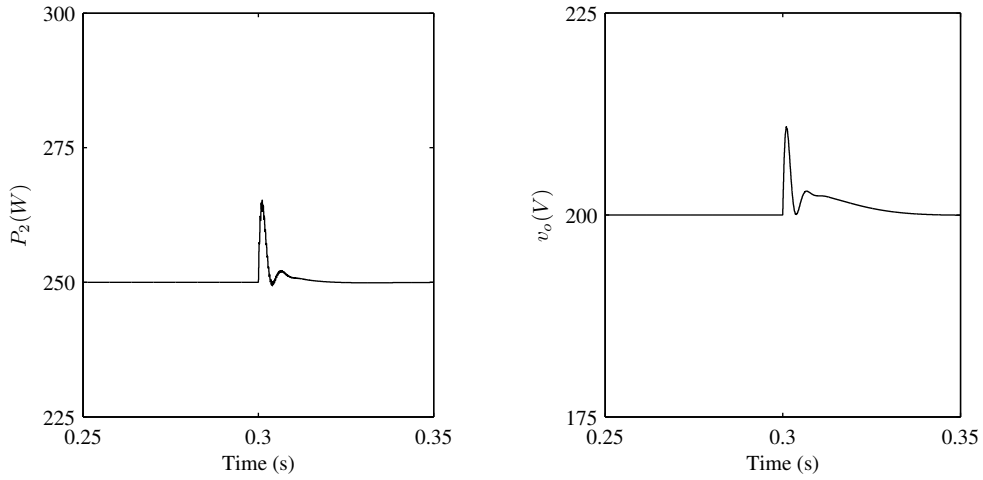

Figure 6.18: The response of (a) Port2 power (b) Output voltage for a 10% step decrease in load in closed loop

integral controllers are designed to regulate the output voltage and the port2 power. From Fig. 6.18a it can be observed that the port2 power returns to its original value of $250W$ in the simulation. The control method suggested in [5] is used here with two control loops designed from the small-signal model.

6.5.2 Experimental results

A laboratory prototype is constructed to test the performance of the current-fed three-port converter. The converter is designed for the specifications given in Table 6.1 and the parameters in Table 6.2. The switches in the converter are current uni-directional which require overlap times between switching transitions. A pulse transformer cannot be used for the gate-drive eventhough the pulses are at 50% duty cycle since such a configuration can give only dead-times between transitions. In this prototype, 12 isolated power supplies are used for the gate-drive circuits. The PWM pulses are generated by FPGA and sent through optocouplers to the gate-driver ICs. The pulse generation module in FPGA is similar to the one used in Section 4.4 and illustrated in Fig. 4.16.

Results of the capacitor voltages v_{C_1} and v_{C_2} are shown in Fig. 6.19 for power sharing mode of operation. The high-frequency square-wave currents i_{1hf} and i_{2hf} and

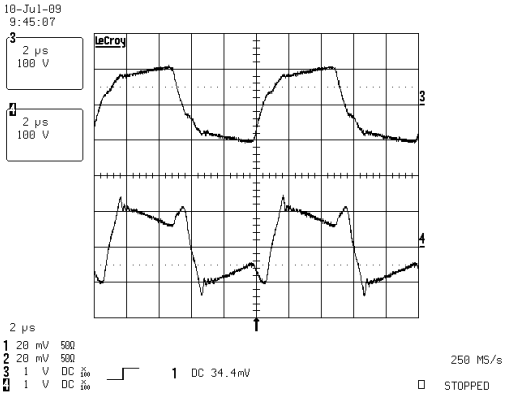

Figure 6.19: Observed waveforms of the voltage across the high-frequency capacitors C_1 (Ch.3) and C_2 (Ch.4) in power sharing mode

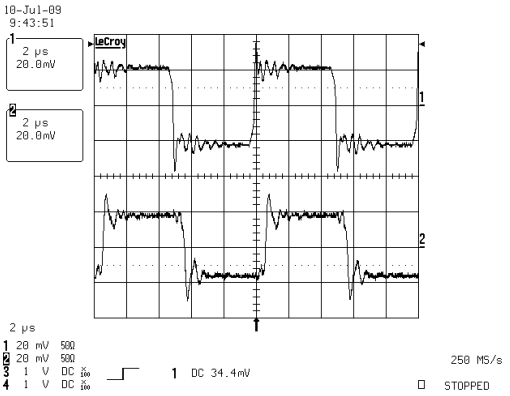

Figure 6.20: Observed waveforms of the high frequency square-wave currents i_{1hf} (Ch.1 - 4A/div) and i_{2hf} (Ch.2 - 4A/div) in power sharing mode

the corresponding phase-shift ϕ_{12} between them are shown in Fig. 6.20. The transformer winding3 voltage v_{ohf} along with the rectified voltage v_{or} whose average value is $107V$ are shown in Fig. 6.21. The experiment is done in open loop with an output power of $140W$.

The leakage inductance of each of the transformers is a non-ideality affecting the the square-wave currents as can be observed in the ringing in Fig. 6.20. This results in overvoltage appearing across the switches at the end of overlap time. Hence, the voltage rating and the switching losses increase in the switches. Also the diodes in the switches have reverse recovery effect causing further increase in losses. The voltage across the

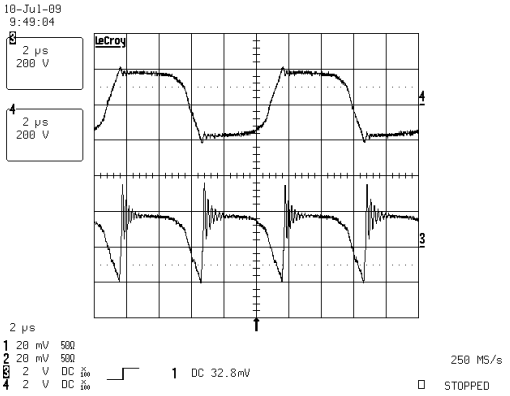

Figure 6.21: Observed waveforms of the voltage across the high-frequency capacitor C_3 (Ch.3) and the rectified waveform v_{or} (Ch.4) in power sharing mode

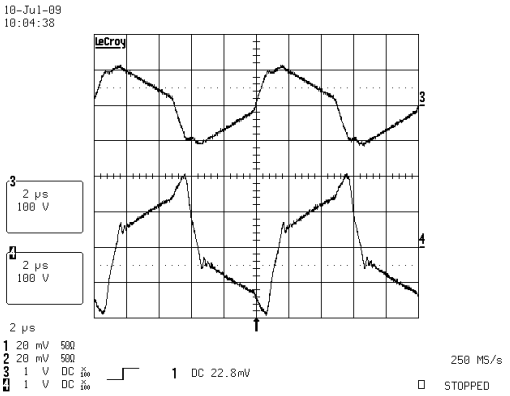

Figure 6.22: Observed waveforms of the voltage across the high-frequency capacitors C_1 (Ch.3) and C_2 (Ch.4) in power sharing mode for a ϕ_{12} increase of 5^o

high-frequency capacitors in Fig. 6.19 is very high due to the high step-up ratio of the transformers. Since the transformer secondaries are connected in delta, the algebraic sum of v_{C_1} and v_{C_2} appears across the winding3 voltage in Fig. 6.21.

The converter being current-fed has inherently high voltages across the switches as compared to high currents in the voltage-fed three-port converter. This disadvantage combined with the effect of leakage inductance restrict the use of this converter when compared to the series resonant converter presented in previous chapters. The phase-shift ϕ_{12} is increased by 5^o which results in decrease in port1 power according to Fig. 6.9a. The same is observed in the prototype and the results of the high-frequency

voltages across the capacitors C_1 and C_2 for this operating point are shown in Fig. 6.22 where the voltage v_{C_2} has a higher peak value. The output voltage drops by $5V$ in this case.

6.6 Conclusion

In this Chapter, the current-fed three-port dc-dc converter is proposed. Steady-state analysis of the converter is presented with phase-shifts between the active bridges as the control variables. It can be observed that the output voltage is independent of the load resistance. Also, as the load reduces the power from port2 remains almost constant and the current in port1 reverses direction. Small-signal model around a steady-state operating point is presented and simulation results of the controller are given. Simulation results of the converter in power sharing mode and battery charging mode are presented.

Chapter 7

Conclusion

Renewable energy sources such as fuel-cell, PV array are being increasingly used for stand-alone residential, commercial and automobile applications. Multi-port dc-dc converters are needed to interface the sources and the load along with energy storage in such applications. This thesis addresses this need by proposing two converter topologies. Both the topologies use high-frequency ac-link and hence have the advantages of reduced size, reduced power conversion stages and reduced part count when compared to conventional dc-link based systems. Some of the important conclusions in the work done in this thesis are discussed in the following section.

7.1 Conclusion

7.1.1 Series resonant three-port converter

In Chapter 2, a three-port series resonant converter [43] is proposed. It has two series resonant tanks and a three-winding transformer. Bi-directional power flow in all ports is achieved by phase-shift control of the three active bridges. Detailed analysis of the converter to determine the steady-state expressions of output voltage, port power, peak tank currents, peak tank voltages and soft-switching operation boundary is presented. The existing high-frequency ac-link topology for three-port converter uses only inductances, which includes the leakage inductances of the three-winding transformer, for power flow control. Since the power flow between ports is inversely proportional to the

impedance offered by the leakage inductance and the external inductance, impedance has to be low at high power levels. To get realizable inductance values equal to or more than the leakage inductance of the transformer, the switching frequency has to be reduced. Hence the selection of switching frequency is not independent of the value of inductance. The proposed series-resonant converter has more freedom in choosing realizable inductance values and the switching frequency, independent of each other. Such a converter can operate at higher switching frequencies for medium and high-power converters. A detailed comparison with the existing three-port converter in literature is presented in Chapter 4.

The tank capacitors in the series resonant converter play an additional role of blocking dc voltages caused because of difference in dead times and characteristics of the switches used in the active bridges. Whereas in existing three-port converter, the magnetizing inductance has to be reduced significantly to prevent saturation of the transformer. This also affects the power flow calculations since it changes the impedance in the power flow expressions. A detailed analysis of the three-winding transformer and its effect on the operation of the series resonant three-port converter is discussed in Section 2.5.1 and Section 4.2.3. The analysis concludes that the effect of the magnetizing inductance and the third winding leakage inductance on the power flow between ports can be reduced by designing the quality factors appropriately.

The steady-state analysis presented in Chapter 2 uses sinusoidal approximation. Such an approximation is valid due to filtering action of the series resonant tanks on the harmonics of the square wave applied voltages. With this approximation the derivation of the steady-state expressions are simplified. The expressions are converted to per unit and the design procedure is explained in Chapter 4. The design procedure gives details on selection of the voltage conversion ratios and its effect on soft-switching operating boundary. From the design procedure, it can be concluded that the three-port converter can do soft-switching in all switches provided that the voltage conversion ratios are chosen to be unity. Also the procedure ensures operation in all three modes, power sharing, battery charging and regenerative load.

Dynamic analysis of the converter using generalized averaging method is explained in Chapter 3. Two different time scales are identified which simplifies the controller design. Methods to control the output voltage in closed loop with a fixed reference for

one of the port currents are explained in this Chapter. The controller is implemented in FPGA in a laboratory prototype and the results are given in Chapter 4. These experimental results augment the analysis and simulation results.

The series-resonant three-port converter is modified for uni-directional load applications [44, 45] in Chapter 5. Due to the presence of diode bridge at the output, the phase-shift between the active bridges and the diode bridge is fixed and not controllable. Two phase-shift control variables are proposed for this converter. A center modulation technique is adopted to remove the interdependence on the phase-shifts between bridges and between legs in a single bridge. Using this control technique, bi-directional power flow in the other two ports are achieved. Detailed analysis are presented to determine the modified output voltage, port power, tank voltages, tank currents and soft-switching operating boundary. From the analysis it can be concluded that soft-switching operation in all the switches is not possible in this converter. Bi-directional power flow and control using phase-shifts are verified both in simulation and hardware prototype and the results are presented. Analytical expressions for peak tank currents and voltages including transformer rating are difficult to derive due to the presence of diode bridge and hence simulation results at various operating points are given in this Chapter.

7.1.2 Current-fed three-port converter

A current-fed three-port converter [46] is proposed in Chapter 6. This converter has inductors at the input and hence act as current ports. This ensures dc currents at the ports and thereby eliminates the need of capacitive filters as in the series resonant three-port converter. This converter is the dual of the existing three-port converter with only inductances. In this converter the square wave currents are phase-shifted from each other to control power flow between ports. Three separate transformers are needed and their secondaries are connected in delta. Detailed analysis of the converter is presented in this Chapter to determine the output voltage and power flow expressions. It is observed from the analysis that the output voltage is independent of the load resistance as opposed to the series resonant converter. Bi-directional power flow in the battery port is possible and verified through analysis and simulation.

The converter being current-fed uses uni-directional current switches and hence requires one Mosfet and one diode for each switch. This increases the semiconductor

switch count. Also for battery port, the diode needs to be replaced by another Mosfet to enable current direction reversal during battery charging. Since capacitors are used in the high-frequency side, the voltages across the capacitors increase two or three times the nominal voltage of the ports. This increases the voltage rating of the devices. These are some of the disadvantages of this converter over the series resonant three-port converter.

Sinusoidal approximation is not possible in this converter due to the high third and fifth harmonic content in the voltage waveforms. Hence when the generalized averaging theory is applied, the number of state equations increase three-fold. A small-signal analysis around a steady-state operating point is presented in Chapter 6. Simulation results of the converter in closed loop are presented for variations around the steady-state operating point.

7.2 Future work

The future scope of this work can include the following,

- Parallel resonant, LCC resonant and self-oscillating resonant circuits have unique advantages in two-port configurations. These topologies can be extended for three-port applications.

- This thesis discusses dc-dc-dc power conversion. Rectifiers or inverters are needed as additional power conversion stages to interface ac sources and ac loads. High frequency ac-link based single-stage power conversion can also be explored for ac-dc-ac three-port converter. Modified phase-shift modulation techniques need to be proposed for ac-dc-ac interfaces.

- The application scope of this three-port converter can be extended to power flow control devices in residential and commercial buildings, uninterruptible power supplies and high-power automobile applications.

- This thesis discusses three-port converter and the same principle can be extended to four-port or multi-port converters. The analysis and control methods for such configurations have to be explored.

Bibliography

[1] (2009) Solar america cities. U.S. Department of Energy. [Online]. Available: http://solaramericacities.energy.gov/

[2] "Final report on energy storage technologies," U.S. Department of Energy, Electricity Advisory Committee, Dec. 2008.

[3] (2009) Fuel cell vehicles. U.S. Department of Energy. [Online]. Available: http://www.fueleconomy.gov/feg/fuelcell.shtml

[4] C. Zhao and J. W. Kolar, "A novel three-phase three-port ups employing a single high-frquency isolation transformer," in *Proc. IEEE Power Electronics Specialists Conference (PESC'04)*, 2004, pp. 4135–4141.

[5] H. Tao, A. Kotsopulos, J. L. Duarte, and M. A. M. Hendrix, "Family of multiport bidirectional dc-dc converters," *IEE Proceedings in Electric Power Applications*, vol. 153, no. 15, pp. 451–458, May 2006.

[6] M. H. Kheraluwala, R. W. Gascoigne, D. M. Divan, and E. D. Baumann, "Performance characterization of a high-power dual active bridge dc-to-dc converter," *IEEE Trans. Ind. Appl.*, vol. 28, no. 6, pp. 1294–1300, Nov. 1992.

[7] R. L. Steigerwald, "Half bridge resonant converter topologies," *IEEE Trans. Power Electron.*, vol. 3, no. 2, pp. 173–182, Apr. 1988.

[8] P. Jain and H. Pinheiro, "Hybrid high frequency ac power distribution architecture for telecommunication systems," *Aerospace and Electronic Systems, IEEE Transactions on*, vol. 35, no. 1, pp. 138–147, Jan 1999.

[9] Z. Ye, P. Jain, and P. Sen, "A full-bridge resonant inverter with modified phase-shift modulation for high-frequency ac power distribution systems," *IEEE Trans. Ind. Electron.*, vol. 54, no. 5, pp. 2831–2845, Oct. 2007.

[10] J. L. Duarte, M. A. M. Hendrix, and M. G. Simoes, "Three-port bi-directional converter for hybrid fuel cell systems," *IEEE Trans. Power Electron.*, vol. 22, no. 2, pp. 480–487, Mar. 2007.

[11] D. Maksimovic, R. Erickson, and C. Griesbach, "Modeling of cross-regulation in converters containing coupled inductors," *IEEE Trans. Power Electron.*, vol. 15, no. 4, pp. 607–615, Jul 2000.

[12] H. Tao, J. Duarte, and M. Hendrix, "Three-port triple-half-bridge bidirectional converter with zero-voltage switching," *IEEE Trans. Power Electron.*, vol. 23, no. 2, pp. 782–792, March 2008.

[13] H. Tao, A. Kotsopoulos, J. Duarte, and M. Hendrix, "Transformer-coupled multi-port zvs bidirectional dcdc converter with wide input range," *IEEE Trans. Power Electron.*, vol. 23, no. 2, pp. 771–781, March 2008.

[14] H. Tao, J. L. Duarte, and M. A. M. Hendrix, "High-power three-port three-phase bidirectional dc-dc converter," in *Proc. IEEE Industry Applications Society 42nd Annual Meeting (IAS'07)*, 2007, pp. 2022–2029.

[15] D. Liu and H. Liu, "A zvs bi-directional dc-dc converter for multiple energy storage elements," *IEEE Trans. Power Electron.*, vol. 21, no. 5, pp. 1513–1517, Sep. 2006.

[16] B. Dobbs and P. Chapman, "A multiple-input dc-dc converter topology," *Power Electronics Letters, IEEE*, vol. 1, no. 1, pp. 6–9, March 2003.

[17] H. Matsuo, K. Kobayashi, Y. Sekine, M. Asano, and L. Wenzhong, "Novel solar cell power supply system using the multiple-input dc-dc converter," in *Telecommunications Energy Conference, 1998. INTELEC. Twentieth International*, 1998, pp. 797–802.

[18] H. Al-Atrash, F. Tian, and I. Batarseh, "Tri-modal half-bridge converter topology for three-port interface," *IEEE Trans. Power Electron.*, vol. 22, no. 1, pp. 341–345, Jan. 2007.

[19] H. Pinheiro and P. K. Jain, "Series-parallel resonant ups with capacitive output dc bus filter for powering hfc networks," *IEEE Trans. Power Electron.*, vol. 17, no. 6, pp. 971–979, Nov. 2002.

[20] H. Al-Atrash, F. Tian, and I. Batarseh, "Tri-modal half-bridge converter topology for three-port interface," *IEEE Trans. Power Electron.*, vol. 22, no. 1, pp. 341–345, Jan. 2007.

[21] S. Inoue and H. Akagi, "A bidirectional isolated dcdc converter as a core circuit of the next-generation medium-voltage power conversion system," *IEEE Trans. Power Electron.*, vol. 22, no. 2, pp. 535–542, March 2007.

[22] F. Z. Peng, M. Shen, and K. Holland, "Application of z-source inverter for traction drive of fuel cellbattery hybrid electric vehicles," *IEEE Trans. Power Electron.*, vol. 22, no. 3, pp. 1054–1061, May 2007.

[23] Y.-M. Chen, Y.-C. Liu, S.-C. Hung, and C.-S. Cheng, "Multi-input inverter for grid-connected hybrid pv/wind power system," *IEEE Trans. Power Electron.*, vol. 22, no. 3, pp. 1070–1077, May 2007.

[24] G.-J. Su and L. Tang, "A multiphase, modular, bidirectional, triple-voltage dcdc converter for hybrid and fuel cell vehicle power systems," *IEEE Trans. Power Electron.*, vol. 23, no. 6, pp. 3035–3046, Nov. 2008.

[25] X. Li and A. K. S. Bhat, "Ac equivalent circuit analysis for high-frequency isolated dual-bridge series resonant dc/dc converter," in *Proc. IEEE Power Electronics Specialists Conference (PESC'08)*, 2008, pp. 238–244.

[26] B. S. Nathan, "Analysis, simulation and design of series resonant converter for high voltage applications," M.Sc.(Engg.) thesis, Indian Institute of Science, Bangalore, India, Dec. 1999.

[27] S. Sanders, J. Noworolski, X. Liu, and G. Verghese, "Generalized averaging method for power conversion circuits," *IEEE Trans. Power Electron.*, vol. 6, no. 2, pp. 251–259, Apr 1991.

[28] J. Carrasco, E. Galvan, G. Valderrama, R. Ortega, and A. Stankovic, "Analysis and experimentation of nonlinear adaptive controllers for the series resonant converter," *IEEE Trans. Power Electron.*, vol. 15, no. 3, pp. 536–544, May 2000.

[29] A. Stankovic, "A dissipativity-based controller for series resonant dc/dc converters," in *Proc. IEEE Power Electronics Specialists Conference (PESC'96)*, 1996, pp. 1844–1849.

[30] D. Maksimovic, A. Stankovic, V. Thottuvelil, and G. Verghese, "Modeling and simulation of power electronic converters," *Proc. IEEE*, vol. 89, no. 6, pp. 898–912, Jun 2001.

[31] A. Stankovic, D. Perreault, and K. Sato, "Synthesis of dissipative nonlinear controllers for series resonant dc/dc converters," *IEEE Trans. Power Electron.*, vol. 14, no. 4, pp. 673–682, Jul 1999.

[32] C. Jacobson, A. Stankovic, and G. Tadmor, "Design of robust controllers for resonant dc/dc converters," Sep 1995, pp. 360–365.

[33] Y. Lu, K. Cheng, S. Ho, and J. Pan, "Passivity-based control of a phase-shifted resonant converter," *Electric Power Applications, IEE Proceedings* -, vol. 152, no. 6, pp. 1509–1515, Nov. 2005.

[34] H. K. Khalil, *Nonlinear Systems*, 3rd ed. Prentice Hall, 2002.

[35] (2009) Nuvera fuel cells, powerflow. [Online]. Available: http://www.nuvera.com/products/powerflow.php

[36] O. Bitsche and G. Gutmann, "Systems for hybrid cars," *Journal of Power Sources*, vol. 127, no. 1-2, pp. 8 – 15, 2004, eighth Ulmer Electrochemische Tage.

[37] N. Mohan, T. M. Undeland, and W. P. Robbins, *Power Electronics Converters, Applications and Design*, 3rd ed. John Wiley and Sons, Inc, 2003.

[38] R. Middlebrook and S. Cuk, *Advances in switched-mode power conversion, Vols 1 and 2*, 1st ed. Teslaco, 1983.

[39] (2009) Digilent basys board reference manual. [Online]. Available: http://www.digilentinc.com/Data/Products/BASYS/BASYS_C_rm.pdf

[40] H. Krishnaswami and V. Ramanarayanan, "Control of high-frequency ac link electronic transformer," *Electric Power Applications, IEE Proceedings* -, vol. 152, no. 3, pp. 509–516, May 2005.

[41] R. W. Erickson and D. Maksimovic, *Fundamentals of Power Electronics*, 2nd ed. Kluwer Academic Publishers, 2000.

[42] M. Ehsani, I. Husain, and M. Bilgic, "Inverse dual converter (idc) for high power dc-dc applications," in *Power Electronics Specialists Conference, 1990. PESC '90 Record., 21st Annual IEEE*, Jun 1990, pp. 814–821.

[43] H. Krishnaswami and N. Mohan, "Three-port series-resonant dc-dc converter to interface renewable energy sources with bi-directional load and energy storage ports," IEEE Trans. Power Electron., accepted for publication.

[44] H. Krishnaswami and N. Mohan, "Constant switching frequency series resonant three-port bi-directional dc-dc converter," in *Proc. IEEE Power Electronics Specialists Conference (PESC'08)*, 2008, pp. 1640–1645.

[45] H. Krishnaswami and N. Mohan, "Simulation model of a three-port bi-directional series resonant dc-dc converter to determine component specifications," in *Proc. SCS Grand Challenges in Modeling and Simulation (GCMS'08)*, 2008.

[46] H. Krishnaswami and N. Mohan, "A current-fed three-port bi-directional dc-dc converter," in *Proc. IEEE International Telecommunications Energy Conference (INTELEC'07)*, 2007, pp. 523–526.